Dissertation
zur Erlangung des akademischen Grades
”doctor rerum naturalium” *(Dr. rer. nat.)*
in der Wissenschaftsdisziplin
Biologische Physik

Locomotion of a bacterium
with a polar bundle of flagella

**Insights into movement and navigation
by fluorescence high speed microscopy**

Marius Hintsche, M. Sc.

Potsdam,
05.09.2018

eingereicht an der
Mathematisch-Naturwissenschaftlichen Fakultät
Institut für Physik und Astronomie

Ort und Tag der Disputation:
Potsdam, 28. Februar 2019

Selbständigkeitserklärung

Ich erkläre, dass ich die vorliegende Arbeit selbständig und nur unter Verwendung der angegebenen Literatur und Hilfsmittel angefertigt habe.

Potsdam, den 05. September 2018   Marius Hintsche

Contents

Contents

List of Figures

List of Tables

1. Introduction

Many, if not most microorganisms are able to move through their environment in a directed manner. They control their motion in order to attain a variety of goals. From finding and consuming food to escaping predation, active motion, called motility in the context of microbiology, plays a vital role for all domains of life (Jarrell and McBride, 2008). Among the many modes of movement, this work will focus on the swimming motility of bacteria.

Due to their often fast reproductive rates, bacteria are of importance in many scientific and technical fields. They form biofilms, infect other organisms, or might even consume harmful substances, for example in activated sewage sludge. Recently, it became apparent that the bacterial microbiomes associated with animals and humans are of special interest (McFall-Ngai et al., 2013). All of these processes are frequently associated with, or even dependent on, the ability to actively move to the right place at the right time (Schaechter, 2009).

Bacterial motility and its physical and biological mechanisms have therefore been studied in great detail since the inception of microbiology. A first detailed understanding of swimming motility was obtained in the 1970s by Howard Berg, Robert Macnab and others. They found that bacteria swim by rotating thin, helical filaments attached to their cell body (H. C. Berg and Anderson, 1973; Macnab, 1976). This is one of the few instances in biology where a true rotating motion occurs, and presents a fascinating interdisciplinary field between physics and biology.

In the beginning, the study of bacterial motility was tightly coupled with their chemotactic ability (Adler, 1969). Chemotaxis describes the directed motion of microorganisms in response to chemical cues such as food and is important for the formation of bacterial biofilms, as well as for their virulence and infectious diseases (Costerton et al., 1999).

Swimming and chemotaxis at the micrometer scale was unraveled using first *Escherichia coli* (*E. coli*) and *Salmonella typhimurium* (commonly only referred to as *Salmonella* in the literature (Neidhardt and Curtiss, 1996)) as the model organisms. These workhorses of microbiology have multiple flagella, scattered randomly over their cell body (peritrichous flagellation) (Neidhardt and Curtiss, 1996). The arrangement of the flagella over the cell body varies considerably with different species of bacteria (Leifson, 1960). However, so much work has been focused on *E. coli* and its peritrichous cousins, that we know surprisingly little about the motility of other bacteria that have different flagellation types. A recent discovery was the rudder-like action of the flagellum of some marina bacteria. Due to a mechanical instability in the attachment point of their single, polar flagellum, it may flick 90° to the side under certain conditions. This move greatly expands the motile possibilities for these bacteria (Xie et al.,

2011).

There are however, many more different flagellation patterns found in bacteria (Leifson, 1960), while most of their motility mechanisms have not been studied in detail. Previous studies on *Pseudomonas putida* (*P. putida*) had shown that this multiflagellated bacterium has two "gears", meaning that it can change its speed from one run to the next (Theves, Taktikos, et al., 2013). *P. putida* has multiple flagella attached to one of its cell poles. How the motion it performs is possible with this polar bundle of flagella is not known and cannot be explained by current models for flagellar interaction dynamics.

In light of the lack of specific knowledge about *P. putida's* motility, the goals of this thesis are as follows. We want to asses the influence of the flagellation pattern of the lophotrichous bacterium, *P. putida*, on its general motility pattern. It is therefore our aim to reveal the nature of its speed changes and shed light on the inter-flagella dynamics. The technical method we chose for this aim was the fluorescent labeling of flagella in swimming *P. putida* and their direct observation by high-speed microscopy. Because the motility pattern is sufficiently different from the peritrichous bacteria used as model organisms in this field, we wanted to explore if the chemotaxis strategy of *P. putida* is also different from the classical *E. coli* system. We also want to extend the study of bacterial motility from mostly bulk-fluid observations to the realm of structured environments. To this end we will evaluate the impact of an artificial, structured material on the swimming dynamics of *P. putida* through direct microscopic observation.

The outline of this work from here on is as follows. A literature review section gives the background for this study and the methods, concepts and major results that have been attained so far. We introduce the two model organisms used in this thesis and then describe their motility and chemotaxis systems from a microbiological standpoint. Then we introduce the physical and hydrodynamical basis for their swimming motility and conclude the review section with an overview of the concepts of stochastic modeling used to describe the random walk nature of bacterial swimmers.

Afterwards, we describe the methods and materials used, before reporting the results obtained in the course of this thesis. There, we describe the flagellar and bundle dynamics of *P. putida* on the sub-seconds time scale and then discuss the resulting swimming pattern. This enables us to answer the most pressing questions concerning this organism's swimming motility that had been described before (Theves, Taktikos, et al., 2013). Further more, we explore how the motility pattern of single cells changes when they are swimming in an artificial porous medium and discuss what implications and advantages this might have in *P. putida's* natural habitat.

After this exploration of our model bacterium's swimming, we turn to its navigation in chemical landscapes. Here, we characterize its behavior in gradients of a chemoattractant and compare its response to that of other bacteria. Finally, we present a novel classification algorithm for dividing swimming trajectories into runs and turns.

The thesis concludes with a summary and a discussion of questions raised by our study and possibilities for future investigation.

2. Background

Bacteria are ubiquitous in nature. They play a vital role in almost every ecosystem and living organism, and are indispensable for research in modern biology . Because species adapted to high nutrient environments have very high reproduction rates – up to one doubling per hour – they are often used as a model organism in many biological disciplines.

In the 1970s, researches began to ask and understand about their locomotion (H. C. Berg and Anderson, 1973; Taylor and Koshland, 1974). Many bacteria can propel themselves through liquid environments with the help of their helical flagella. Most early insights into the bacterial propulsion apparatus and its function were gained from *E. coli*. But today, more and more aspects of bacterial swimming that are not present in, or different from, *E. coli* are being discovered (Xie et al., 2011; Kühn et al., 2017).

Additional interest in their physical abilities has grown in recent years since the advent of microbiome research. It has renewed interest in the relation between microbiota and their hosts, where the former often outnumber the latter in cell numbers by orders of magnitude (McFall-Ngai et al., 2013).

This work is mainly concerned with the motion and navigation of *P. putida*, a gram negative rod-shaped soil bacterium.

2.1. Model organisms

Escherichia coli

One of the most well characterized bacteria and indeed life forms on earth is *Escherichia coli* (Schaechter, 2009). A member of the family *Enterobacteriacea*, it is a gram-negative, rod-shaped bacterium, which is able to grow rapidly with and without oxygen. Most *Enterobacteriacea*, are closely associated with humans and other vertebrates, were they often live in the gut. Many species are part of a healthy intestinal flora, but some live a pathogenic lifestyle and cause different diseases (Neidhardt and Curtiss, 1996).

E. coli is one of the work horses of micro- and molecular biology. Many aspects, including most of its genome, proteome and metabolome have been studied intensively and it has become a reference case in many fields of biology. Together with *Salmonella* it was also the bacterium with which the means of flagella mediated swimming motility were elucidated (H. C. Berg and Anderson, 1973; H. C. Berg, 2004). This is why it is still the most often studied example of bacterial motility and why we have chosen to use it in parts of this thesis.

Therefore the motile nature of *E. coli* is of great interest for this work. Most of its wild type strains are motile. They poses typically 5-10 thin helical flagellar filaments, which are themselves passive – in contrast to eukaryotic flagella. Bacterial flagellar filaments are driven by the motor to which they are attached (Neidhardt and Curtiss, 1996). In section 2.2 we describe in detail the mechanism with which *E. coli* swims using its rotating flagella.

An important aspect of bacterial motility is the ability to follow chemical cues, which may be attracting or repelling. *E. coli* can respond to a variety of chemicals, such as various saccharides and amino acids (Neidhardt and Curtiss, 1996). The signal transduction network that translates chemical signals from the outside into a control signal for the motility apparatus is described in section 2.3.

Pseudomonas putida
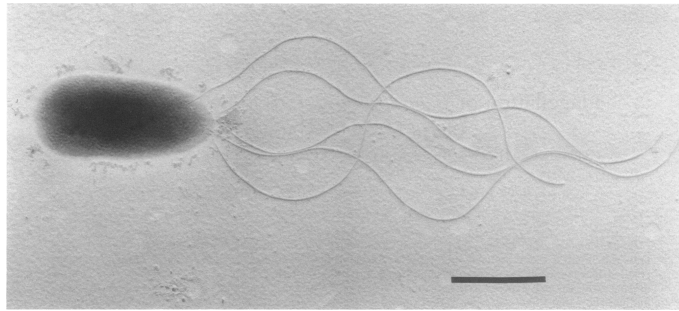
Figure 2.1.: Flagellation of *P. putida* PRS2000 (electron micrograph). Scale bar is 1 µm. Reproduced from Harwood, Fosnaugh, et al. (1989).

The main model organism used in this work, is *P. putida* KT2440. It belongs to the genus *Pseudomonas* which is ubiquitous in nature, and is often found in close association with plants and animals. Most members of this genus have a very versatile metabolism and can degrade different organic pollutants such as aromatic compounds (Schaechter, 2009). They are gram-negative, rod-shaped bacteria that are motile by means of one or more polar flagella (Lighthill, 1975).

Pseudomonas putida lives in the soil, where it is mainly found in the rhizosphere in association with plant roots. Because its cultivation is uncomplicated and it is a non infectious representative of its genus, *P. putida* has been used extensively as a model organism in basic research (Timmis, 2002). It has further been used as a biocontrol agent to protect tobacco plants against infections from the black root disease caused by *Fusarium* species (Schaechter, 2009). One of the first organisms to be patented as an agent for biological waste removal was also *P. putida* (Chakrabarty, 1981). It was supposed to be used in this way, because *P. putida* has a very diverse metabolism and can tolerate and even degrade many organic solvents and aromatic compounds, like toluene and benzoic acid (Belda et al., 2016). Because of these metabolic qualities and subsequent research interest, its genome has been fully sequenced and its metabolic

pathways have been thoroughly analyzed (Nelson et al., 2002; Belda et al., 2016).

In addition, it has been shown to be attracted to and actively swim towards sources of different aromatic acids, which makes it interesting for the investigation of chemotaxis in this thesis. Notably, *P. putida* can grow on sodium benzoate as is sole carbon source, which is commonly used as a food preservative. In *P. putida* however, it induces the bacteria to be attracted to that compound (Harwood, Rivelli, et al., 1984).

The shape and flagellation pattern of our model organism are shown in figure 2.1. The cell body is $1\,\mu m$ to $3\,\mu m$ long and about $1\,\mu m$ in diameter. Attached to one pole of the cell are 5 to 8 flagella (Harwood, Rivelli, et al., 1984). How these flagella confer swimming motility to the organism is discussed in the following section.

2.2. Bacterial motility

Many microbiological processes rely on motility – the ability of microorganisms to actively move through their environments. Examples are chemotaxis, biofilm formation and pathogenesis (Josenhans and Suerbaum, 2002) .

Bacterial motility is very diverse, as bacteria are present in many different environments and often need to move through them. It encompasses modes of movement such as twitching, gliding, swarming as well as swimming by different means. While the first two strategies can propel single cells along solid-liquid interfaces, swarming is used by actively growing cell colonies to move along moist surfaces (Turner, Zhang, et al., 2010). Swimming in contrast, is a process of moving through the bulk of a fluid even when no phase boundaries are present (Jarrell and McBride, 2008).

Most species of bacteria swim using long helical filaments called flagella. Others are able to swim without flagella, like *Spiroplasma* and *Synechococcus* species, through as of yet unknown mechanisms (Shaevitz et al., 2005; Ehlers and Oster, 2012). The most well studied mode of bacterial swimming is, however, the flagellar motility present in many bacteria. This fundamental process was investigated with different physical and biochemical methods. It will be the main object of this thesis and is further described below.

2.2.1. Flagellar propulsion

Structure

The swimming movement of most bacteria is driven by the rotation of one or multiple flagella. Each of these bacterial flagella is a thin and long helical filament, attached to the cell body at one end and suspended in the extracellular fluid. In contrast to its eukaryotic namesake, the filament itself is passive but is actively involved in the swimming motion . It is driven by the flagellar motor in order to produce motion (H. C. Berg, 2004). This motor rotates the attached flagellum and thus produces a thrust force on the cell body.

The flagellum of bacteria is a protein filament composed of the flagellin subunit protein FliC, which builds up a helically wound hollow structure, shown in figure 2.2.

It is about 20 µm in diameter (Terashima et al., 2008) and thus cannot be observed using conventional bright field microscopy (Macnab, 1976). Flagellin subunits are assembled into 11 protofilaments which are approximately parallel to the long axis of the filament (Terashima et al., 2008). Each protofilament can exist in either R- or L-type conformations. Their slightly different subunit spacings cause a twist of the filament which leads to its helical shape (K. Hasegawa et al., 1998; Samatey et al., 2001). Because different numbers of protofilaments can be in either state, the filament can exist in several different conformations (polymorphic states). Under certain conditions filaments can change back and forth between these states in a process called polymorphic switching (see section 2.2.1).
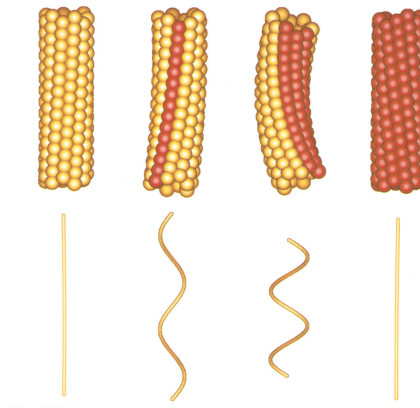
Figure 2.2.: Flagellar structure and subunit states.
Top: The bacterial flagellum is composed of 11 protofilaments made up of flagellin subunits. Each subunit can be in either L-type (◯) or R-type (●) conformation.
Bottom: Some of the 11 possible polymorphic forms of flagella. From left to right: L-type straight, normal, curly, R-type straight. Adapted from Terashima et al. (2008).

The flagellum is attached to the cell via a flexible hook (DePamphilis and Adler, 1971).

In *E. coli* and *Salmonella* the hook's length is tightly controlled to about 55 nm (Terashima et al., 2008). Because it needs to transmit the motor rotation to the flagellum proper, the hook is flexible along its long axis, while the flagellum itself is more stiff in order to produce sufficient resistance for propulsion (H. C. Berg, 2003).

The filament and the connecting hook are attached to the basal body, which is anchored in the cell wall (Hirano et al., 1994), see figure 2.3. This assembly consists of a rod and three coaxial rings (MS-, P-, and L-ring) (Terashima et al., 2008). Also associated is the Mot complex, which spans the cytoplasmic membrane and acts as the stator of the motor. A proton flux through this complex generates the torque which rotates the motor. Furthermore, the switch complex is responsible for switching the sense of rotation (H. C. Berg, 2003). The export apparatus at the very base of

the assembly is essential for elongation of the flagellar filament during cell growth. It exports unfolded flagellin proteins through the hollow filament, which then fold and self assemble at the tip of the flagellum (Terashima et al., 2008).
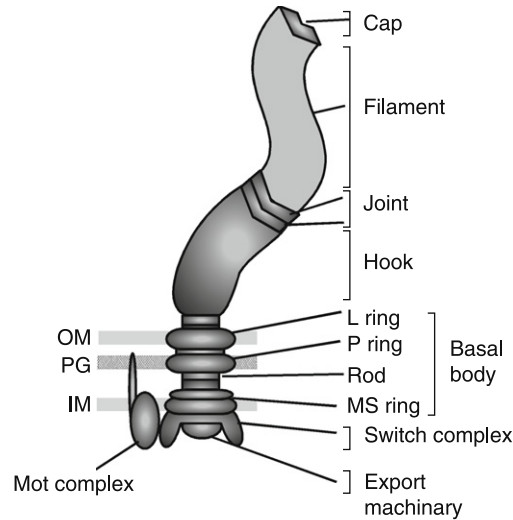
Figure 2.3.: Motor complex with hook and flagellar filament. The basal body (lower part) is attached to the outer membrane (OM) via the L ring, to the peptidoglycan via the P ring, and to the inner membrane (IM) via the MS ring. The Mot complex confers torque to the rotating parts, while the switch complex modulates rotation direction. Flagellar growth is mediated by the export machinery. Reproduced from Terashima et al. (2008).

Energy for the motor is supplied by a proton gradient across the inner membrane, which is build up by the cells metabolic activity (H. C. Berg, 2004). This provides a proton motive force which causes protons to flow through the motor complex, generating power for its rotation. Some bacteria however, use a Na^+ gradient as the power source for their motors (Sato and Homma, 2000). In *E. coli's* case, about 1200 protons are necessary to perform one revolution (Meister et al., 1987). It has been shown that under physiological conditions the motor operates in a constant torque regime (Chen and H. C. Berg, 2000), where it generates approximately 4500 pN nm (Berry and H. C. Berg, 1997).

The location of the motors and attached flagella over the cell body varies considerably between species. Bacteria can have single flagella (monotrichous) either on the cell pole (polar) or on the side of their elongated bodies (lateral). Species with multiple flagella range in from random distribution over the body surface (peritrichous) to tufts of flagella at one pole (lophotrichous) and even one or multiple flagella on both poles (amphitrichous) (Leifson, 1960).

Traditionally, prokaryotic flagella could be made visible only in dead and fixed cells through histological staining techniques, such as the crystal violet stain (E. Ryu,

1937) or electron microscopy. The observation of the moving flagella of live cells was initially achieved by Robert Macnab who observed the flagellar bundle of *Salmonella* under intense darkfield illumination (Macnab, 1976). This technique, however, had one severe drawback. Because the comparatively large cell body scatters much more light than the thin flagellar filaments, it outshines the flagella in its proximity.

A newer procedure to visualize the flagella of *E. coli* used amine specific labeling of the FliC subunits with a fluorescent dye (Turner, W. S. Ryu, et al., 2000). Further improvement of labeling quality was achieved by using a thiol specific staining technique. Substituting a solvent accessible amino acid in FliC for cysteine enabled a greater contrast by significantly reducing unwanted staining of the cell body (Turner, Zhang, et al., 2010). This procedure eliminates most of the drawbacks of previous methods of flagellar visualization. It was therefore adapted in this work and enabled the high speed live cell imaging required to elucidate the detailed dynamics of *P. putida's* swimming.

Polymorphic switching

Flagella are made up of protofilaments that can exist in either L- or R-type conformation. From their combinations 12 possible states of the whole filament arise, called polymorphic states (Terashima et al., 2008) – each one of them with a distinct twist and curvature (Kamiya and Asakura, 1976). These polymorphic states of the flagellum therefore differ in their helical pitch and radius (Macnab and Ornston, 1977). The balance between states is sensitive to perturbations, so that already a single point mutation can shift it toward complete L- or R- type conformation (F. Wang et al., 2017).

Polymorphic switching may be triggered in vitro by changing pH, temperature, or ionic strength (Kamiya and Asakura, 1976; E. Hasegawa et al., 1982). The conformation that is assumed during forward swimming is usually called the 'normal' form. In *Salmonella* it has a helix diameter of 0.4 µm and a pitch of 2.3 µm (Macnab and Ornston, 1977) and is similar across species (Shah et al., 2000). Other conformations that have been observed in vivo are, for example, curly I, curly II, coiled and semi-coiled.

In vivo, the switch is usually triggered through a change in torque or extensional force (Macnab and Ornston, 1977; Armitage, Pitta, et al., 1999; Darnton and H. C. Berg, 2007). A well known example is *E. coli*, where a switch from CCW to CW rotation triggers a polymorphic transitions from normal to curly (Darnton, Turner, et al., 2007; Vogel and Stark, 2013) and *R. sphaeroides*, where a switch from CCW rotation to a complete stop triggers a transition from normal to coiled form (Armitage, Pitta, et al., 1999; Vogel and Stark, 2013)).

Hydrodynamics at the microscopic scale

Life at the micrometer scale must employ very different mechanisms for swimming than larger animals. This is because viscosity becomes the dominant force, as an organisms characteristic scale decreases. The well known Reynolds number (Re) characterizes

this behavior and is defined as the ratio of inertil to viscous forces It is given by

$$\mathrm{Re} = \frac{\rho U L}{\eta} \; ,$$

where ρ is the fluid density, U and L the characteristic velocity and length scales, and η the dynamic viscosity of the fluid. For swimming bacteria Re is on the order of 10^{-5} (Lauga and Powers, 2009). In this regime the motion of a body through an aqueous fluid is governed by the Stokes equations

$$- \nabla p + \eta \Delta \mathbf{v} = 0 \quad \text{and} \quad \nabla \cdot \mathbf{v} = 0 \; , \tag{2.1}$$

of which the first one describes the relationship between the velocity field $\mathbf{v}$ and the pressure field p, while the second one is the continuity equation for mass conservation of an incompressible fluid.

Because the equations are time independent, they are time reversible. This means that reciprocal motion cannot not yield directed movement of a swimming body. One way to overcome this difficulty is through the corkscrew like motion of the helical flagellum that bacteria exhibit (E. M. Purcell, 1977). In their world dominated by viscous forces, a bacterium swimming with $30\,\mu\text{m/s}$ – corresponding to more than 10 body length per second – will come to a full stop within $1\,\text{Å}$ after stopping its motors (H. C. Berg, 2004).

Since the Stokes equations are linear, the relation between force ($\mathbf{F}$) and velocity ($\mathbf{v}$) as well as torque ($\mathbf{M}$) and rotation rate (ω) of a swimming body must also be linear. E. M. Purcell describes this relationship using the propulsion matrix formalism:

$$\begin{pmatrix} \mathbf{F} \\ \mathbf{M} \end{pmatrix} = \begin{pmatrix} \mathbf{A} & \mathbf{B} \\ \mathbf{B}^{\mathrm{T}} & \mathbf{C} \end{pmatrix} \cdot \begin{pmatrix} \mathbf{v} \\ \omega \end{pmatrix} \; . \tag{2.2}$$

Here $\mathbf{A}$ is the matrix of translational and $\mathbf{C}$ the matrix of rotational drag coefficients. The coupling of torques and forces, for example through a rotating chiral body such as a flagellum, is described $\mathbf{B}$ (Lighthill, 1975). This coupling is depicted in figure 2.4a. In the helical flagellum, this coupling can be understood in terms of the asymmetric drag coefficients for a small, rod shaped piece of helix. Figure 2.4b shows the two different drag forces associated with a thin rod that moves in a direction orthogonal or parallel to its long axis through the fluid. This asymmetry creates the thrust force of a rotating helix in this regime. The elements of $\mathbf{B}$ scale as: (Lauga and Powers, 2009)

$$\mathbf{B} \propto (\text{transverse drag} - \text{longitudinal drag}) \; .$$

Because of linearity of the stokes equations, the forces and torques produced by the cell body and flagella can be added. The elements of the propulsion matrix for swimming bacteria have been measured using optical tweezers as well as laser dark-field techniques (Chattopadhyay et al., 2006; Magariyama et al., 1995).
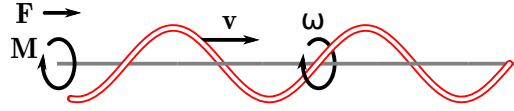
(a) Coaxial force **F** and torque **M** produced by a rotating left handed helix.
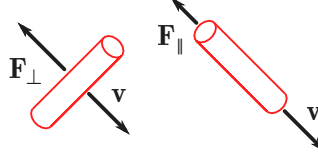
(b) Asymmetry of drag coefficients. The difference between the two drag forces $\mathbf{F}_\perp$ and $\mathbf{F}_\parallel$ creates the thrust force of a rotating helix element.

Figure 2.4.: Coupling between torques and forces. Adapted from E. M. Purcell (1977).

Torque balance

When a cell is swimming in the bulk of the fluid, far away from any boundaries, it has no net rotation and its motion will be torque free. Therefore, the torques exerted by the body and flagella on the fluid will balance each other (Lauga and Powers, 2009)

$$\mathbf{M}_b + \mathbf{M}_f = 0 \, .$$

These coaxial torques are caused by the frictional drag which the cell body M_b and the flagellar bundle M_f experience while moving through the surrounding fluid. According to the propulsion matrix equation 2.2, drag forces and torques are proportional to the speed and rotational speed $\omega_{\{f,b\}}$, respectively. Therefore the rotational speeds of the body and flagella are – for a given configuration of the two – fixed by the ratio of their drag coefficients $\gamma_{\{f,b\}}$

$$\frac{\omega_f}{\omega_b} = \frac{\gamma_b}{\gamma_f} \, . \tag{2.3}$$

Furthermore, the motor is the sole source of relative rotation of the two components, which means that its rotation is divided between the body and the flagella.

$$\omega_m = \omega_f + \omega_b \, . \tag{2.4}$$

Boundary effects

In proximity to a non-slip boundary surface, the axisymmetry of the propulsion mechanism is broken, which leads to a coupling of the rotation of the helical flagella around the helix axis and parallel to the surface. Because the side of the helix which is closer to the wall, experiences higher drag due to the no-slip condition, it experiences a force parallel to the wall. An equal but opposite force acts on the cell body, which rotates in the other direction. These two opposing forces on the body and on the flagellar bundle result in a torque perpendicular to the wall (Lauga, DiLuzio, et al., 2006). *E. coli,*

for example, has been observed to swim in counterclockwise circles when viewed from above a glass cover slip. In this case, the flagellar helices are left handed and rotate counterclockwise as viewed from behind the cell, while the body rotates clock wise (H. C. Berg and Turner, 1990).

Another well known wall-effect is a moment around the pitch axis of a cell swimming close to the boundary. This is due to the – in good approximation – dipolar flow field generated by the swimming bacterium. At a boundary surface, the no-slip condition can be satisfied by a hydrodynamical mirror image on the other side of the boundary. In this picture, the interaction with the mirror image produces a torque on the cell parallel to the surface. Therefore, pushers are reoriented parallel to the surface, while pullers are reoriented perpendicular to it (Berke et al., 2008; Lauga and Powers, 2009).

2.2.2. Motility patterns

Although the canonical example of flagellar propulsion is *E. coli*, many bacteria have slightly different swimming patterns. Many properties of their swimming patterns have been characterized and explained from physical, chemical and biological standpoints. All of the patterns are divided in two phases: straight movement and reorientation. These two phases are called runs and tumbles for peritrichous bacteria (H. C. Berg, 2004). Other species exhibit other kinds of reorientation events, such as reversals, flicks. In this work, we will refer to all of these reorientation processes as turns, unless specifically noted. The resulting coarse grained motion is depicted in figure 2.5. In
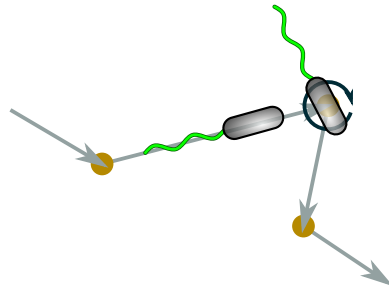
Figure 2.5.: General motility pattern of bacteria. Runs are represented by ➤ and turns are marked by ●.

the following section we will describe how this motion is achieved in bacteria, and how different species vary upon this theme.

E. coli and *Salmonella* have between one and 10 flagella, which are attached randomly over the whole cell body (peritrichous flagellation). During a run, all of the motors rotate counterclockwise (CCW), as seen from outside the cell envelope. The flagella are all in their normal left handed conformation and assemble into a coherent bundle behind the swimming cell. In this conformation they push the cell through the fluid. When one or more motors reverse their direction of rotation to clockwise (CW), the corresponding flagellum breaks apart from the bundle and undergoes a series of

polymorphic transitions (H. C. Berg and Anderson, 1973). This process initiates a tumble. Due to the now opposite sign of the applied torque, the flagellum changes from normal form to different right handed forms. Its off axis thrust deflects the cell body from its previous run direction to a new one. After the motor resumes its CCW rotation, the flagellum undergoes a transformation back to normal form as it rejoins the bundle. This concludes the tumble and starts a new run (Darnton, Turner, et al., 2007). The tumbling action changes the swimming direction between runs. The angles between runs are called tumble angles – or turning angles in other species. They are randomly distributed with a peak probability at 60° (H. C. Berg and Brown, 1972). A sketch of this pattern is shown in figures 2.5 and 2.6.
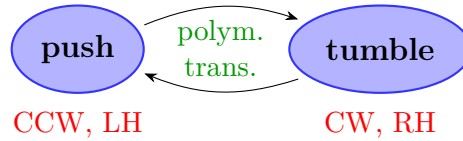
Figure 2.6.: Run-and-tumble pattern of peritrichous bacteria. States of motion are shown in blue, transitions between states are indicated with arrows ($\longrightarrow$). Rotation sense and flagella handedness are shown in red. Dynamical events triggered by the transitions are shown in green.

In contrast, many marine bacteria only have one flagellum attached to a cell pole. Here, the cell body is pushed by the single normal form flagellum, when the left handed filament rotates CCW. Reversal of the motor leads to a swimming mode where the cell body is pulled by the flagellum into a sharp reversal during which the direction of propagation changes by about 180°. The cell then stays in this pulling run, until the motor reverses again. Here, the flagellum does not change its polymorphic state during a reorientation event (Homma et al., 1996). In the species *Vibrio alginolyticus*, the transition from pull to push further is associated with a buckling of the hook. As its load switches from an extensional to a compressional force, the hook buckles which leads to a 90° flick of the flagellum. Consequently the turning angle of the flick transition is about 90° (Xie et al., 2011).
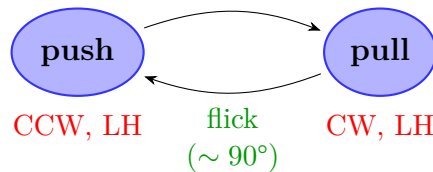
Figure 2.7.: Run-reverse-flick pattern of the monotrichous polar bacterium *V. alginolyticus*.

Yet another motility strategy is that of the monotrichous bacterium *Rhodobacter sphaeroides*. This species has one flagellum attached laterally to the cell body. During a run its motor rotates CW, while the flagellum is in normal right handed conformation and pushes the cell. At the end of a run the motor stops its rotation. It is

thought that the reorientation of the cell body is done mostly by rotational Brownian diffusion. However, recent work indicates that during stops *R. sphaeroides* actively enhances the reorientation process (Rosser, R. E. Baker, et al., 2014).

While the cell is pausing its motion is passively reoriented by rotational diffusion. When it is stopped, the flagellum assumes a right handed open coiled conformation with a larger radius and a much tighter pitch (Armitage and Schmitt, 1997).
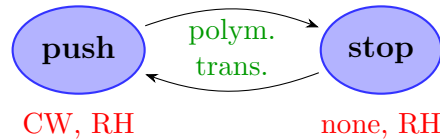
Figure 2.8.: Run-and-stop pattern of the monotrichous bacterium *R. sphaeroides*

Some *Pseudomonas* species perform a run-and-reverse pattern but also sometimes stop their motors during runs (Qian et al., 2013; Theves, Taktikos, et al., 2013). The purpose of these stops is not known yet. Other members of the genus such as *P. citronellis*, *P. fluorescence*, and *P. putida* have been known to alternate slow and fast runs under certain conditions (Taylor and Koshland, 1974; Ping et al., 2013; Theves, Taktikos, et al., 2013). The reasons for this behavior, however, were not reported in theses studies.

A different mode of bacterial motility has recently been discovered in *Shewanella putrefaciens*. When trapped in tight spaces, this polar monotrichous organism can transition to a swimming mode where the flagellum is not extended away from the cell body, but wrapped around it. This conformation may be triggered when the cell is stuck between an agar wedge and a cover slip. Starting in pulling mode the flagellum of stuck cell often exhibits a polymorphic transformation to the wrapped mode, in which the flagellum is wound around the cell body by the CW motor rotation. In that state the cell swims with a left-handed flagellum and its flagellated pole is in front (Kühn et al., 2017, Fig. 1.).
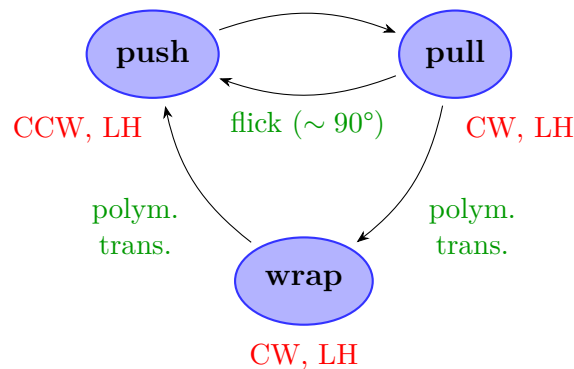
Figure 2.9.: Motility pattern of *S. putrefaciens*

The model organism studied in this work, *Pseudomonas putida* deviates somewhat

from classical models of bacterial motility. It is lophotrichously flagellated, which means it has multiple flagella attached to one pole (usually 3-8). Characteristic for this species are sharp 180° reversals (Harwood, Fosnaugh, et al., 1989). Unlike most other bacteria, it can abruptly change its speed while continuing in the same direction. This has been called a 0°-event, because an aspect of its swimming changes, but no net change of propagation direction follows. Similarly it may change its speed in conjunction with a reversal, but this is not always the case: sometimes the speed before and after reversals stays constant (Theves, Taktikos, et al., 2013; Theves, 2013). What causes these speed changes is not known. Even how the sharp reversals are possible is not entirely clear (Raatz et al., 2015). Usually, flagellar bundles are thought to be only stable when rotating in one direction compatible with their handedness – counterclockwise for left-handed and clockwise for right-handed filaments. Rotation in the other direction is thought to cause the bundle to disassemble due to destabilizing mechanical and hydrodynamical interactions between individual flagella (Macnab, 1977; Kim et al., 2003). Furthermore, cell tracking experiments as well as tethering assays show that it frequently stops its motors within runs (Theves, Taktikos, et al., 2013; Qian et al., 2013). The benefit of this behavior has also not been determined yet.

One of the central aims of this work is to answer the open questions concerning *P. putida's* swimming mechanism. What causes the two swimming speeds and the 180° reversals? How do they relate to each other or is just one mechanism responsible for both? These and other problems are addressed in the results section on Flagellar dynamics.

2.2.3. Structured environments

Bacteria are ubiquitous in the soil, where they often live in close association with plant roots (Ranjard and Richaume, 2001). Soils are composed of solid material particles and interleaved with a network of pores. The pores are usually filled with liquid as well as with gas phase material. It is in theses pores that motile bacteria can move (Vos et al., 2013). Soil particles can aggregate to a variety of sizes and the pores between them can range from micron size to hundreds of microns. Other components of the soil matrix are plant roots, fungal hyphae, and various organic compounds including extracellular polymeric substances (EPS) (Vos et al., 2013). This composition is depicted in figure 2.10.

Although it has been recognized that bacterial motility and chemotaxis in these kinds of environments can differ substantially from that in bulk media (Valdés-Parada et al., 2009), it has been difficult to directly visualize the movement of microorganisms in porous media. In the past, studies have primarily focused on macro-scale experiments, e.g. the artificial soil columns of M. Wang and Ford (2009), or numerical simulation of relevant motility parameters (Duffy and Ford, 1997). They showed that porous media have a significant impact on the random motility of bacteria, and that bioremediation strategies needs to take these influences under account (Duffy, Cummings, et al., 1995). Furthermore, Duffy and Ford (1997) found evidence, that *P. putida's* motility strategy is beneficial in porous environments since it reduces the
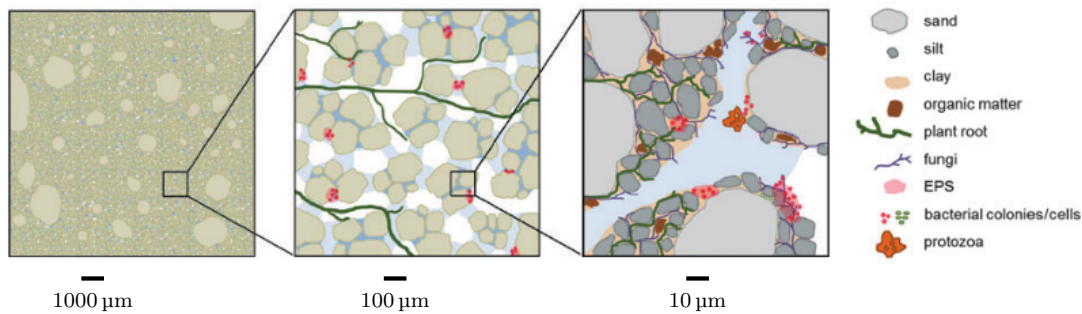
Figure 2.10.: Soil structure and microbiological composition. Depicted is a soil matrix on different lengths scales, with scale bars below each panel. Adapted from Vos et al. (2013, Fig. 2).

number of obstacle collisions. Recently, is has become possible to directly image bacteria in artificial, porous media (Leis et al., 2005; Raatz et al., 2015). This will give more insight into the swimming of microorganisms in structured environments.

2.3. Chemotaxis

Chemotaxis is the process of directed migration of microorganisms towards a source or sink of chemical compounds and almost all motile organisms exhibit a form of chemotaxis. Bacteria are able to sense a wide array of environmental signals from pH, temperature, osmolarity, and oxygen, to nutrients and toxins. They use these signal to move towards conditions favorable for reproduction or growth (Wadhams and Armitage, 2004). Conserved across almost all motile species of bacteria is a set of six regulatory proteins which enables chemotaxis in this domain of life (Stock and M. D. Baker, 2009). They serve in effect to modulate the turning frequency of a bacterium depending on whether it is swimming up or down a gradient. This results in a net movement up or down the gradient for attractants or repellents, respectively. The molecular components involved in this process, their interplay and organization will be examined in the following section (Sourjik and Wingreen, 2012).

2.3.1. *E. coli*

One of the most well known strategies for chemotaxis, and indeed intracellular signal transduction, is that of *E. coli* (H. C. Berg, 2004). Its chemotaxis machinery has been studied from biological (Falke et al., 1997; Parkinson, 2003), physical (H. Berg and E. Purcell, 1977; Mears et al., 2014), and information theoretical (Celani and Vergassola, 2010; Masson et al., 2012) points of view.

The bacterial chemotaxis pathway is an example of a two component signaling system (H. C. Berg, 2004). Its layout is shown in figure 2.11. In this type of protein signaling cascade, a signal molecule binds to a sensor, which regulates a transmitter,
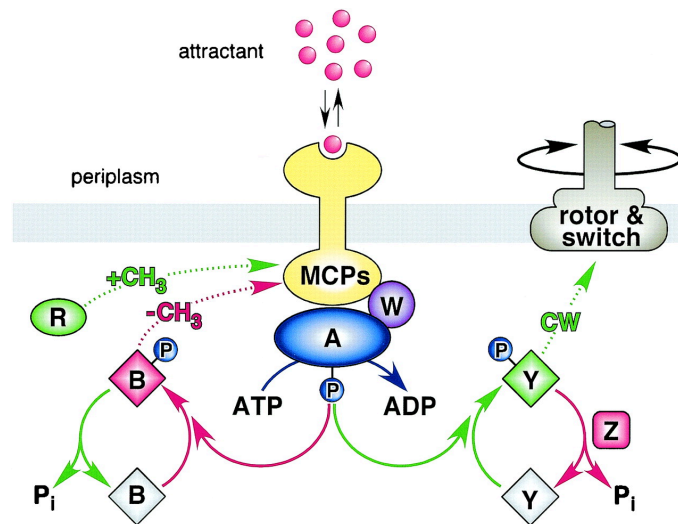
Figure 2.11.: Chemotaxis signaling pathway in *E. coli*.
Receptor MCPs bind the attractant and activate CheA (⬤) which phos-
phorylates the second messenger CheY (◇). CheY diffuses to the motor
complex, binds to FliM and modulated the switching probability. CheZ
(▢) constitutively de-phosphorylates the messenger CheY. Adaptation
is mediated through methylation and de-methylation of the receptor by
CheR (⬤) and CheB (◇). Reproduced from Parkinson (2003, fig. 1).

which in the end activates a receiver (Falke et al., 1997, fig. 1). The sensor protein in bacteria is usually a transmembrane receptor, called MCP (methyl-accepting chemotaxis protein). In *E. coli* they frequently form tight clusters (Krell et al., 2010). Attached to it is the transmitter complex CheW and CheA. The histidine kinase CheA autophosphorylates and in turn phosphorylates the competing response regulators CheY and CheB (Parkinson, 2003). Binding of attractant to the receptor complex reduces its autophosphorylation rate and thus reduces CheY phosphorylation.

At the output of the cascade, phosphorylated CheY (CheY-P) diffuses through the cytoplasm, binds to FliM in the switching complex and increases its probability of switching to CW rotation. This increases the probability of tumbles in *E. coli* and thus controls its overall tumbling frequency. Exactly how CheY-P influences the motor rotation remains to be elucidated (Falke et al., 1997; H. C. Berg, 2004). In *E. coli* CheY-P is also constantly dephosphorylated by CheZ.

Alternatively, CheB is phosphorylated by CheA and then actively demethylates the MCP at one of four different sites. The activation of the MCP and the associated CheA is reduced by this methylation, and thus attenuates the signal transduction. At the same time the MCP is constantly methylated by CheR. The different time scales of activation and methylation lead to an adaptation of the chemotaxis response and an increased sensitivity even at higher levels of attractants (Alon et al., 1999; Wadhams and Armitage, 2004).

The integrated dynamics of these processes shapes the overall response of the cell to temporally changing chemical cues. The positive action of phosphorylation and subsequent diffusion of CheY to the motor are much faster than the negative feedback of the demethylation CheB. A rise in chemoattractant concentration therefore results in a decrease of the tumbling frequency, since CheY phosphorylation by CheA is repressed by the activated MCP. Subsequently, the MCP is demethylated by the slower acting CheB, which desensitizes the receptor complex. This leads to a slowly increasing tumbling frequency – even while the attractant concentration stays high. The cell, therefore, adapts to the external signal (Celani and Vergassola, 2010; Masson et al., 2012; Wong-Ng et al., 2016).

2.3.2. Other bacteria

E. coli has four different MCPs which bind different classes of ligands. Most bacteria, however, posses more than 10 different MCPs on average (Lacal et al., 2010). More importantly, most species usually have more than one of the major components for intracellular signaling pathways, and often multiple homologue copies of the whole pathway (Hamer et al., 2010). It has also been shown that CheZ homologues are not present in many bacteria. Additional chemotaxis proteins, such as CheC and D (adaptation) and CheV (CheW homologue) are present in other bacteria. They are thought to mediate additional regulatory pathways not present in *E. coli* (Krell et al., 2010).

On the output side of the chemosensory system many bacteria are differently organized than *E. coli*. *Rhodobacter sphaeroides* for example, does not reverse its motor

as a reaction to CheY-P binding, but stops it completely (Pilizota et al., 2009). When it is not stopped, its motor rotates CCW at a constant speed (Armitage and Macnab, 1987). Yet another regulation of the motor occurs in *Sinorhizobium meliloti*. Here, the motor rotates only CW but decreases its rotation speed when concentrations of the attractant go down (Attmannspacher et al., 2005). Similar observations have been made in *Rhizobium lupini* (Scharf, 2002).

The main object in this work, *P. putida*, also possesses a slightly different set of chemotaxis genes than *E. coli* (Inmaculada Sampedro and Hill, 2015). Presumably because of its metabolic versatility, it has 23 MCPs (Nelson et al., 2002). It can respond to amino acids and sugars like *E. coli* and, in addition, also to many aromatic acids (Harwood, Parales, et al., 1990). It also has genes for aerotaxis, and the full set of CheA, B, R, and W, as well as CheY, and Z (Ditty et al., 1998; Nelson et al., 2002). Some chemotaxis genes, such as two putative CheV variants, are altogether not present in *E. coli* (García-Fontana et al., 2013; Belda et al., 2016). In *P. putida*, some major chemotaxis proteins possess homologue alternatives. Genes for CheY2 and B2 are present, but are uncharacterized as of yet (Nelson et al., 2002). CheR2 has been found to specifically methylate McpS and McpT. It is involved in chemotaxis, whereas CheR1 is required for biofilm formation (García-Fontana et al., 2013). CheY paralogues often serve as phosphate sinks in competition with the motor binding CheY variant and aid in signal termination (Krell et al., 2010). In *Sinorhizobium meliloti* for example, CheY2 is mainly responsible for the regulation of the chemotactic response, while CheY1 apparently competes with CheY2 for phosphorylation by CheA.

2.3.3. Temporal response

For concentrations below the saturation of the chemotaxis system and at low gradient strengths, the turn rate relates linearly to the history of the attractant concentration experienced by a swimming cell. One can then derive a linear response theory were the tumbling rate $\lambda(t)$ is given by the convolution of the concentration history $c(\mathbf{r}(t))$ with the chemotactic response function $R(t)$. Gennes (2004) showed that

$$\lambda(t) = \lambda_{\mathrm{eq}} - \int_{-\infty}^{t} R(t - t') \cdot c(\mathbf{r}(t')) \, dt' \, , \tag{2.5}$$

were λ_{eq} is the equilibrium turn rate without and attractant, $c(\mathbf{r})$ the concentration field and $\mathbf{r}(t)$ the position of the cell. The "memory" of past attractant concentrations which is contained in the different phosphorylation and methylation levels of the involved chemotaxis proteins is represented by $R(t)$. Its is the result of the precise concentrations and reaction rates of the relevant proteins. Segall et al. (1986) determined its shape for the attractant aspartate by analyzing the rotation of cells tethered to a cover slip, which were subjected to varying pulses of chemoattractant.

An example of response functions for typical *E. coli* cells is shown in figure 2.12. Here, the typical memory time of the signal transduction system of about 5 seconds can be seen. The time and strength of the response can, however, differ significantly throughout the population (Masson et al., 2012). This means that for gradients which
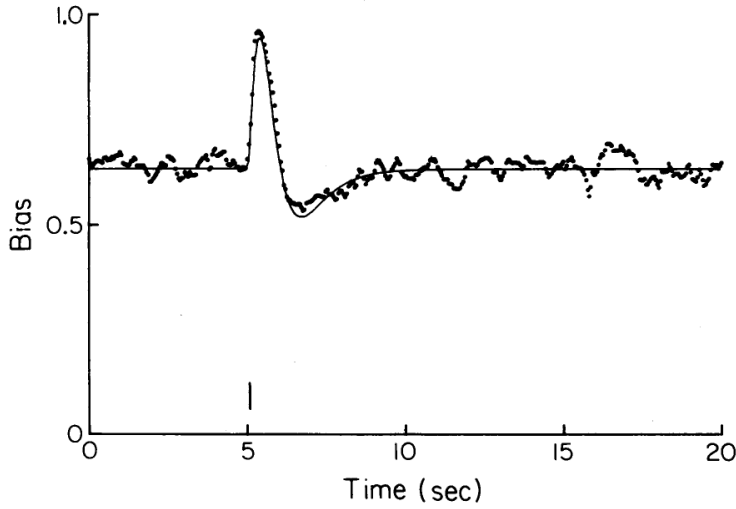
Figure 2.12.: Impulse response $R(t)$ of *E. coli* to aspartate. Shown is the bias, or probability, of counterclockwise (CCW) rotation. At $t = 5$ s (vertical line) an attractant pulse is administered. Cells respond by first reducing their reversal rate for about one second, and then increasing their reversal rate for about 3 seconds. after 4 to 5 seconds the response returns to pre-stimulus levels. Reproduced from Segall et al. (1986).

are not too steep the response of the chemosensory system is linear (Block et al., 1982). Furthermore, the run times of bacteria are usually of the same order of magnitude as the memory of the chemotactic system. This is because the direction of longer runs will decorrelate with the initial direction due to rotational diffusion (H. C. Berg, 2004).

(Clark and Grant, 2005) later could show, that the response function is mainly shaped by two conflicting requirements: moving up a gradient quickly and staying near a maximum once there. Both contributions are present in the response function shown in figure 2.12. A large positive initial component leads to a good performance when climbing up the gradient, while a transient negative response around 1 to 2 seconds leads to the ability to stay near maxima in the gradient (Clark and Grant, 2005).

In linear gradients, equation 2.5 can then be simplified by only considering the contribution of the last run to the turn rate: (Pohl et al., 2017)

$$\lambda(t) = \lambda_{\text{equ}} + K v_0 \, \cos(\theta) \int_{t_0}^{t} R(t - t') t \, dt' + \dots \tag{2.6}$$

Here, v_0 and θ are the mean run speed and the run's angle relative to the gradient, while K is proportional to the gradient strength.

2.4. Classifying runs and turns

In order to extract information about chemotactic behavior from tracks of swimming bacteria, it is necessary to classify which portions of a track represents a run, and which portion represents a turn. To this end, multiple approaches have been taken.

The first algorithm was developed by Howard Berg to analyze trajectories of swimming *E. coli* acquired with the very first tracking microscope (H. C. Berg and Brown, 1972). Because *E. coli* tumbles are accompanied by quick changes in the swimming direction, this algorithm classifies time points above a certain threshold in angular velocity as tumbles. It has been frequently used since its inception and was applied to other tracking techniques, for example (Taute et al., 2015)

An extension similar to the Berg algorithm is the one by Masson et al. (2012). Here, not thresholds in angular velocity are computed, but local maxima in the angular velocity and speed time series are explored. When a local maximum of angular velocity is significantly larger than would be expected based on angular diffusion alone, the time points close to the maximum are classified as a turn. Since tumbling *E. coli* cells tend to have a lower swimming speed, local speed minima are explored in a similar manner and also can lead to a classified turn interval, while each one of the criteria is already sufficient.

A more statistically rigorous approach was developed by (Rosser, Fletcher, et al., 2013). Using mutant strains that only turn or only swim straight, a two-state hidden Markov model was trained to distinguish between those two motion phases. This method provides a classifier robust to noise, but relies on the availability of the two mutant strains.

3. Materials and methods

3.1. Microbial culture

The focus of this work is the species *Pseudomonas putida* whose strain KT2440 is considered the wild type (wt) in the scope of this work. For staining of flagella, the derivative strain $FliC_{S267C}$ was used, where one amino acid in the flagellin protein (FliC) is changed – cysteine is substituted for serine at amino acid 267. The thiol group of the cysteine residue then enabled the covalent labeling with a fluorescent dye. We thank Marco Kühn and Kai Thormann from the Justus-Liebig-University Gießen for kindly providing this strain. Details of its construction are given in the appendix, subsection A.1.1. For *E. coli* chemotaxis and control experiments, *E. coli* K12 strain AW405 was used.

Microbial culture was similar for all strains used. A stock of isogenic bacteria was kept in a 50 % glycerol/50 % LB medium solution (20 g/l ready made LB medium, AppliChem) at $-80\,°C$. This stock solution was streaked on 1.5 % agar plates containing 20 g/l LB medium (both AppliChem, Germany) and grown in an incubator. Temperatures for incubation were $30\,°C$ for *P. putida* and $37\,°C$ for *E. coli*. A single-colony isolate from the streak plate was used to inoculate 10 ml of LB medium in a 100 ml Erlenmeyer flask, and grown over night on a rotary shaker at 300/min.

The stationary culture was diluted 1:100 fold into 10 ml of fresh LB medium and grown to mid-exponential phase. To monitor the growth of microbial cultures we used the optical density at 600 nm (OD_{600}) as a measure of turbidity. The onset and end of exponential growth phase were evaluated from growth curves of all strain and medium combinations used here. In LB medium the time to reach mid exponential phase (OD 0.7) was about 3.5 h for *P. putida* and 3 h for *E. coli*.

Before the start of experiments, bacteria were washed two times by centrifugation at 1000 g for 10 min and careful resuspension in 10 ml motility buffer (1×10^{-2} M potassium phosphate, 6.7×10^{-2} M NaCl, 1×10^{-4} M EDTA and 0.5 g/ml glucose; pH 7.0) at densities between 0.1 and 0.01 OD_{600}.

For *P. putida* chemotaxis towards benzoate, the chemosensory system for that compound had to be induced by providing benzoate as the only carbon source (Harwood, Rivelli, et al., 1984). To this end, cells were grown in M9 defined medium (48 mM Na_2HPO_4, 22 mM KH_2PO_4, 19 mM NH_4Cl, 8.5 mM NaCl, 2 mM $MgSO_4$, 0.1 mM $CaCl_2$ with 5 mM sodium benzoate. This is a minimal medium and consequently growth rates where very slow. To reach stationary phase at OD 0.7 cells had to grow for 24 h. Because of this, cultures inoculated from streak plates were directly used in chemotaxis experiments and not further diluted in fresh medium. Otherwise cell preparation was the same.

For experiments in structured microchannels, cells had to be partially grown inside the microfluidic devices used. A single *P. putida* colony grown on LB-Agar, was used to inoculate a 50 ml-flask of N-medium (5 g/l peptone, 3 g/l meat extract, adjusted to pH 7.0). This culture was incubated on a rotating shaker overnight and then diluted down to an OD of 0.1 (approximately 1×10^7 cells/ml) with fresh medium. The cell suspension was then injected into the microfluidic channel and allowed to grow there for six hours (Theves, Taktikos, et al., 2015).

3.2. Microscopy & image acquisition

All measurements were performed using an inverted wide field microscope (Olympus IX71) and recorded with a Hamamatsu Orca Flash 4.0 high speed CMOS camera. The camera was connected via CameraLink™ to a PC running Hokawo (Hamamatsu) and images were recorded onto a SSD Raid array in BigTIFF format. Up to a frame rate of 100 fps the camera is capable of recording its full field of view (2048×2048 pixels) and was used in that mode where possible. When a frame rate of 200 fps was used the field of view had to be reduced to half its full height (2048×1024) and further halved for each frame rate doubling.

The objectives used were Olympus 10×, 20×, 40×, 60×, and 100× UPlanFL N Ph. Normal cell tracking was done in phase contrast mode, while high speed imaging of flagella was done in fluorescence mode. For wide field phase contrast the depth of focus for this setup was about 5 μm and thus our recordings essentially represent thin 2D slices within the channel volume.

Observations in specially structured channels (section 4.2) were performed in bright field mode, because of excessive phase contrast halos surrounding the obstacles. In these experiments a EoSens MC 1362 camera (Mikrotron, Munich, Germany) was used in combination with the 20× objective and a 1.5× integrated lens for a total magnification of 30x. Data was recorded with 1280×1024 pixels at 50 fps.

3.3. Chemotaxis assay

A μ-Slide Chemotaxis 3D (ibidi , Germany) was used to generate stable linear gradients of the chemoattractants α-methyl-aspartate (Sigma-Aldrich, USA) for *E. coli* and sodium benzoate (VWR Prolabo) for *P. putida*. Layout and dimensions of the ibidi chamber are shown in figure 3.1. The height of the gradient region is 70 μm.

Stationarity and linearity of the gradient were checked by filling the attractant reservoir with 1 μM fluorescein and measuring the intensity profile with a confocal microscope (LSM 780, Zeiss, Germany). The resulting gradient profile is shown in 3.2. Because not all measurements could be done in the same microfluidic device, measurements at 8 and 10 min were taken from a second experiment. Since both data sets had slightly different starting concentrations, due to the manual process of filling the reservoirs, gradients in figure 3.2 were normalized to have the same intensity at 800 μm. Because of similar molecule sizes, α-methyl-aspartate and fluorescein have
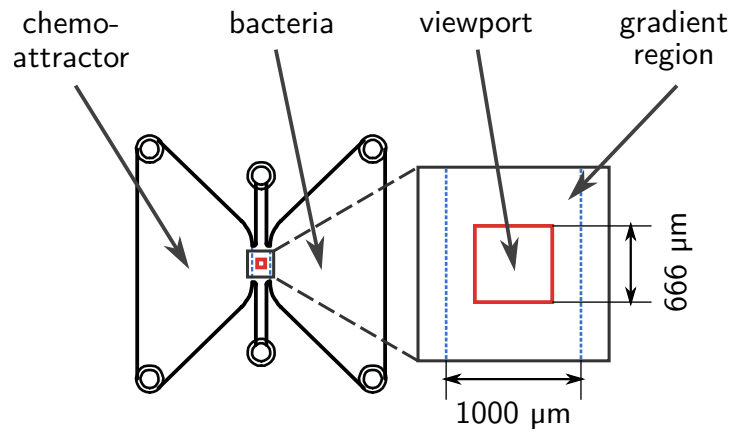
Figure 3.1.: Layout of the 'ibidi Chemotaxis 3D' microfluidic device. Attractant reservoir is on the left, cell reservoir on the right. The gradient region is marked in blue, the view port imaged by the microscope in red.
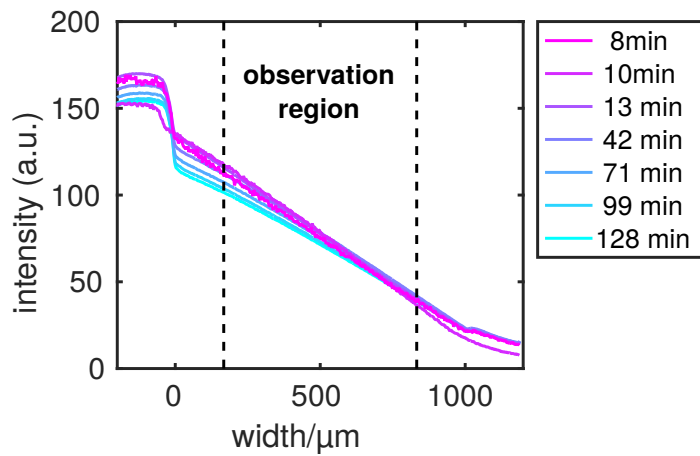
Figure 3.2.: Evolution of the gradient profile after filling the channel, normalized to the same value at $800\,\mu m$. The observation region lies between the dotted lines.

similar diffusion coefficients and it can be assumed that the gradient profile measured represents also the distribution of the chemoattractant (Ribeiro et al., 2014).

Imaging was performed with a 20× objective. The view port and focal plane were set in the center of the channels observation region, about 35 µm from top and bottom (see figure 3.1).

Cells were diluted to an OD of 0.05 before filling them into the device. Each chamber on the ibidi chip was prepared as follows: First, the gradient region was filled with motility buffer, then the cell suspension was filled into the right hand reservoir of the channel. Lastly, the left hand reservoir was filled with motility buffer containing the chemoattractant – α-methyl-aspartate in the case of *E. coli* and sodium benzoate in the case of *P. putida*. Different concentrations of attractants were used, ranging from 0.5 mM/mm to 5 mM/mm for *E. coli* and from 0.5 mM/mm to 50 mM/mm for *P. putida*.

In order to determine a time point with a sufficient amount of motile cells for the *E. coli* experiments, video sequences of 2 minutes each were recorded at 7, 12, 30, 45, 60 and 95 minutes after filling the channel. The video frame rate was 25 Hz. For *P. putida* experiments the videos were recorded approximately 15 minutes after filling at a frame rate of 20 Hz.

After tracking bacteria in the video recordings, we applied our heuristic run-and-tumble classification algorithm (see section 3.8.1), as well as the method of conditional moments described in section 2.4 and (Pohl et al., 2017), as an alternative classification scheme.

3.4. Adaptation assay

Bacteria were grown in one of two media described above, depending on the chemoattractant used. M9 medium with benzoate as a carbon source was used for benzoate assays and LB medium for the casamino acids assays. In preparation for the assay, they were washed free from the growth medium by centrifugation and diluted in motility buffer with glucose to an OD of 0.05. During this step benzoate or casamino acids were added to reach the desired final concentrations (see Appendix, table A.1).

For each attractant concentration, 500 µl of cell suspension were introduced into a well of a glass bottom, black, polypropylene, 96 well plate. In order to limit evaporation driven flows during the following observation, the open volume between and around the wells was filled with distilled water and a lid was placed on the microwell plate. If a flow was still visible in the system, the lid was additionally sealed with parafilm. The cell suspension was then allowed to settle and adapt to the buffer solution for 15 min. Finally, videos were recorded sequentially for 2 min to 2.5 min in each well. Imaging was carried out in the center of each well with the 20× Olympus objective at 20 Hz. In order to avoid hydrodynamic interaction of cells with surfaces, the focal plane was chosen 30 µm to 50 µm above the bottom glass.

The experiments on the adaptation to homogeneous stimuli of chemoattractant were mostly performed by Veronika Waljor, whose Bachelor thesis I supervised.
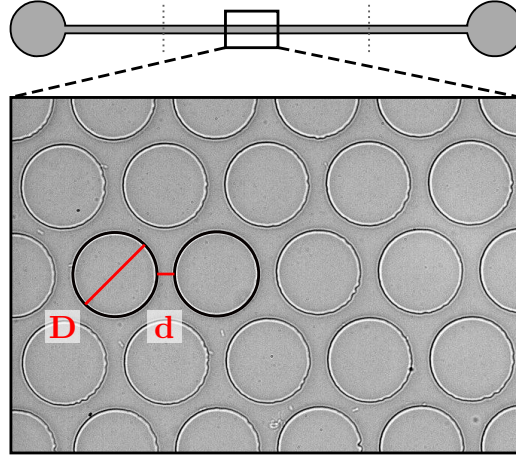
Figure 3.3.: Geometry of structured microfluidic channels. Obstacle diameters ranged from $D = 25\,\mu$m to $100\,\mu$m and inter obstacles distance were $d = 5\,\mu$m, $10\,\mu$m and $20\,\mu$m. Reproduced from Raatz et al. (2015) with kind permission of The European Physical Journal (EPJ).

3.5. Structured environments

Microfluidic channels were fabricated from polydimethylsiloxane (PDMS) using standard soft lithography protocols (Xia and Whitesides, 1998). For structured environment assays, channels measuring $30\,\text{mm} \times 500\,\mu\text{m} \times 5\,\mu\text{m}$ were used. They contained cylindrical obstacles arranged on a regular hexagonal lattice, shown in figure 3.3. Three regions with different obstacle distances (d) where present in every channel: $5\,\mu$m, $10\,\mu$m and $25\,\mu$m. Of those, four different channel types with obstacle sizes (D) of $25\,\mu$m, $50\,\mu$m, $75\,\mu$m and $100\,\mu$m were fabricated. This enabled us to measure motility statistics in 12 different environments with porosities ($V_{\text{void}}/V_{\text{total}}$) ranging from 0.17 to 0.72.

In contrast to the other experiments in this work, cell where first grown in shaking culture with N-medium as described above, and then injected into the structured channels. There, the cell suspension was incubated in situ, at room temperature, for six hours. After this time period a sufficient number of swimming cells had developed (Theves, 2013) and microscopic observation was started. The video imaging was performed with the $20\times$ Olympus objective in bright field mode at $50\,\text{Hz}$.

The experiments were performed by Marco Bahrs, whose Bachelor thesis I co-supervised.

3.6. High speed imaging of flagella

One of the main challenges of this thesis was to perform high speed observation of swimming *P. putida* bacteria. We therefore combined established flagella staining

protocols with a custom combination of a high speed camera and a high power wide field LED illumination.

3.6.1. Labeling

To make the flagella of *P. putida* visible for direct microscopic examination, fluorescent staining protocols developed for *E. coli* were adapted from Turner, W. S. Ryu, et al. (2000) and Turner, Zhang, et al. (2010). Results reported in this work, were achieved by labeling *P. putida* KT2440 (wt) with NHS functionalized dye, and later by labeling the mutant strain *P. putida* KT2440 FliC$_{S267C}$ with maleimide functionalized dye. For a detailed description of the technique used to create the strain see the appendix, subsection A.1.1.

The wild-type was grown in LB medium, while FliC$_{S267C}$ was grown in Tryptone broth (10 g/l tryptone (AppliChem), 5 g/l NaCl) at 30 °C on a rotary shaker at 300 rpm. LB grown cultures exhibited the best motility at an OD of 1 , to 1.5 , corresponding to the transition to stationary phase. Cultures grown in Tryptone broth were highly motile in stationary phase when incubated overnight and where used thus. 10 ml to 25 ml of cell suspension from the shaking culture was then washed by centrifugation (2 min to 3 min, 3000 g) up to three times using motility buffer with glucose. During the last washing step the cell suspension was concentrated 10-fold to 1 ml in a 1.5 ml micro tube. The dye was then added to the concentrated cell suspension: 50 µl of 1 g/ml Alexa 488 NHS-ester (Thermo Fisher Scientific) solution in water for wt cells or 50 µl of 1 mg/ml Alexa 488 C5-maleimide (Thermo Fisher Scientific) in DMSO for FliC mutants. Maleimide functionalized dyes had to be freshly prepared in water free DMSO and could be used for up to two weeks when stored at −20 °C. Cells were then incubated on a rocking shaker for 15 min at 40 rpm protected from light. To remove excess dye the sample was washed again at least two times by centrifugation with replacement of the supernatant with fresh motility buffer. Samples where used immediately after staining because motility declined within half an hour for LB grown cells. For tryptone grown cultures motility declined much slower and was still present after up to 5 h after preparation of the sample. Addition of fresh Tryptone broth to a final concentration of 1:10 or 1:5 to the washed cell suspension in buffer resulted in an even higher motility and was performed if too few swimmers could be observed.

3.6.2. Microscopy

For high speed fluorescent imaging of swimming cells with stained flagella (section 4.1), a 100 W mercury arc lamp (U-LH100HG, Olympus) was used initially as an excitation light source. This was sufficient for about 50 fps corresponding to exposure times of 20 ms. For higher frame rates a high powered blue LED light source (Prizmatix UHP-T-LED-470, Mountain Photonics GmbH, Germany) with 4.8 W optical output power at 470 nm had to be used, enabling frame rates up to 600 Hz in combination with the Hamamatsu Orca Flash 4.0 CMOS camera. In stead of the Olympus 40× objective, a Zeiss Fluar 40× 1.3 NA oil immersion objective was used because of its
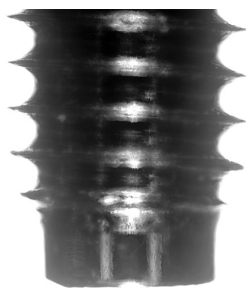
Figure 3.4.: Image of a right hand machine screw. The right hand thread of the screw
appears left handed, due to the z-inversion.

superior numerical aperture and thus higher light gathering ability for our low intensity
fluorescent objects.

Image orientation Special care must be taken when observing 3D structures through
a microscope, because it changes certain aspects of spacial orientation of the specimen.
The inverted microscope used in this work projects an image onto the camera and
through the oculars that appears as if looking from above onto the specimen. We
verified this fact by painting a pattern on a glass cover slip and imaging it ink-up
on the microscope. Because the microscope is inverted, the objective is below the
sample, looking upwards at the bottom of the slide (Murphy, 2002). It therefore has
to form an image of the specimen which is inverted along the z-axis, compared to an
observer sitting in front of the sample looking downwards. The handedness of a helix,
however, is not conserved by this image transformation. This fact was experimentally
verified by imaging a standard machine screw with a right-handed thread, whose
image as produced by the microscope is that of a left-handed thread (figure 3.4). Our
observations of fluorescent flagella therefore appear with the opposite of the true sense
of helix handedness.

3.6.3. Post processing of high speed fluorescence data

To process and analyze the high speed fluorescence data, an ImageJ (Schneider et
al., 2012; Schindelin et al., 2015) macro was written to enable an efficient manual
extraction of the relevant portions from the up to 300.000 frames of each recording.
Depending on the frame rate, 1 min to 5 min recordings resulted in stacks of 5000 to
30 000 images (50 GB to 300 GB). The resulting image stacks often contained only a
few swimming cells. Using our custom ImageJ macro, the maximum projection for
sub-groups of 300 to 600 images from the original stack were calculated with 10 to
20 frames overlap. Fluorescent cells leave bright streaks in this projection, see for
example figure 3.5. Relevant spatio-temporal regions from the original stack were
then selected manually and extracted to substacks in ImageJ. Those substacks which
contained swimming bacteria where saved, the rest of the large original stack was
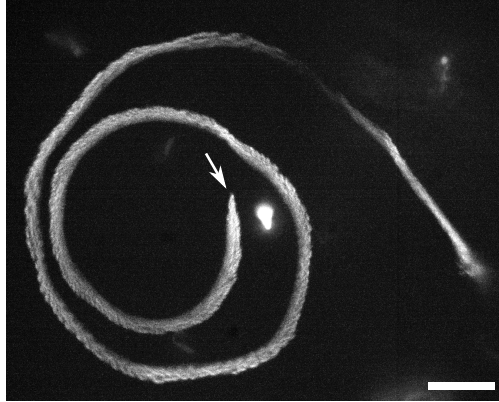
Figure 3.5.: Maximum projection of a swimming cell. The start of the streak is marked by the arrow. Scale bar is 10 µm.

discarded because it did not contain relevant information and because of the high memory requirements.

Runs, tumbles, and more general transition events were then classified by manual inspection and compiled into a spread sheet catalog. From this catalog, statistics of the observed patterns in the flagellar dynamics were calculated directly within the spread sheet.

3.6.4. Speed analysis

The high speed recordings of fluorescently stained bacterial swimmers was near the limits of the available setup, and thus our recordings have low signal to noise ratios (SNR). Most structures such as cell bodies and flagella achieve a SNR of ~ 0.1 to 0.2 and relevant features could just be made out by eye. Because of the low SNR, the usual segmentation algorithm could not be used for object detection. In order to evaluate the speed of portions of the trajectories, path lengths and time intervals between transitions were measured. This was again based on maximum projected paths, of which the contour length of relevant portions were measured using ImageJ's segmented line tool. The resulting data was analyzed and ploted using custom Matlab scripts.

Despite the difficulties with the normal object detection, some cells could be tracked using ImageJ's 'TrackMate' plugin. It uses the 'Laplacian of Gaussian' approach for image edge detection and segmentation. Linking of components is based on the LAP algorithm, see Tinevez et al. (2017) for details. Parameters for the tracking plug-in where chosen on a case by case basis to achieve optimal results. Typical values were: blob size = 3.5 µm, threshold = 0.05, maximum linking distance = 1 µm and maximal gap closing = 2 to 5. The extracted tracks could then be fed into our Matlab program for automated trajectory analysis as described in section 3.7.
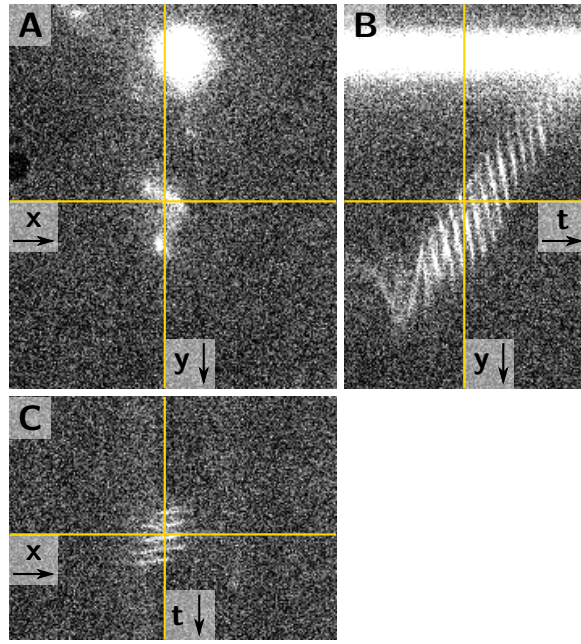
Figure 3.6.: Method used to measure flagellar rotation frequency. Image stack of a cell swimming upwards, along the -y direction.
A) single frame snapshot, **B)** and **C)** kymographs along the y- and x-direction, respectively. The yellow lines in **A)** mark the directions along which the kymographs **B)** and **C)** are calculated.

3.6.5. Frequency analysis

For some cells swimming in wrapped mode we were able to measure the apparent rotation frequency of the flagellar bundle. To this end, a selected portion of a run was used to generate kymographs, which shows the intensity variation over time along a line in the image coordinate frame.

Kymographs were generated with ImageJ's 'orthogonal views' tool. It allows one to select a point in the image through which two kymographs, one in x- and one in y-direction, will pass. Figure 3.6 shows an exemplary episode with corresponding kymographs in x- and y-direction. Shown in yellow in figure 3.6A are the two kymograph axes. Along each line one kymograph is computed – (x→) in panel B and (y↓) in panel C. Each kymograph shows the temporal evolution of all pixels along the corresponding spatial axis. The periodic rotation of the bundle results in an intensity variation along the temporal axis of the kymographs.

We counted the number of distinguishable intensity peaks n_{peaks} over a time interval T_{peaks}. The rotation frequency was then given by $f = n_{\text{peaks}}/T_{\text{peaks}}$ and the results were evaluated in a spread sheet.

3.7. Automated image processing & cell tracking

Raw camera images from tracking experiments were processed with a custom Matlab program which could perform all of the required data analysis steps:

- Image preprocessing, thresholding and segmentation
- Identification of connected components by leveraging Matlab's Image Processing Toolbox
- Filtering out unwanted image components
- Cell tracking based on the particle tracking algorithm by Crocker and Grier (1996)
- Post-processing of tracks, smoothing
- Run-and-tumble classification based on the algorithm by Masson et al. (2012)

as well as analysis of the acquired tracking data such as

- Calculation of motility parameters such as run speed, turning angles, etc.
- Measurement of motion biases in chemotactic fields.

An alternative manual classification of runs, reversals and stops using a custom GUI was performed for some of our experiments.

Great care was taken to adhere to best practices for scientific programming such as version control, in order to ensure reproducible results. The software package the author developed for this thesis continues to be used and extended by bachelors and masters students supervised by me, as well as fellow PhD students.

Individual processing steps are broken down and summarized in the following sections. The complete Matlab code is available upon request to the author.

Image processing   First, a background correction was performed for each time series, or stack, of images. The average projection was calculated by taking the time average of each pixel separately. This gave a good estimate of the background image B, in which only non-moving objects were visible. The correction was performed by dividing each frame I by the estimated background

$$T = \frac{I}{B} \ .$$

The result, T, is an effective transmission value because the measured intensity I is proportional to the bright field illumination intensity, which is estimated by B. This resulted in an image which was free of non-moving objects as well as of shading effects due to uneven illumination. To simplify further processing and reduce storage requirements, the 32 bit floating point transmission value was scaled back to the 16 bit intensity range of the original image. Because the whole stack did not fit in the memory of available computers, the appropriate intensity range was estimated by

performing the background correction with the minimum and maximum projection ($I_{\min}$ and $I_{\max}$) of the whole image stack

$$T_{\max} = \frac{I_{\max}}{B} \ ,$$

where

$$I_{\max}(k, l) = \max_i \sum_i I_j(k, l)$$

and $I_{\min}$ analogously. The pixel's row and column are denoted by k and l, respectively, while i denotes the frame index. The extreme values $\min_{k,l} T_{\min}(k, l)$ and $\max_{k,l} T_{\max}(k, l)$ of the background corrected projections then define the lowest and highest possible intensity values of the whole image stack, and were thus used for the rescaling of the corrected stack.

The resulting corrected image stack was segmented using our Matlab adaptation of the maximum entropy thresholding algorithm by Kapur et al. (1985). To minimize noise introduced by the segmentation, the threshold was computed for each image separately and the median of these values was then used to segment the whole stack. Small specks still present after segmentation were removed by morphological opening and closing with a disk shaped structuring element of a radius equivalent to $0.3\,\mu m$ (Gonzalez et al., 2009). Positions of cells were determined by computing the centroid of each connected component in the binary image using Matlab functions from the Image Processing Toolbox. Lastly, connected components with areas between $1\,\mu m^2$ to $15.6\,\mu m^2$ were considered as single cells, the rest were discarded from the analysis.

Cell tracking Cell tracking was based on the particle tracking algorithm by Crocker and Grier (1996). Specifically we used the Matlab implementation of Blair and Dufresne (2008). This method links cell positions in consecutive frames, so that the sum of squared distances between frames $\sum_i \delta_i^2$ is minimized. Because this is computationally costly, only candidates below a distance $l_{\max}$ are considered. This cutoff length corresponds to a maximum velocity $v_{\max} = l_{\max}/\Delta t_{\text{frame}}$ above which a cells positions can no longer be linked to a contiguous track. It was chosen so that $v_{\max}$ was $75\,\mu m/s$ for *P. putida* and $50\,\mu m/s$ for *E. coli* experiments.

3.8. Analysis of trajectories

In order to characterize and analyze the cell trajectories, the velocity and higher derivatives were estimated by finite differences as follows. For each frame i the velocity vector $\mathbf{v}_i$ to the next frame $i + 1$ was calculated by forward difference as

$$\mathbf{v}_i = \frac{\mathbf{s}_i}{\Delta t} = \frac{1}{\Delta t} \cdot \begin{pmatrix} x_{i+1} - x_i \\ y_{i+1} - y_i \end{pmatrix} \ ,$$

from the frame-to-frame displacement $\mathbf{s}_i$. The momentary speed ($v_i = \|\mathbf{v}_i\|$) and propagation angle ($\theta_i = \angle(\mathbf{v_i}, \mathbf{e}_x)$) were computed from this velocity estimate.
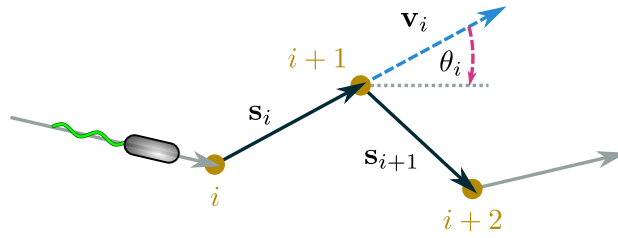
Figure 3.7.: Scheme of track analysis. The position at frame i is marked by ●. The displacement and average velocity assigned to that frame are $\mathbf{s}_i$ and $\mathbf{v}_i$, while θ_i is the angle of propagation. The direction of propagation $\angle(\mathbf{v}_i$ is measured relative to the lab frame (gray dotted line, ⋯⋯).

Filtering and smoothing Many traits relevant to bacterial motility vary from one cell to the next. To only select healthy cells, some tracks were rejected according to the following criteria. Non-moving or very slow cells were discarded below a mean speed of $10\,\mu m/s$ or if tracks were longer than $20\,s$. At the same time tracks shorter than $0.5\,s$ were also discarded, because cells swimming through the focal plane only appear briefly as a properly segmented object and not much information is contained in those very short fragments.

The remaining raw tracks contained a substantial amount of noise. Part of that can be attributed to not perfectly symmetrical cell bodies and bundle configurations which lead to a thrust vector which is off axis with the center of hydrodynamic pressure. This leads to an intrinsic curvature and torsion of the swimming path and thus produces slightly helical tracks which appear 'wobbly' in the 2D projection. Another source of noise can be the segmentation process itself and of course the Brownian motion experienced by the cell body and flagella bundle.

All of these sources of noise make it necessary to filter out some tracks in order to make a run-and-tumble detection feasible on the remaining ones. The wobbliness of tracks was characterized by their local curvature κ, which is given by

$$\kappa_i = \left| \frac{\theta_i - \theta_{i-1}}{s_i} \right| ,$$

where s_i is the displacement from frame i to $i+1$ (see figure 3.7). For each track the median curvature $\mathrm{Median}(\kappa_i)$ was calculated over all frames. Tracks were then ranked by their curvature, and the top $20\,\%$ (above the 80th percentile) were discarded. To remove noise from the remaining tracks the x- and y- coordinates x_i and y_i were smoothed by applying a 3 point, second order Savitzky–Golay filter (Savitzky and Golay, 1964). This filter was chosen in order to preserve extrema in the data, so the later tumble classification remained as precise as possible.

E. coli tracks were processed differently to be suitable for the novel tumble classification scheme of Pohl (2016). Here, the original $25\,Hz$ track data was subsampled by using only every third data point leading to an effective data rate of $8.33\,Hz$. No other smoothing was applied in this case. Bacteria in *E. coli* experiments tended to tumble

at the beginning and end of each trajectory because this is the only way to enter the focal plane. Cells swimming on a run at an angle to the focal plane only appear very briefly. Thus, the first and last $0.5\,\mathrm{s}$ of each recorded track were disregard in order to avoid artificially high tumble rates.

3.8.1. Run-and-tumble classification

Heuristic local method   After smoothing or sub-sampling, all kinetic parameters like v_i and θ_i were recomputed based on the filtered trajectories. Then, the so called turn rate ω_i was computed from the difference $\omega_i = (\theta_i - \theta_{i+1})/\Delta t$.

Instantaneous speed v_i and turn rate ω_i were then used to classify runs and tumbles, based on the algorithm from Masson et al. (2012). It identifies tumbles, or more generally reorientation events, based on variations in the speed and turn rates. First minima in speed are identified at times $t_{\min}$. Adjacent maxima are then found at $t_1 < t_{\min}$ and $t_2 > t_{\min}$. A minimum is considered a tumble if its depth $\Delta v = \max\left[v(t_1) - v(t_{\min}), v(t_2) - v(t_{\min})\right]$ satisfies

$$\frac{\Delta v}{v(t_{\min})} > \alpha \ . \tag{3.1}$$

Around a sufficiently deep minimum the cell is considered to be tumbling while

$$v(t) - v(t_{\min}) \leq \rho_v \cdot \Delta v \tag{3.2}$$

is satisfied.

The absolute value of the turn rate $|\omega|$ was then searched in analogous fashion for maxima at times $t_{\max}$ with surrounding minima denoted by $t_{1,2}$ with $t_1 < t_{\max} < t_2$. It is considered a tumble when the total angular deviation between t_1 and t_2 satisfies

$$|\theta(t_2) - \theta(t_1)| > \gamma\sqrt{D_r(t_2 - t_1)} \ , \tag{3.3}$$

which means that the observed angular reorientation is greater than the one expected due to rotational diffusion. Points around the maximum were assigned to that tumble while

$$|\omega(t_{\max}) - \omega(t)| \leq \rho_\omega \cdot \Delta\omega \ , \tag{3.4}$$

where $\Delta\omega$ is the height of the maximum defined analogously to the speed case as $\Delta\omega = \max\left[\omega(t_{\max}) - \omega(t_1), \omega(t_{\max}) - \omega(t_2)\right]$. Once equations (3.1) through (3.4) have been evaluated, all points that are identified by either the speed or the turn rate criterion are counted as tumbles.

The free parameter D_r was chosen as $0.1\,\mathrm{rad/s^2}$ so it matches the magnitude of rotational diffusion for the rod shaped cell bodies of *E. coli* and *P. putida*. The remaining parameters α, ρ_v, γ and ρ_ω are free parameters in this classification scheme. They were chosen based on literature values and adapted, so that the resulting classification agreed with the notion of tumbles present in the literature (H. C. Berg and Brown, 1972; Harwood, Fosnaugh, et al., 1989; Duffy and Ford, 1997). The resulting parameter values that were used in the following analyses are listed in table 4.5.
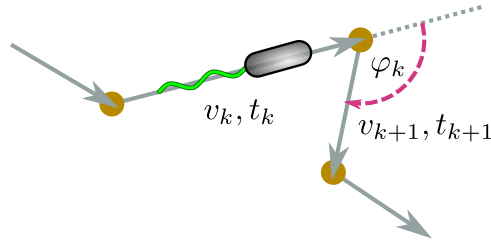
Figure 3.8.: A cell performing several runs. Runs are represented by ⟶ and tumbles are marked by ●. Mean run speed is denoted by v_k, run time by t_k and the tuning angle by φ_k.

Stop event classification Under some conditions, *P. putida* cells frequently stop their swimming motion for about a second, and then continue with their motion in approximately the same direction. This kind of 'tumbling' could not be classified with our usual algorithm but instead produced artifacts consisting of many short stops in rapid succession.

For experiments on *P. putida* adaptation (Waljor, 2016), we developed a graphical user interface (GUI) for our Matlab data analysis package. With this GUI, stop events can be marked manually and are then completely integrated into the data analysis pipeline.

3.8.2. Computation of motility parameters

After classification of runs and reorientation events, the cell motion was treated on the level of only these events. In order to examine swimming behavior and chemotaxis, run times t_k, run speeds v_k, and turning angles φ_k were measured, where φ_k is the angle between run k and the next run. Their definition is shown in figure 3.8.

The parameters which were extracted from the data are described in this section.

Mean tumble rate One measure of the response of bacteria to chemotactic stimuli is their tumbling – or more generally reorientation – rate. To compute the mean tumble rate from multiple trajectories, each track was appropriately weighted. First the tumble rate for each single track was computed

$$\lambda_i = \frac{n_i}{T_i} \, , \tag{3.5}$$

where n_i and T_i are the number of tumbles detected and the total duration of track i, respectively. Tracks without any tumbles then have a tumble rate of $\lambda_i = 0/\text{s}$. If one took the unweighted mean of these tracks, they would all count with the same weight. However, longer tracks without any tumbles should lead to a stronger decrease in the mean tumble rate than shorter ones. To take this additional information into account,

the single tumble rates were weighed with the run-time of each track:

$$\langle \lambda \rangle_w = \frac{\sum_i \lambda_i \cdot T_i}{\sum_i T_i} \overset{(3.5)}{=} \frac{\sum_i n_i}{\sum_i T_i} \tag{3.6}$$
$$= \frac{N}{T} \; ,$$

The second equality above shows that the time weighted mean is equivalent to concatenating all tracks together and then computing the tumble rate of the 'grand' track from the cumulative number of tumbles N and the total time T. In order to estimate the measurement uncertainty the weighted standard deviation

$$\sigma_{\lambda_w} = \frac{\sum_{i=1}^N (\lambda_i - \langle \lambda \rangle_w)^2 T_i}{\sum_{i=1}^{T_i} T_i} = \frac{\sum_{i=1}^N T_i \cdot \lambda_i^2}{\sum_{i=1}^N T_i} - \langle \lambda \rangle_w^2 \tag{3.7}$$

was used. In this way, information about both the distribution of single track run-times λ_i and a correct population mean $\langle \lambda \rangle_w$ was retained.

Transition rates In experiments where stops and turns were classified separately, transition rates and probabilities for run-to-stop and run-to-turn transitions and back were measured. For the underlying model see subsection 4.3.4, figure 4.32.

The rate for the transition $k \rightarrow l$ for each track i was computed as $\lambda_{i,kl} = n_{kl}/t_i$. Average weights were computed by taking the time weighted mean $\langle \lambda_{i,kl} \rangle_w$ and estimating its standard deviation as for the normal turn rate (equations 3.6 and 3.7). Mean run, stop, and turn times were calculated by unweighted average over individual run, stop, and turn times, respectively. In contrast to the rates, life times of the different states were only calculated from whole episodes, where both start and end were directly observed. That is, for example, only run with stops or turns in the beginning and end were considered for these measurements.

Mixture model for the run speed Because *P. putida* swims with two different speeds, the observed distribution of runs speeds after run-and-tumble classification is bimodal (see for example figure 4.24). In low magnification tracking experiments the swimming state of the bacterium is not known and there is significant overlap between fast and slow mode swimmers. Since many factors contribute to the actual speed of a single cell in either mode the speed distribution will be approximately normal. The resulting bimodal speed distribution can be modeled by a Gaussian Mixture Model (GMM), with one Gaussian for fast and one for slow swimming modes. The resulting probability density is given by the weighted sum of two Normal distributions $\mathcal{N}_1$ and $\mathcal{N}_2$ such that

$$\rho(x) = w_1 \cdot \mathcal{N}_1(\mu_1, \sigma_1) + w_2 \cdot \mathcal{N}_2(\mu_2, \sigma_2) \tag{3.8}$$

and $w_1 + w_2 = 1$ so that the resulting probability density is normalized.

A scheme to fit this model to the data is provided by the expectation-maximization algorithm (EM-algorithm) (Bishop, 2006). It iteratively maximizes the likelihood to

observe the measured dataset, given that it is composed of, in this case, classes with different means and variances. The algorithm provides the optimal parameter set $w_1, \mu_1, \sigma_1, w_2 = (1-w_1), \mu_2, \sigma_2$ given the available information (Dempster et al., 1977). A possible interpretation of this statistical model is as follows: randomly choose one of the available classes – in this case fast or slow – with probability w_1 for class 1 and $w_2 = (1 - w_1)$ for class two. Then choose a value according to the relevant Normal distribution $\mathcal{N}_1$ or $\mathcal{N}_2$. Based on only the outcome x one can then assign a probability that the realization belonged to class 1 or 2 (Bishop, 2006). This probability is called the responsibility of x and is given by

$$\gamma_1(x) = p(\text{class} = 1|x) = \frac{w_1 \mathcal{N}_1}{\sum_i \mathcal{N}_i} . \tag{3.9}$$

In the case of swimming *P. putida* it is thus possible to calculate the probability of a speed value belonging to the fast or the slow class.

3.8.3. Chemotactic response

In order to test for the possible chemotactic modulation of motility parameters, we conditioned some of the calculated parameters on the direction of the previous run. The run's propagation angle was measured relative to the lab frame (see figure 3.8), which was aligned with the direction of the chemotactic field.

Chemotactic index The chemotactic index (CI) was calculated in order to quantify the chemotactic response of the bacterial population as a whole. For a single trajectory i, it is defined as the ratio of the distance d_i covered along a certain direction $\mathbf{x}$ to the total path length l_i traversed:

$$\text{CI}_i(\mathbf{x}) = \frac{d_i(\mathbf{x})}{l_i} . \tag{3.10}$$

Usually $\mathbf{x}$ is chosen to be the direction of the gradient, or orthogonal to that. This is equivalent to the ratio of effective velocity in that direction over the mean instantaneous speed v because

$$\begin{aligned} \text{CI}_i &= \frac{v_i}{\langle|\mathbf{v}|\rangle} \\ &= \frac{d_i/t}{l/t} . \end{aligned}$$

Here, t_i is the total duration of trajectory i. Comparing the chemotactic index averaged over many trajectories in parallel and orthogonal direction to the gradient ($\mathbf{x} \parallel \nabla \mathbf{c}$ vs. $\mathbf{x} \perp \nabla \mathbf{c}$) yields information about the chemotactic efficiency.

Because the swimming of bacteria is governed by Brownian motion (H. C. Berg, 2004), their CI is rather low – on the order of $1\,\%$ to $10\,\%$ in the case of *E. coli* swimming in an aspartate gradient (Ahmed and Stocker, 2008). Individual tracks in

the experiments performed here are rather short, usually 1 or 2 seconds long. There-fore, individual trajectories were accumulated and the CI was computed from their population average displacement in the following manner:

$$\langle \text{CI} \rangle = \frac{\sum_i d_i}{\sum_i l_i} \,. \tag{3.11}$$

This procedure corresponds to stringing together all individual trajectories and then calculating the CI from the resulting "great" trajectory of the whole population. Sim-ilar to the mean tumble rate, it is equivalent to weighing the individual CI's with their total path length l_i:

$$\langle \text{CI} \rangle = \langle \text{CI} \rangle_w = \frac{\sum_i l_i \cdot CI_i}{\sum_i l_i} \,.$$

The resulting statistical measure is more robust to the heterogeneous population data present here and the noise due to short tracks. An example cumulative trajectory from this procedure is shown in figure 4.25. Additionally it allows the estimation of the standard deviation of the CI and thus the standard error of the mean. In this way it is possible to use the cumulative trajectory for calculation but still retain some information about the uncertainty of the quantity obtained.

4. Results and discussion

In the course of this work, the swimming and navigation of *P. putida* has been explored on different scales and in varying environments. First, we explore the causes of our model organism's unusual motility pattern by high speed fluorescent observations on short time scales. Our results are then discussed in the context of a recently emerging addition to the arsenal of bacterial swimming "styles": the wrapping of flagella around the cell body (Kühn et al., 2017; Hintsche et al., 2017; Kinosita et al., 2017). Additionally we investigate the interactions of the swimmers with artificially created obstacles and the subsequently induced changes to its motility pattern. Then we examine the chemotaxis strategy of *P. putida* by cell tracking and review the possible influences of the chemosensory system on the complex motility pattern elucidated in the previous sections. Lastly, we give an overview over a new technique used to infer the statistics of key motility parameters without relying on heuristic turn classification.

4.1. Flagellar dynamics

In this section we will present our results concerning the motility pattern and the details of *P. putida's* flagellar dynamics. Most of the findings presented below have been published in Hintsche et al. (2017).

After using an unspecific staining technique with NHS-esters on *P. putida*, we found that the cell body was very brightly stained by this procedure and outshone the dim flagella its direct proximity. Furthermore, the motility of the cells was greatly reduced, which necessitated a slightly different approach. By using the mutant strain *P. putida* FliC$_{S267C}$, kindly supplied by Prof. Kai Thormann, University of Gießen, the staining efficiency of the flagella was greatly improved, while the cell body was only stained very weakly. This mutant strain, which has a substituted cysteine residue it's flagellin subunits, enabled us to use a thiol specific dye as a fluorescent marker. By directly labeling the flagella, we were able to resolve details of the flagellar motion and dynamics in proximity to the cell body.

All of the observations in this section were only possible through the combination of a high power LED light source for fluorescence excitation and a high speed, high sensitivity camera. This method, described in more detail in section 3.6, provided sufficiently strong signals for the observations presented below. In order to analyze the large amounts of data produced and because of the sparcity of events of interest, we also developed a method to efficiently extract relevant regions in space and time. Due to the disk space requirements of the high speed imaging, only short clips of swimming bacteria could be gathered – usually one to several seconds long. Therefore, a large number of individual trajectories had to be collected for a meaningful analysis.

We observed *P. putida* in different swimming modes and were able to describe the transitions between them. In the following section we describe our findings and discuss how they relate to the previously unexplained features of *P. putida*'s motility as well as their context in the established framework of bacterial motility research.

Many of our observations are best viewed in video form. We encourage the reader to use the videos mentioned throughout this section. They are provided with the attached CD or online (see table A.3).

4.1.1. Swimming modes

To gather enough data for a confident evaluation of the swimming dynamics of our model organism we recorded around 750 individual trajectories (table A.2a). These were cataloged and manually classified into episodes according to their different swimming states. We identified three distinct swimming modes in *P. putida*: 'pulling', 'pushing', and 'wrapped'. Pushing runs account for 4/5 of the observed runs, while wrapped and pulling runs contribute equally to the rest. The relative occurrence of states in our observations is represented in figure 4.1.
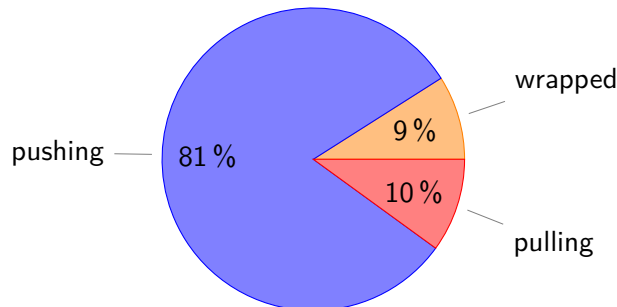
Figure 4.1.: Proportion of observed swimming states. For underlying data see table A.2a, page 96.

In all of the swimming modes cells would sometimes stop their bundle rotation for tenth of milliseconds and pause their swimming. This behavior is depicted in figure 4.2 and in this online movie. Pauses have been observed before in *P. putida* and other *Pseudomonads* (Theves, Taktikos, et al., 2013; Cai et al., 2016), but do not appear to correlate in any way to the three swimming modes. They are therefore not considered to be important for the motility or chemotaxis strategies of the *Pseudomonads* studied.
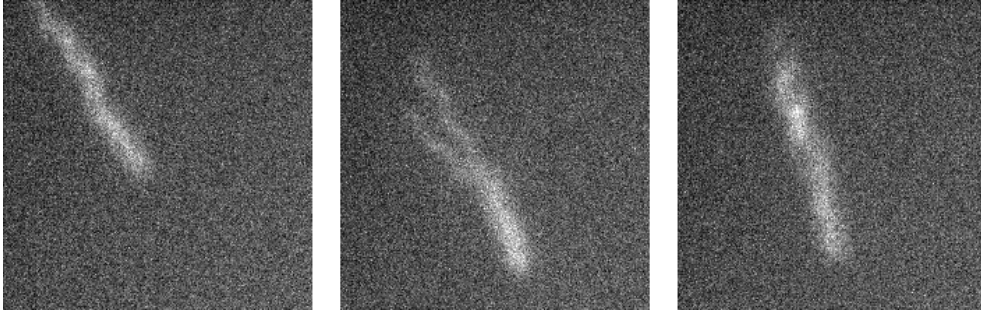
Figure 4.2.: Bundle spreading during a pause. The cell enters the frame pushing, then stops, and leaves pulling. Examples of stops can be seen in movies 6 and 7.

Pushing
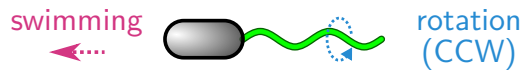
Figure 4.3.: A swimmer in pushing mode. The anterior pole is leading. The left handed flagellar bundle shown in green.

The most frequent mode we observed was the *pushing* mode. Here the flagella form a tight bundle extending away from the posterior cell pole – or back of the cell – to which they are attached. In this configuration the cell performs a run with the bundle pushing the body from behind (see figure 4.3).

Because of the small physical dimensions of the flagella and their tight bundling, we often could not distinguish between cells swimming with one or multiple flagella. However, during the frequent pausings the bundle often dispersed and we could verify the existence of multiple flagella (figure 4.2, page 41). Sometimes it was also possible to distinguish multiple flagella of the cell due to their different length and the resulting brightness variation along the bundle.

In most cases, we could not directly resolve the bundle rotation due to its high rotation speed. It therefore was not possible to directly determine the sense of rotation of the flagellar motors. However, many of the trajectories were curved (movie 1). This is due to a well known wall effect, which results form the hydrodynamic interaction of the counter rotating bundle and cell body with the no-slip boundary presented by the glass cover slip (Lauga and Powers, 2009), see section 2.2.1. All of the curved pushing trajectories were bent to the right, corresponding to a counterclockwise (CCW) rotation of the bundle (see figure 4.5a). Therefore, the flagella must form a left handed helix in order to propel the cell in the forward direction.

We found that the bundle rotates at about $200\,\mathrm{Hz}$ in some of our $400\,\mathrm{Hz}$ recordings. According to the Nyquist sampling theorem, a periodic signal can only be re-

constructed unambiguously if it is sampled with at least twice the frequency of the original signal. To make sure we were not observing aliasing effects we performed a small number of measurements at 666 Hz which confirmed the previous observations.

Pulling

Figure 4.4.: A swimmer in pulling mode. The bundle is leading before the flagellated cell pole. It is comprised of left handed flagella and is stably rotating clockwise (CW).

About 10 % of the observed runs were in *pulling* mode. Here the bundle is extended towards the front and pulls the cell body behind it, see figure 4.4). From pausings with bundle spreading, we conclude that also in this mode several flagella can form a stable bundle.

Trajectories of pullers close to the glass were always curved to the left, as depicted in figure 4.5b (see movie 2). From the same wall effect as for the pushers, we conclude that in pulling mode the flagella rotate clockwise (CW) and thus form right handed helices. The curved sections of pulling runs were, however, much shorter and over all

(a) pusher   (b) puller
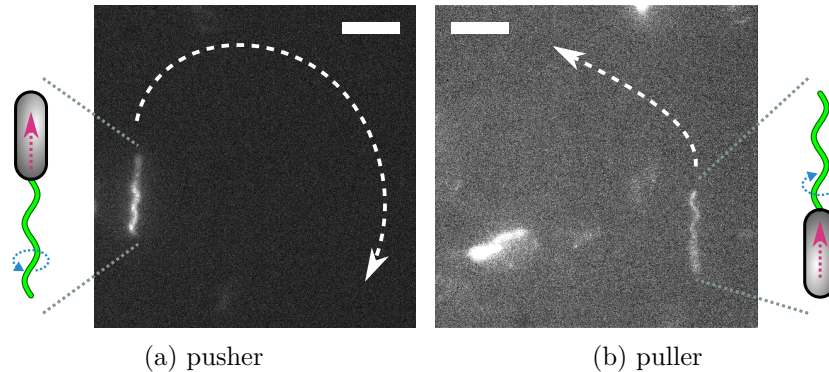
Figure 4.5.: Curved trajectories of swimming cells. Due to hydrodynamic interactions with the cover slip we can deduce the sense of bundle rotation for both modes: CCW for pushing and CW for pulling. The cell's trajectories are indicated by ![arrow], the swimming direction is indicated by -->, and the sense of rotation by -->. Scale bar is 5 µm. Both situations are available in movie form: movie 1 (pusher) and movie 2 (puller).

less frequent than the equivalent curves of pushing runs.

Wrapped
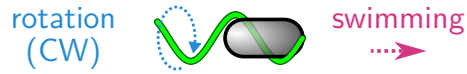
Figure 4.6.: Sketch of a swimmer in wrapped mode. The flagel-
lated pole is leading, while the bundle is tightly wrapped
around the cell body.

In addition to the two well known pushing and pulling modes, we also observed an uncommon swimming configuration, which we call wrapped mode. Here the bundle is wrapped around the cell body and the cell is swimming with its flagellated pole forward. Figures 4.7 and 4.6 show the observed arrangement. See also the corresponding recording (movie 4) of a wrapped swimmer.
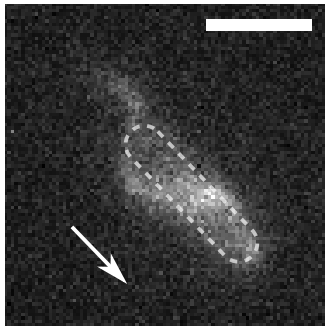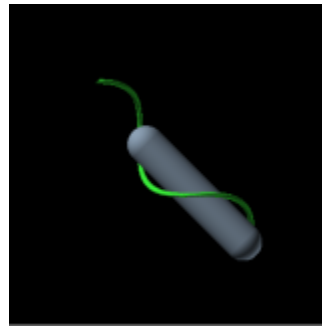
(a) fluorescence micrograph   (b) 3D representation

Figure 4.7.: Still image of a cell in wrapped state, swimming in the direction indicated
by the arrow. The geometry of body and bundle is represented in panel
(b). Scale bar is 5 µm.

Compared to pushing or pulling, the helical bundle has a larger diameter of about 1.2 µm when it is wrapped around the cell body (table 4.1), which is necessary for free rotation. The larger radius indicates a polymorphic state which is different from the normal one during pushing or pulling. Due to the similarity with a polymorphic state described in *Salmonella* (Kamiya and Asakura, 1976) and *E. coli* (Turner, W. S. Ryu, et al., 2000) we call this form *semi-coiled.*

Table 4.1.: Helix parameters of the two polymorphic states.

state	pitch/µm	diameter/µm
normal	2.0 ± 0.1	0.8 ± 0.2
semi coiled	2.1 ± 0.3	1.2 ± 0.2

4. Results and discussion

In contrast to the other two modes, wrapped cells did not show any systematic curvature of their trajectories when close to the cover slip. However, because of the larger diameter of the helical bundle, we could directly observe the handedness of the flagellum in the following way. For objects with have a thickness that is comparable to the focal depth of the microscope optics, it is not possible to distinguish the front and back of an object in a wide field micrograph. But when recording close to the cover slip ($\sim 1\,\mu m$ to $2\,\mu m$), we sometimes observed wrapped cells swimming in and out of focus. Because of the proximity of the focal plane to the cover slip their motion had to be directed toward the glass for cells coming into focus and away from the glass for cells going out of focus. Thus it was possible to infer the z-direction in relation to the cover slip. We observed the orientation of the front helix windings (close to the objective), as they appeared in focus first (figure 4.8, as well as movies 21 and 6. They are slanted to the *right*, which would corresponds to a right handed helix. Because the microscope inverts the z-dimension of the image (see Background, section 3.6.2), the helix is *left handed* in object space. Afterwards, the back windings would come into focus. Their opposite orientation confirmed our result. Since the bundle is left handed

(a) original micrograph (b) with helix superimposed
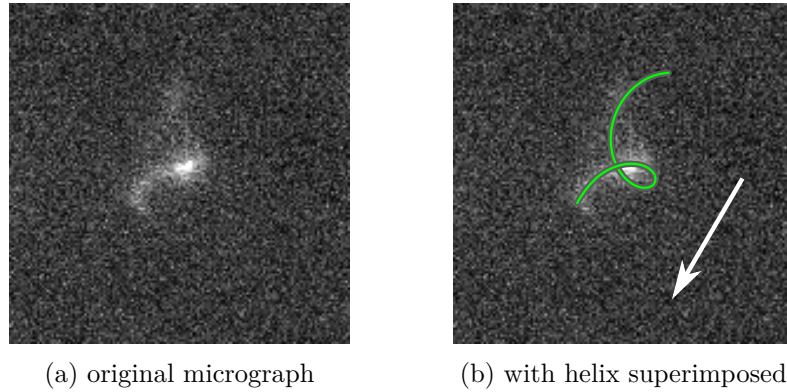
Figure 4.8.: Helix handedness in the wrapped state. Fluorescence micrograph of a wrapped cell swimming towards the objective and towards the bottom left (white arrow). Only the front windings of the helical bundle are in focus. The helix appears right handed – note the apparent handedness reverses due to the microscope optics (section 3.6.2). This still image was taken from movie 21.

in this mode, it must be rotating clockwise for the cell to move in the direction of its flagellated pole.

Here, we could completely resolve the rotation of the bundle in time, since it was much slower than in the extended flagella modes. Thus, we were able to measure the rotation frequency of the flagella for several wrapped swimmers because it was well below the Nyquist frequency of the recording setup. We measured the apparent rotation frequency from motion kymographs of several wrapped swimmers, see subsection 3.6.5 for details of this method. The mean value determined from 19 cells was $(47 \pm 14)\,Hz$ with values ranging from $20\,Hz$ to $69\,Hz$.

It should be noted however, that the observed rotation speed in the laboratory frame is not equal to the motor rotation speed. Firstly, we measured the apparent rotation rate of freely swimming cells and therefore observe a mixture of the rotation and the forward movement. *E. coli* and *V. alginolyticus* travel forward 8 % and 7 % of the flagellar pitch length per rotation (Magariyama et al., 1995; Darnton, Turner, et al., 2007). Therefore, we estimate that our observation underestimates the actual rotation rate on the order of 10 %. Secondly, the bundle and the cell body counter rotate (see subsection 2.2.1). By using the torque balance (equation 2.3) and motor rotation frequency (equation 2.4), the motor rotation speed can be expressed by the measured flagella rotation speed and the drag ratio of bundle and cell body:

$$\omega_m = \omega_f \cdot \left(1 + \frac{\gamma_f}{\gamma_b}\right) .$$ (4.1)

Measurements of the two rates in *E. coli* show that the body drag is typically much larger than the bundle drag. *E. coli's* bundle rotates with around 120 Hz while the body rotates with about 20 Hz (Chattopadhyay et al., 2006). *P. putida's* body and flagella in extended mode are about the same size as they are in *E. coli*. In wrapped mode the flagellum is somewhat larger, but it is still about the same size as the body. Thus it is reasonable to assume, that $\gamma_b \gtrsim \gamma_f$.

Together with strictly positive drag coefficients, equation 4.1 gives a bound for the motor rotation rate: $\omega_f < \omega_m \lesssim 2 \cdot \omega_f$.

This means that the measured 50 Hz are in fact a lower bound on the motor rotation frequency in the wrapped state. The true motor speed must therefore lie between 50 Hz to 100 Hz and is slower than in the extended modes by at least a factor of two.

Corresponding to the reduced motor rotation frequency, cells also swam slower in wrapped mode. From 31 trajectories with sufficient resolution we measured 61 run speeds and calculated the mean swimming speeds: (15.5 ± 0.2) µm/s in wrapped mode, (25.4 ± 0.4) µm/s in pushing and (29.0 ± 1.5) µm/s in pulling mode, respectively (figure 4.9). The Wilcoxon rank-sum test indicates that the pushing and pulling run speeds have a significantly different median ($p = 0.05$) compared to the wrapped run speed.

An example track which exhibits the speed changes characteristic for *P. putida* is shown in figure 4.10.
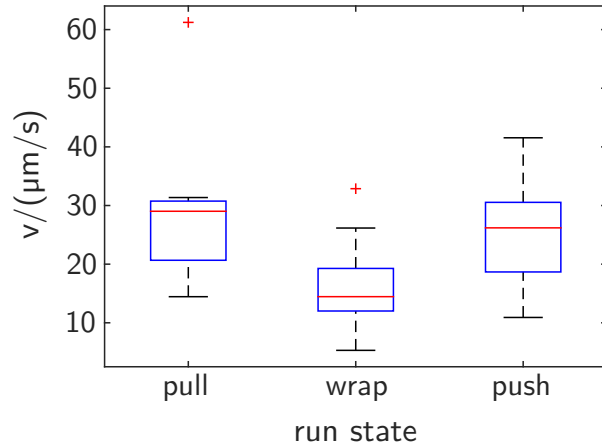
Figure 4.9.: Average run speeds in different swimming states.
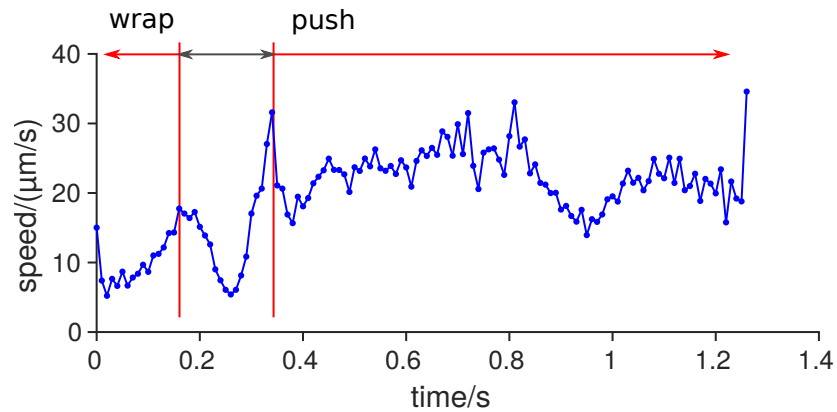
Figure 4.10.: High resolution speed time series of a swimming cell. The cell enters the focal plane in wrapped mode, unwraps its flagellum, and continues in pushing mode until it is out of focus again. This trajectory was obtained from a raw image stack with the ImageJ TrackMate plugin. Time resolution is 10 ms (frame rate 100 Hz). (Available as movie 20 on the CD.)

4.1.2. Transitions

Within all the recorded trajectories from our catalog, we could evaluate around 270 transitions between the different swimming states (table A.2b). Of the possible six transitions between states, only three could actually be observed. We found sharp reversals where the swimmer switches from push to pull and vice versa, transitions from pull to wrap and transitions from wrap to push. The proportions of observed transition were similar for all types and are shown in figure 4.11a.

transition	mean/ms	n
wrap→push	77 ± 4	10
pull →wrap	65 ± 7	7
push→pull	25	7
pull →push	117 ± 16	1

(a) Relative frequencies of transitions. For underlying data see table A.2b, page 96.

(b) Durations of different state transitions
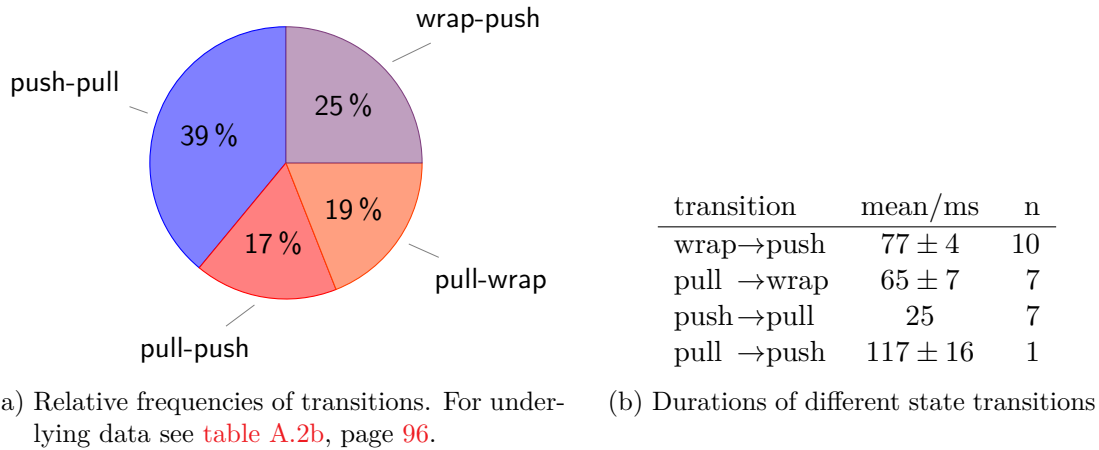
Figure 4.11.: Distribution and durations of observed transitions

Reversals
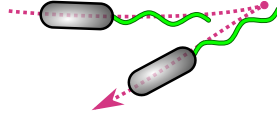
Figure 4.12.: Pull to push transition (reversal). The mean turning angle is $\langle \Delta\varphi \rangle = 180°$ and the swimming speed stays constant on average. A reverse transition from push to pull is also possible.

The transitions observed most frequently occurred from pull to push and push to pull. Here cells perform a rapid reversal, which was about as fast as the time resolution of our recordings. A recording of this behavior is available as movie 3. From the trajectory curvatures described above, we know that these reversals correspond to a switch in the sense of motor rotation. Push to pull corresponds to a switch from counterclockwise to clockwise and pull-to-push vice versa.

Observation of the bundle revealed that it usually stayed completely intact and did not visibly break apart (see movie 8). This means that all motors must be reversing their sense of rotation in a synchronous fashion.

In a few instances, a wave could be observed traveling from the proximal to the distal end of the bundle. This process seemed to coincide with the moment of motor reversal. We believe this to be a bending wave traveling up the flagella from the point of highest torque at the proximal end to the point of lowest torque at the distal end.

During a reversal, the orientation of the cell body and the bundle does not change. Because only the direction of thrust reverses, the transition has a mean turning angle of $\langle \varphi \rangle = 180°$. It is not associated with a speed change, since pushing and pulling have, on average, the same speed. Rarely, we also observed a brief pause of the motor

rotation before a reversal, which lasted only a few milliseconds.

Pull to wrapped

Figure 4.13.: Pull to wrapped transition. The mean turning angle is
$\langle \varphi \rangle = 0°$ and the swimming speed decreases.

Cells in pulling mode were also observed to transition into wrapped mode. Here the cell body briefly paused its translation and a strongly curved bend formed at the proximal end of the extended bundle. Its curvature then increased, pulling the whole bundle toward the cell body. Further rotation wrapped the bundle completely around the body, and the cell continued on the next run in wrapped mode. This process, which we call "flip over", is illustrated in figure 4.14 (also see movie 9). A more detailed view
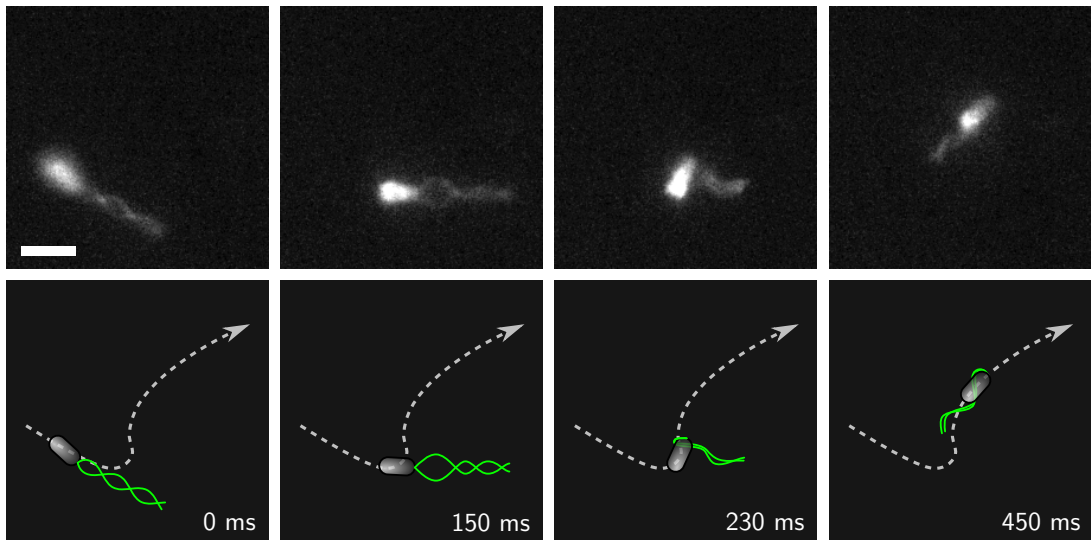
Figure 4.14.: Transition from pulling to wrapped mode. The dashed line shows the cell track, scale bar is $3\,\mu m$

of the transition dynamics is shown in table A.2.1 and movie 10. Here a cell which is stuck to the glass, but can freely move its flagellum, undergoes several transitions from pull to wrapped and from wrapped to push. In most cases the bundle stayed coherent throughout the whole maneuver, with all motors switching their rotation synchronously. On average the transition took about $70\,ms$ (figure 4.11b). Sometimes however, not all motors switched at the same time and we could verify the existence of

multiple flagella in the bundle. This means that most of the time all flagella changed their state in a synchronous manner.

As described above, the bundle rotates clockwise before and after the transition. Its physical conformation, however, changes during the transition, which indicates that a polymorphic transition must take place. This means that the flagella change from a "normal" to a "semi-coiled" conformation. Despite that transition, their handedness stays *left handed*. Interestingly, this polymorphic transition cannot rely on a change in the motor rotation sense, because only the rotation speed and thus the magnitude of applied torque are changing. We also observed some slow swimmers, where the flagellum relaxes from a normal conformation to a semi-coiled one, without the flagellum flipping over the body (see movie 13). This indicates that the torque change underlies the polymorphic transition, but is not sufficient for the complete flip over.

Because cells swim with their flagellated pole in front, before and after the transition, the turning angle between incoming and outgoing runs tends to be small and centered around zero. The mean turning angle for this transition is $\langle \varphi \rangle = 0°$, while the speed changes from fast to slow.

We never observed a transition back from wrap to pull. A few recordings, however, revealed very short series of wrapped-push-pull transition sequences. Here, a very short pushing episode occurs in between the wrapped and the pulling states at the start and end of the maneuver. When recording with a lower time resolution – typically 20 Hz for tracking experiments – an effective back transition form wrapped to pull would be observed. These effective transitions would also have a mean turning angle of $\langle \varphi \rangle = 0°$, while the speed of propagation changes from slow to fast.

Wrapped to push
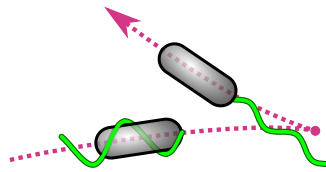
Figure 4.15.: Wrapped to push transition. The mean turn-
ing angle is $\langle \varphi \rangle = 180°$ and the swimming
speed increases.

The third transition we observed was from wrapped mode to pushing mode. An example time series is depicted in figure 4.16 and shown in movie 11. Upon switching of the motor rotation, a small loop develops at the proximal end of the semi-coiled flagellum. The loop grows and pulls the bundle away from the body, while the counterclockwise rotation unwraps it further (fig. 4.16, frame 2). When it has unwrapped, the flagellum – now in normal conformation – whips away from the body (fig. 4.16, frame 3). Usually it performs a few oscillation cycles until it extends away straight from the body again (fig. 4.16, frame 4). As before, the dynamics are visible slightly
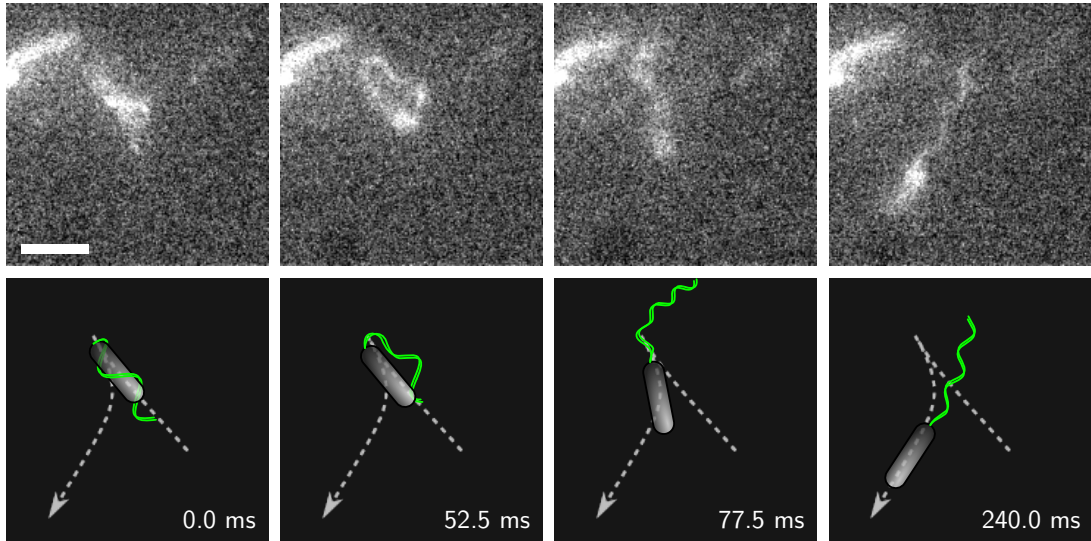
Figure 4.16.: Transition from pulling to wrapped mode. The cell enters the frame in wrapped mode. Around 50 ms the bundle rotation reverses and the flip over of the flagellum is initiated. The dashed line shows the cell's trajectory, scale bar is 3 µm. (Available as movie 11.)

better with a cell which is stuck to the glass. This is shown in figure A.2.1 and movie 12. Most of the cells which performed this transition switched the whole bundle in a synchronous manner. This could be deduced from cells which paused or sometimes did not exhibit complete synchrony during transitions. Here, it was evident that more than one flagellum was part of the bundle, which confirmed these observations (see movies 6 and 7). The whole maneuver took about 70 s, similar to the pull-to-wrap one (table 4.1).

From the previous observations of the swimming states it is clear, that the bundle switches from the semi-coiled, wrapped state and clockwise rotation to the normal, extended state and counterclockwise rotation. The flagellum handedness does not change during this process and it stays left handed. Thus the polymorphic transition of the flagellum is induced by the change in motor rotation, as has been observed for other bacterial swimmers.

Cells enter this transition with their flagellated pole in front and leave it with that pole in the back. Thus, the turning angle of this transition is centered around $\langle \varphi \rangle = 180°$. Due to the complex mechanics of the unwrapping and extending bundle, the angle distribution will presumably be broader than for the reversal. At the same time the run speed changes from slow to fast.

4.1.3. Discussion

High speed fluorescent imaging of motile *P. putida* revealed three distinct modes of propagation: pushing, pulling, and wrapped swimming. In all of these modes the

flagella are always in a left handed conformation. A graphical summary of the motility pattern is shown in figure 4.17.
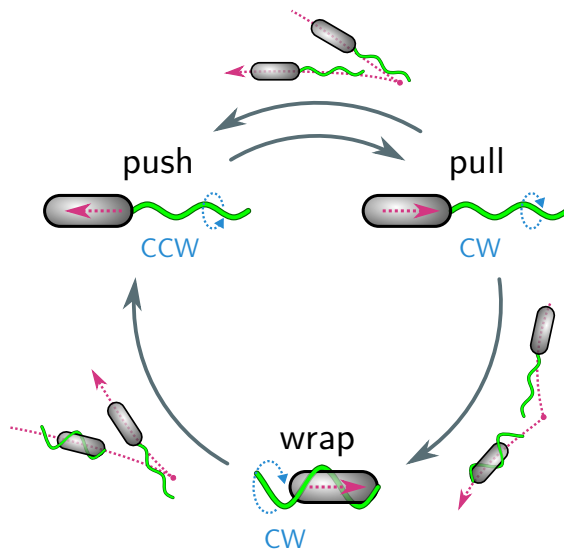
Figure 4.17.: Summary of the motility pattern of *P. putida*. All three swimming modes are shown together with the corresponding bundle configuration. Possible transitions are indicated in gray with resulting trajectory motifs shown next to them. Stops are possible in all modes.

We will now discuss how our results relate to the existing literature framework. Previous studies from our group have raised several questions concerning the motility pattern of *P. putida*. One of the first questions posed was, how a bacterium with multiple flagella in one polar tuft can perform instantaneous 180° reversals without any apparent tumble motion. The reason this was not clear was that earlier studies on peritrichous bacteria had shown that its bundle is only stable during counterclockwise rotation while the flagella are in left handed configuration, i.e. in pushing mode for *E. coli* and *P. putida* (Macnab, 1977; Kim et al., 2003). Similarly the different run speeds of *P. putida* had been noted but not been explained sufficiently (Theves, 2013). Different hypotheses have been presented in order to explain the observed behavior (Theves, Taktikos, et al., 2013; Raatz et al., 2015). Here we will address these open questions as well as the previously formulated hypotheses.

Pushing is the best studied mode of bacterial swimming. The pushing mode we describe here for *P. putida* is almost identical to the usual run mode of *E. coli* and other multitrichous bacteria like *Salmonella*. Our model organisms shows the same left handed flagellar bundle, and thus must have the same counterclockwise rotation sense of the helices. Other monotrichous bacteria like *P. aeruginosa* and *V. alginolyticus* are other well-studied examples of this form of propagation, which is a common motif in bacterial swimming.

Pulling was observed only in one out of ten runs. Because of the hydrodynamic wall effect described in section 2.2.1, pushers can swim stably in parallel orientation to a wall. Pullers in contrast, are unstable in this configuration and are driven into an orthogonal orientation when close to the wall (Lauga and Powers, 2009). This explains why we observed very few pullers close to the cover slip. Those who were recorded, stayed in this region only short periods of time.

Monotrichous bacteria are known to change from pushing to pulling and vice versa. The theory behind this mechanism is well known (Lauga and Powers, 2009). Because of the time reversibility of the Stokes-equation, reversing the rotation sense of a single flagellum will propagate it through the fluid in the opposite direction.

For bacteria with multiple flagella, the situation is much less clear, because interactions between the flagella play a major role. Because of observations in *E. coli* an entire bundle of multiple flagella was often assumed to be unstable in pulling configuration Macnab (1977). Normally *E. coli's* bundle becomes unstable when one motor reverses its sense of rotation, as this separates that flagellum form the pushing bundle. Under certain circumstances it has been observed to reverse briefly, for example in confined environments like in swarm films or narrow constrictions (Turner, Zhang, et al., 2010). In the bulk fluid however, *E. coli* does not swim with a pulling bundle and multiple studies have concluded that this is by the mechanical interaction of the semi-rigid flagella within the bundle (Macnab, 1977; Kim et al., 2003). Therefore, *E. coli* can only perform a run when all left handed flagella rotate CCW.

Although one report has described multi flagellated bacterial pullers in the past (H. C. Berg, 1975), detailed observations of this kind of motility have not been available until now. The purple sulfur bacterium *Chromatium okenii*, for example, has a very large cell body and a bundle of multiple polar flagella. Its bundle is visible with dark-field microscopy and, according to H. C. Berg (1975), its cells performs a push-pull type reversal. This means that it also synchronously reverses all its flagellar motors, although no details of this process have been examined since. Here we showed unequivocally, that a stable pulling bundle is possible and that the pulling mode is indeed an important feature of *P. putida's* motility pattern. Why a stable pulling bundle does not suffer from the destabilizing effects observed in *E. coli* as discussed in the past, remains an open question.

The rotation speed of the motors we estimate at 200 Hz for pushing and pulling. For *E. coli*, a rotation frequency on the order of 100 Hz has been reported from optical trapping (Min et al., 2009) and high speed imaging of labeled flagella (Turner, W. S. Ryu, et al., 2000). This slightly faster motor rotation is probably a cause of *P. putida's* higher mean swimming speed.

Previous articles from this group advanced different hypotheses to explain the observed 0° and 180° events together with speed changes (Theves, Taktikos, et al., 2013). Among them was a whole-bundle push to pull scenario, which corresponds to the push-pull reversal we report here. The difference in curvature of pushing and pulling runs close to a wall, which we observed here, had been predicted earlier by (Theves, Taktikos, et al., 2015) In that study, no significant curvature differences before and after reversals was detected. Presumably, a lack of significant curvature in wrapped

mode, together with the not strictly alternating nature of the transitions, blurred the observed curvatures too much to be detected in that study.

The tracking experiments performed for the chemotaxis part of this work (section 4.3), as well as previous tracking studies (Theves, Taktikos, et al., 2013), share a number of important features. First, there are two distinct speed for the runs. In section 4.1, Flagellar dynamics, we showed that these two speeds correspond to wrapped and extend (push or pull) runs. Second, there are different kinds of transitions between runs. There are four possible combinations between mean turning angles $\Delta\varphi$ (0° or 180°) and a change in mean run speed $\Delta\langle v \rangle$. All of the previously observed

Table 4.2.: Swimming transitions and their effect on speed v and turning angle $\Delta\phi$

transition	$\Delta\varphi$	$\Delta\langle v \rangle$
push-pull & pull-push	180°	no
wrap-push & rapid wrap-push-pull	180°	yes
pause	0°	no
pull-wrap	0°	yes

combinations of turning angle and speed change can be explained by the three state swimming model we derived here, see table 4.2.

We further found that *P. putida* cells sometimes stopped their motor activity and paused their runs. During that time, the bundle often dispersed slightly and rejoined immediately when the motors resumed rotation (figure 4.2. This behavior might be related to that of *Sinorhizobium meliotis* which was shown to use a similar kind of bundle spreading as a mechanism for reorientation between runs (Armitage and Schmitt, 1997). Another organisms that uses stops for reorientation is *Rhodobacter sphaeroides*. It also exhibits a torque induced polymorphic transition were its single lateral flagellum undergoes a reversible polymorphic transition from coiled to normal form as soon as the motor starts to rotate (Armitage, Pitta, et al., 1999). Why *Pseudomonads*, which do not use their short stops for reorientation, employ them at all in their motility strategy, should be investigaed in further studies.

Wrapped mode

The third mode of flagellar propagation of *P. putida* shown here, has only recently been reported in literature. The first study to observe features related to this wrapped mode was Murat et al. (2015). There, fluorescent staining of the amphitrichous flagella of *Magnetospirillium magnetotacticum* reveals a 'parachute' configuration. Here the flagellum at the leading cell pole envelops part of the cell body. Because of a low time resolution (12.5 Hz), Murat et al. (2015) were not able to elucidate the complete dynamics of *M. magnetotacticum's* flagellar dynamics. Similar to the wrapped-to-push transitions they also observe a switch of the 'parachute' configuration to a 'tuft' which extends away from the cell body. The back transition from 'tuft' to 'parachute' takes place at the same time at the opposite cell pole (analogous to the pull-to-wrapped

transition). Therefore the parachute state is probably the same wrapped state which we report here. Ongoing research on *Helicobacter suis* shows that other amphitrichous species employ the same mode of locomotion (personal communication, Maira A. Constantino, 15 March 2017, Constantino, Sharba, et al., 2017).

Additional, indirect, evidence for the wrapped mode can be found in the literature for *Pseudomonas fluorescens*. The monotrichous cells are reported to perform forward runs with speeds of about 80 µm/s, and then 'back up' with speeds of only 20 µm/s (Ping et al., 2013, figure 1). Observations of cells close to the cover slip show strongly curved and circular forward runs, as well as non-curved 'back up' runs (Ping et al., 2013, figure 3). The characteristics of the wrapped and extended modes described here exactly match the observations in *P. fluorescens*, which is presumably also capable of swimming with a wrapped flagellum. An older report on *P. citronellis* discovered the same characteristics of slow and fast speeds coupled with sudden reversals before the advent of computerized tracking, using a strobed dark photographic streak technique (Taylor and Koshland, 1974).

More recently, a direct observation of the wrapped mode was reported by Kühn et al. (2017). Fluorescent staining of the single polar flagellum of *Shewanella putrefaciens* with a similar technique as was used here, showed a transition from pulling to wrapped mode under certain conditions. When swimming into the narrow space between an agar sheet and the cover glass in pushing mode, *S. putrefaciens* cells would briefly switch into pulling mode and then into wrapped mode. This enabled cells trapped between the two interfaces to escape the confinement.

Their observations show a left handed flagellum in all three modes, with pushing cell's flagella rotating CCW and pulling and wrapped cell's flagella rotating CW. These observations agree with our evaluation of the swimming state and the transitions that arise in these swimmers (figure 4.17). In contrast, they do not find wrapped cells swimming in the bulk fluid, but only when triggered in strongly confined spaces. The fraction of *S. putrefaciens* cells that exhibited wrapped swimming was below 5 % in low viscosity aqueous solution, but increased to 74 % when cells were subjected to increasing viscosity. Kühn et al. therefore suggest, that the increased frictional load on the flagellum causes the transitions in *S. putrefaciens*.

P. putida in contrast, frequently swims in wrapped mode in the bulk fluid. Despite the fact that all of the high speed imaging in this work had to be performed close to the cover slip, the observations in section 4.3 (see figure 4.24), as well as previous reports (Theves, Taktikos, et al., 2013), show the two distinct speeds of wrapped and extended swimming far away from any boundaries.

Similarly, Kinosita et al. (2017) discovered the wrapped swimming mode in *Burkholderia* sp. RPE64 and in *Aliivibrio fischeri*. Both species are animal symbionts. The first one lives in the gut of insects, while the second one colonizes special symbiotic organs in a squid. Because of this, the authors believe wrapped swimming to be advantageous in the mucosal environments present in the hosts' organs.

Thus, a total of three species is known to us that have been directly observed to exhibit wrapped swimming. Indirect evidence exists from four more species that probably also use this mode of propagation. All are from different orders within

the Proteobacteria, which indicates that this new mode of swimming is a widespread feature of bacterial motility.

Rotation speed and drag in wrapped mode

As we measured the apparent bundle rotation rate of freely swimming cells, two effects influence the relationship between the actual motor rotation speed and the observed rotation. Our measurement is based on the frequency of brightness fluctuations along the direction of motion of freely swimming cells (subsection 3.6.5). It therefore includes both the rotation rate of the bundle, as well as a component due to the forward motion of the swimmer. For pushing cells with the flagella in normal form, measurements on *V. alginolyticus* have shown that for each bundle rotation, the cell advances by 7 % of its flagellar pitch length (Magariyama et al., 1995). Similar observations in *E. coli* have shown 8 % in water and 18 % in an α-methyl-cellulose solution with 3-fold higher viscosity. This would mean that our method of measuring the bundle rotation rate underestimates the actual rate by the same amount, because the forward traveling of the cell body reduces the observed frequency of brightness fluctuations. In the extreme case of 100 % forward motion per pitch length, no motion of the bundle would be visible in the laboratory frame. However, as the radius of the semi coiled bundle is 50 % larger than in normal form, the deviation of apparent and actual rotation rate might be larger.

Without the above mentioned effect due to the cell movement, we were able to estimate the motor rotation frequency in wrapped mode to be between 50 Hz and 100 Hz. Chattopadhyay et al. (2006) report *E. coli* rotation rates of $f_f = 115$ Hz for the flagella and $f_b = 20$ Hz for the cell body, averaged over a population of cells. Following the line of reasoning from section 4.1.1 and equation (4.1), the drag ratio for flagella and body of *E. coli* in pushing mode is then $\gamma_f/\gamma_b \approx 1 : 5.8$. If we assume the same drag ratio for *P. putida* in wrapped mode, the actual motor speed would be around 55 Hz. Thus the observed flagella rotation speed is not significantly different from this estimate.

Because the small diameters of *P. putida's* pushing helix (about 0.8 µm) and the flagella themselves (20 nm), the bundle creates much less rotational drag than the ≈ 1 µm thick body when swimming as a pusher. In the case of wrapped swimming however, the bundle is actually larger in diameter than the cell body and, following from stokes law, the flagellar drag coefficient γ_f will increase with the square of the radius r_f. This means that

$$\gamma'_f = \frac{r'^2_f}{r^2_f} \cdot \gamma_f = \frac{(0.6\,\mu\text{m})^2}{(0.4\,\mu\text{m})^2} \cdot \gamma_f$$
$$= 2.25 \cdot \gamma_f \;,$$

where the primed values are those for semi-coiled flagella and the unprimed ones are for normal state flagella. Additionally the helix, whose arc length stays approximately constant during polymorphic transitions, shortens by about 22 % as calculated from the

geometric parameters of the helix (table 4.1). Therefore the drag will also decrease by that value. These effects are multiplicative, and so the drag coefficient about doubles ($\gamma'_f \approx 2 \times \gamma_f$). This would lead to a motor frequency in wrapped mode of $\omega_m \approx 63\,\mathrm{Hz}$. It follows from these estimates that the true motor rotation speed is about 34 % larger than the flagella rotation speed.

Because of the much grater proximity of the flagella to the body in the wrapped mode, friction between the two might become relevant. Nevertheless, when swimming in the bulk fluid this friction occurs only between body and flagella and cancels out in the torque balance equation on which the above estimates are based.

The effects of forward motion and counter rotation influence the measured bundle speed in opposite directions, and with similar sizes. We therefore assume that the true motor speed is close to 50 Hz within 10 % or 20 %.

Curvature in wrapped mode

Pushing cells normally swim in circles close to a surface. This is caused by opposing friction forces generated by the counter rotating cell body and bundle (H. C. Berg and Turner, 1990). In this work we also show that cells in pulling mode also swim in circles when they are close to a surface long enough. In wrapped mode however, this effect does not occur, as our results do not show any systematic curvature of trajectories of wrapped swimmers when close to the cover slip. A possible explanation is that the rotational flow field generated by the body is nested into the opposite rotational flow field from the flagellum. Because of the linearity of the underlying Stokes equations, these boundary effects might cancel each other out – at least far away from the swimming cell. However, a rigorous theoretical analysis of the flow field and its boundary interactions will be necessary in order to understand this swimming mode.

P. putida lives in the soil, a highly heterogeneous environment, in which there are pores and surfaces on many different length scales. Here, the wrapped conformation might enable longer straight runs close to these boundaries. This in turn could, for example, improve chemotactic efficiency, because the bacterium is able to sample larger volumes for variation of signal molecule concentrations. However, from sperm chemotaxis it is known that swimming in circles can also be employed to perform highly efficient chemotaxis (Friedrich and Jülicher, 2007). The impact of wrapped mode on the chemosensory system in porous environments should therefore be studies further. Otherwise, this swimming mode could also enable a population to spread more efficiently and explore new environments by allowing longer straight movement episodes.

Transition dynamics

Most of the transitions we observed occurred synchronously for all flagella in the bundle. This has not been observed before in multitrichous bacteria swimming in bulk liquid. In *E. coli* and *Salmonella* the motors are randomly distributed over the

cell surface and are normally only correlated through diffusion of the cytoplasmic messenger CheY, which directly binds to the motors (H. C. Berg, 2004). However, one study of *E. coli* swarming on solid surfaces reported a synchronized reversal of all flagella at the same time (Turner, Zhang, et al., 2010).

To find out how this synchronization is achieved in *P. putida* more detailed studies on a molecular level will be required. It might be possible that physical proximity of the motors in *P. putida* leads to allosteric interactions. This would enable cooperative motor switching, similar to the interaction of chemotaxis receptor cluster. These receptors are arranged in tight patches and their cooperativity leads to a higher sensitivity of the whole patch (Bray et al., 1998; Bray, 2013). If the motors of *P. putida* are sufficiently close for this kind of interaction is at present unknown. Alternatively, the coupling of motors might be mediated by the mechanical interaction of flagella.

Synchronization is, however, not perfect. In some instances not all motors switched at the same time. This leads to a somewhat chaotic swimming behavior, but after some time the unsynchronized motors do fall in line with the others movie 6.

A rather unique aspect of *P. putida's* motility pattern is that it does not follow a strictly repeating sequence. When in the pulling state, there are two possible states that a cell can transition to next. Either it reverses and continues in pushing mode, or it flips over its flagellum and continues in wrapped mode. The transition to the pushing mode is clearly triggered by the motors switching their sense of rotation. In that first case the rotation speed stays approximately the same, and only direction changes from CW to CCW.

In the second case, the direction of rotation stays CW, and only the speed of rotation is reduced. This type of swimming transition has not been observed before. All model organisms where the flagellar dynamics have been studied in such detail, e.g. *E. coli* and *R. sphaeroides*, rely on motor reversals or complete stops to achieve a change in their swimming configuration.

This raises the question of how a reduction of rotation speed can trigger the flip over of the flagella. The reduction of speed is caused by a reduction in applied motor torque. Therefore, the torsional and tensile load on the flagellum and motor apparatus decreases as well. Since the speed is the only physical parameter that changes during the pull to wrap transition it must in effect cause the flagellum to transition from normal to semi-coiled state, see figure 4.18. A high motor speed creates a high tensile load and thus may inhibit the strong bending that precedes the transition to wrapped mode. As soon as this stabilizing tensile stress decreases below a critical value, the transition to wrapped may be initiated.

The observed propagation of the polymorphic transition from its base to the tip agrees with in-silico models of polymorphic transition dynamics (Vogel, 2012; Vogel and Stark, 2013) as well as with in-vivo and in-vitro experimental studies (Turner, W. S. Ryu, et al., 2000; Darnton and H. C. Berg, 2007). The conformational change starts at the proximal end of the flagellum, where the torque is highest, and travels to the distal end, where the torque is zero. It should be investigated further, if the onset of of the strong bend at the beginning of the pull-to-wrap transition is only due to this polymorphic transition, or if other parts of the flagellar propulsion system contribute.
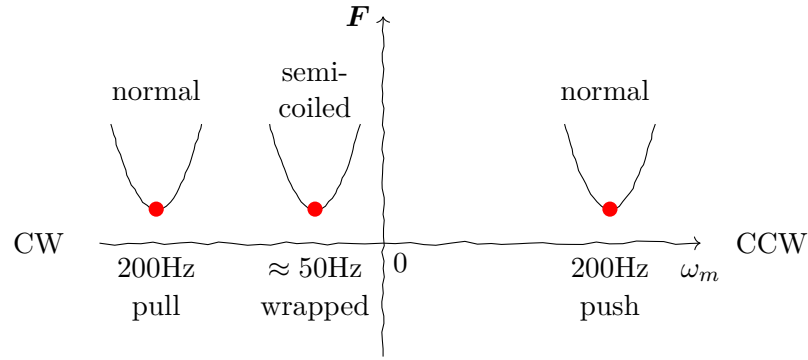
Figure 4.18.: Relation between swimming states and motor speed ω_m. The motor turns clockwise (CW) for negative values of ω_m, and counterclockwise (CCW) for positive values. Each swimming state is a local minimum of the free energy $\boldsymbol{F}$ in conformation space.

In the marine bacterium *V. alginolyticus* the buckling of the hook under compression is responsible for a 90° 'flick' of its flagellum. Therefore it may be possible, that the dynamics of the hook also play a role in the flagellar dynamics of *P. putida*. No wrapped cells swimming in the opposite direction with a CCW rotating flagellum were observed. During CW wrapped swimming the cell is effectively pulled by the flagella and so the hooks are under tension. In a reverse wrapped state the hook would be under compression, which suggests that such a state would be unstable.

It is also worth noting, that the wrap to push transition described here is similar to a scenario suggested in a previous study by Raatz et al. (2015). However, no significant curvature of the wrapped runs predicted in Theves, Taktikos, et al. (2013) was observed in this work. These curvature differences have proved difficult to measure from phase contrast tracking alone. One of the reasons for this is the relative lack of pulling runs close to the surface because of their hydrodynamic instability. Another might be the lack of any systematic curvature at all in the wrapped runs.

For future investigation it might be possible to use relationships between speed change and mean turning angle of transitions established in this work to design a classification algorithm for run states. It might then be possible to extract this state information from bright field data speed and direction information alone. This kind of algorithm could use a combined mixture model for the run speed and turning angle in order to extract the runs' states. In order to test or train such an algorithm, mixed bright field and fluorescence recordings will be necessary, such as the technique recently developed by Turner, Ping, et al. (2016). This will enable the collection of more and longer tracks as well as their combination with swimming state information.

Advantages of wrapped swimming

Kühn et al. (2017) showed that strong confinement and high viscosity of the medium can increase the proportion of wrapped swimmers. At the same time, both organisms

described in Kinosita et al. (2017) live in mucus rich habitats, which presumably also have areas with higher viscosity. It therefore seems that this newly discovered mode of bacterial swimming is strongly associated with viscous environments and must present an advantage over regular push or pull motility in these settings.

P. putida's natural habitat is the soil, were it is frequently found associated with plant roots. Because there are many different pore sizes from the mm to µm scale present in the soil, *P. putida* will encounter dead ends or get stuck when swimming freely. Whether the advantage conferred by this swimming mode is due to enhanced propulsive efficiency (Constantino, Jabbarzadeh, et al., 2016), or other interactions with the environment remains to be investigated in future work. Since the extended flagellum modes always cause a strong curvature of the swimming trajectories when in contact with surfaces, it might be possible that the presence of a non-curved mode of propagation benefits the chemotactic search for nutrients or signal molecules.
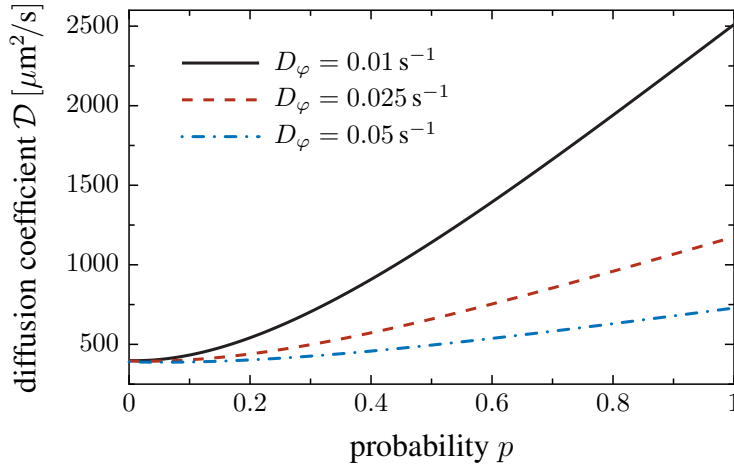
Figure 4.19.: Effective diffusion coefficient for *P. putida's* motility pattern. The probability p denotes the branching fraction – the probability that a pulling cell will switch to wrapped mode. The diffusion coefficient increases monotonically with an increasing branching fraction, i.e. more frequent pull-wrap transitions. Reproduced from Hintsche et al. (2017).

In Hintsche et al. (2017), we showed that the motility pattern described in this section increases the spreading of a population in the long time diffusion limit. The model, developed by Robert Großmann in that study, is based on some simplifying assumptions. All three states have the same mean run time τ, the speed in wrapped mode is half that of the other two modes, and the mean turning angles associated with the possible transitions are those given in table 4.2. The main free parameter is the branching fraction p which denotes the probability that a cell in pulling mode will switch to wrapped mode. Switching instead back to pulling mode then occurs with probability $(1 - p)$. From the master equations for the occupation probability of each

swimming state, Robert Großmann derived the long term diffusion coefficient:

$$\mathcal{D}(p) = \frac{v_0^2}{3(2+p)} \cdot \frac{16D_\varphi(2D_\varphi + k) + 4D_\varphi(D_\varphi + 3k)\,p + k^2p^2}{8D_\varphi\left[4D_\varphi^2 + 6D_\varphi k + k^2(2+p)\right]} \;,$$

where $k = 1/\tau$ is the transition rate and D_φ is the rotational diffusion coefficient of the cell during runs. The resulting dependence of $\mathcal{D}$ on p is shown in figure 4.19.

At $p = 0$ the model reduces to the case of a swimmer with exponentially distributed run times performing a run-and-reverse pattern (Taktikos et al., 2013; Theves, Taktikos, et al., 2013). For $p > 0$ however, it predicts an up to three fold enhanced diffusion coefficient for *P. putida* when using a rotational diffusion coefficient close to the experimental value ($D_\varphi = 0.025/\text{s}$) (Theves, Taktikos, et al., 2015). This result can be attributed to the 0° transitions from pulling to wrapped mode, which increases the distance traveled by preventing a 180° reversal which would decrease the total distance traveled (figure 4.19).

These calculations show that *P. putida's* three state motility pattern is advantageous for the spreading of a population of cells, when compared to a push-pull swimmer without wrapped mode.

4.2. Structured environments

In order to study motility in a more realistic environment we used microfluidic techniques and computerized tracking of bacteria to observe our model organism in structured environment of varying porosities. We introduced the cells into flat rectangular microchannels with cylindrical obstacles arranged on a hexagonal lattice (see section 3.5 and figure 3.3). Several different combinations of obstacle sizes and spacing were used.

Table 4.3.: Geometries used as structured environments.

parameter	length/µm
obstacle distance d	5, 10, 25
obstacle size D	25, 50, 75, 100

Of these parameters, all 12 combinations were studied.

The movement of cells was recorded using phase contrast microscopy and analyzed by cell tracking. We further extracted motility statistics and analyzed the movement and interaction of the swimming cells with their surroundings. Firstly, we describe general cases of obstacle interactions with and without direct labeling of flagella. Then, we quantify the difference between observed run lengths of bacteria with the geometrical mean free path lengths for particles with constant velocity in a dynamical billiards situation. Finally, we compare recorded cell tracks with a simple dynamical billiards model of motion in structured environments.

The experiments presented in this section were performed by Marco Bahrs, whose bachelors thesis I co-supervised (Bahrs, 2013). We then performed the data analysis of the cell tracks and interpreted the results together with Michael Raatz (Raatz et al., 2015).

4.2.1. Interaction with obstacles

Because of the high obstacle densities in these experiments, we saw frequent interactions of cells with the boundaries. These interactions can be grouped into three categories.

The first kind we observed was the "attachment" of trajectories to the obstacle surfaces. Here, bacteria swam very close to the obstacles for prolonged periods of time, after coming into contact with them, see figure 4.20, panel A. This kind of behavior is most likely due to the previously described wall effect (section 2.2.1), which tends to align pushers in parallel to solid boundaries (Berke et al., 2008; Lauga and Powers, 2009). Sometime, the cylinders were completely circled by cells before they detached from their surface.

Other times, collisions occurred where swimmers bumped into the obstacles and then sharply changed their direction of swimming. Often the bacteria stayed close to the obstacles after the collision, see figure 4.20B. Lastly, through a combination of

these two interactions, swimmers were seen to traverse long sections of the channels by swimming along multiple obstacles successively and thus being guided along their contours, see figure 4.20C.
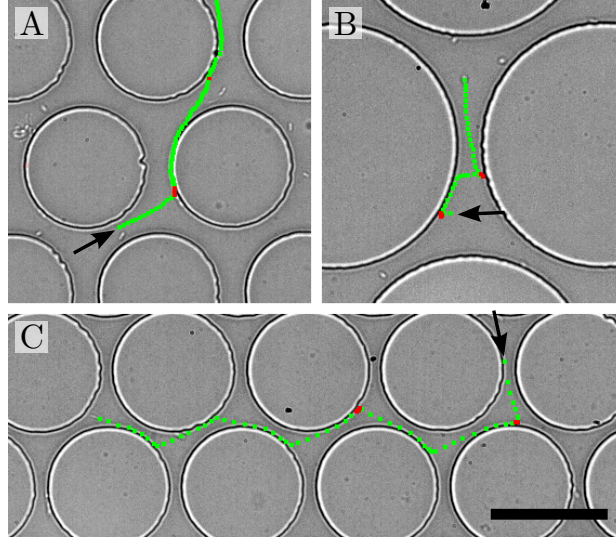
Figure 4.20.: Obstacles guide the runs of *P. putida*. Cell tracks are shown in green, turn events are red. All tracks start at the arrows in the direction indicated. (A) Some cells are guided along the obstacle walls through hydrodynamic effects. (B) Direct collisions sometimes induce turns. (C) Longer runs can be guided along multiple obstacles by bouncing between them. Scale bar is 50 µm. Reproduced from Raatz et al. (2015) with kind permission of The European Physical Journal (EPJ).

To further quantify these initial observations we applied the established turning classification algorithm of Masson et al. (2012) to our trajectory data. Since this algorithm is based on speed and turn rates of the swimmers, it can not distinguish turns initiated by motor rotation (section 4.1) from those brought about by mechanical interaction with obstacle surfaces. Thus we will refer to both types of events as 'turns' below.

We calculated motility parameters such as turning angle and run time distributions for all of the 12 channel geometries used. However, no significant differences or trends between the different channel configurations could be detected. All turning angle distributions showed clear peaks at 0° and 180°, which correspond to combinations of the reversal and flip-over transitions observed in section 4.1, as well as stop events previously described (Theves, Taktikos, et al., 2013).

The turning angle distribution averaged over all geometries is depicted in figure 4.21a, without including turns very close to obstacles. This false-positive background could not be improved by optimizing the parameters of the turn classification. Probably, it is due to a combination of interactions with the channel boundaries and highly curved
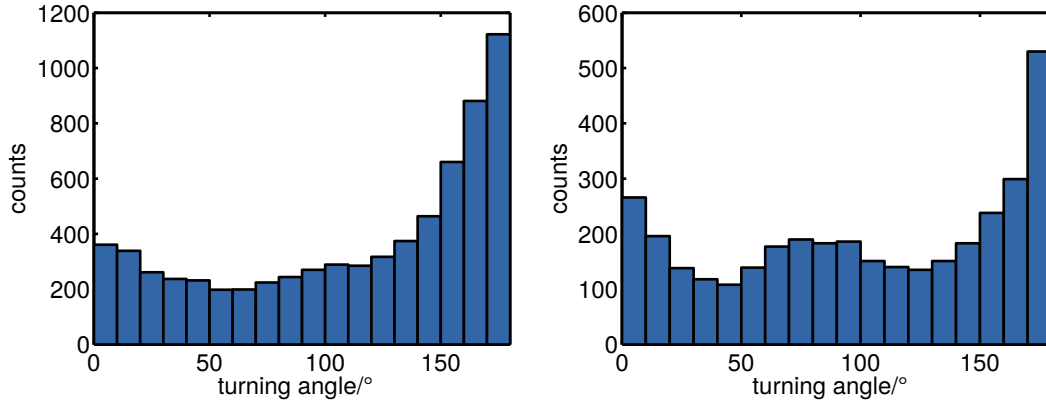
(a) turns *further* than 2 µm from any obstacles   (b) turns *closer* than 2 µm to any obstacle

Figure 4.21.: Turning angle distribution of cells in a structured environment. Histograms are averaged over all geometries. (a) When not in contact with an obstacle, cells show normal turning events at (0° and 180°) as well as a background due to non ideal turn classification. (b) Swimmers in contact with an obstacle show additional surface scattering as shown by the peak at ≈ 90°.

sections of the swimming runs. Since the microchannels used here are only 5 µm high, cells will most of the time be very close to either the top or the bottom surface of the channel. For cells in either pushing of pulling mode this may causes highly curved runs (subsection 4.1.1). Because runs with a wrapped flagellum alternate with those with an extended flagellum, the curvature of runs may change abruptly between swimming states. Additionally cells can quickly come into, or leave, contact with the surfaces in z-direction, which also causes run curvature to change magnitude and sign very fast.

Therefore, the standard turn classification scheme could not be perfectly tuned to the conditions in our structured channels. Because our turn classification algorithm was devised for bacteria swimming in the bulk fluid, it cannot distinguish the frequent changes in direction induced by obstacle contact from freely performed turns and stop events. This leads to a background of falsely identified turns, which can be seen in figure 4.21 as a constant offset over the whole angle range. Measurements performed in the bulk fluid in this work (compare figure 4.31 and figure 4.37) or in previous studies (Theves, Taktikos, et al., 2013) do not show this broad background in the turning angle distribution. We therefore believe, that the measured turning angles measured in our structured environments have a higher false-positive classification rate. This means that slightly more turns are classified as such than in a bulk situation.

We also measured how motility parameters vary with the distance from the obstacles surfaces. Figure 4.21 shows the turning angle distributions close to, and far away from the actual obstacles in the channel. In both cases the previously observed peaks at 0° and 180° are present. However, in proximity to the cylindrical obstacles turns with angles around 90° tend to occur more often. We attribute this observation to
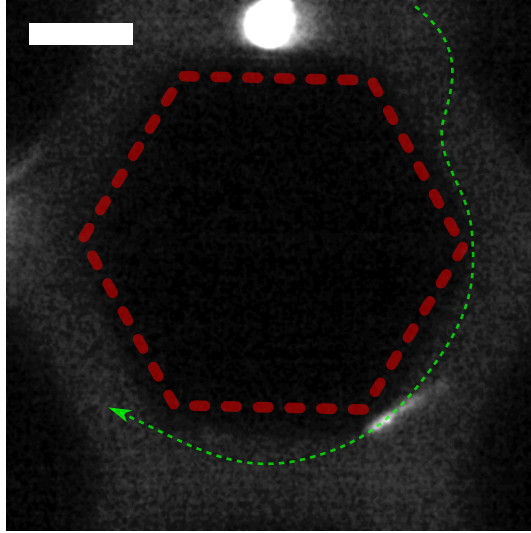
Figure 4.22.: Cell swimming around a hexagonal obstacle. The stained flagella are trailing behind the cell body throughout the event, and the cell is always at an oblique angle to the obstacle surface. A montage of the time course of this event is shown in figure A.3. Scale bar is 10 µm.

interactions of the swimming cells with the obstacle surfaces. Directional changes induced by obstacles occur over a wide angle range and are distributed broadly around 90°. Because we did not directly visualize flagella in these experiments, we can not distinguish between passive reorientations from surface interactions and active, flagella driven, reorientation events like reversals or flip-overs.

To further investigate these observations in Raatz et al. (2015), we fluorescently labeled cells swimming in very similar structured channels, using the protocol established in the previous section. In order to try and distinguish active from passive interactions, we were able to image a few bacteria with stained flagella swimming close to hexagonally and quadratically shaped obstacles.

An example of a cell swimming around an obstacle is shown in figure 4.22. Here the cell is moving as a pusher with the flagella behind the cell body. Throughout the event, the flagella and body are at an angle to the direction of motion (shown by ⌐--➤). The thrust axis is angled towards the obstacle in the middle and leads to the guiding of the cell along the obstacle wall.

It is well known, that swimming as a pusher leads to a moment that aligns the cell parallel to a surface (Berke et al., 2008; Lauga and Powers, 2009). The situation presented here is, however, more complex. At the top of figure 4.22, the cell can be seen changing from one obstacle surface to another. Because the channels used are very shallow (5 µm), the cell is in close proximity to at least three walls at the same time: top and bottom of the channel, as well as the side of the obstacle. This is presumably the reason why small perturbations can lead to an "attachment" to a different surface – each of which is a locally stable hydrodynamic equilibrium were the cell is very close

to that surface. Cells also would often switch from swimming in focus (close to the cover slip) to out of focus (close to the PDMS bottom of the chip).

We thus have gathered evidence that pushing swimmers can be guided through complex geometries due to passive interaction with the walls. The effect responsible for this is presumably a well known alignment effect due to to dipolar nature of the swimmers' flow fields (see section 2.2.1 and (Berke et al., 2008; Lauga and Powers, 2009)). Additionally we could directly observe the off-axis thrust line generated by the swimmers' interaction with the wall, which might be used in the future for quantitative measurements of hydrodynamic forces in this system.

In contrast, no pulling and only a brief wrapped episode could be observed. This might again be due to the unstable nature of pulling swimmers in proximity to surface. Since only a few of these recordings were made, these observations should be considered only as initial evidence, which have to be studied in greater detail. Nonetheless, to our knowledge, these are the first observations which directly show the interaction of flagellated swimmers with surrounding surfaces.

4.2.2. Mean free path length

To better understand the influence of obstacle collisions and interactions on the overall motility in these channels, we will now compare the measured motility statistics to a geometrical prediction for particle movement in complex geometries.

A first approximation for movement in these environments is that of dynamical billiards. Here particles move only on straight lines with a constant velocity. Their direction only changes due to elastic collisions with the boundaries. Because the theory for this kind of motion is well known, we were able to compare the dynamical billiards model with our measured motility statistics. Santaló (1976) calculated the mean free path (MFP) for this kind of molecular billiards in the context of integral geometry. In the limit of many reflections it does not depend on the actual geometry of the volume, but only on the mean free volume $|Q|$ and its surface $|\partial Q|$. Because of the narrow channel height, bacteria can effectively only move in two dimensions. There Santaló's formula gives

$$\langle \tau \rangle = \frac{\pi |Q|}{|\partial Q|} \ ,$$

where τ is the free path length, $|Q|$ is the void area and $|\partial Q|$ the boundary circumference (Santaló, 1976).

We estimated the mean run length of the bacteria for each geometry by multiplying the measured mean run times by the mean speed.

$$\langle l_{\mathrm{run}} \rangle = \langle v_{\mathrm{run}} \rangle \times \langle t_{\mathrm{run}} \rangle$$

These run lengths $\langle l_{\mathrm{run}} \rangle$ are plotted in figure 4.23 as a function of the MFP $\langle \tau \rangle$ of a billiard particle for all geometries used.

We find that, at the smallest obstacle distance of $5 \, \mu\mathrm{m}$, the measured run length is similar, or even slightly larger then the MFP. This indicates that runs are mostly
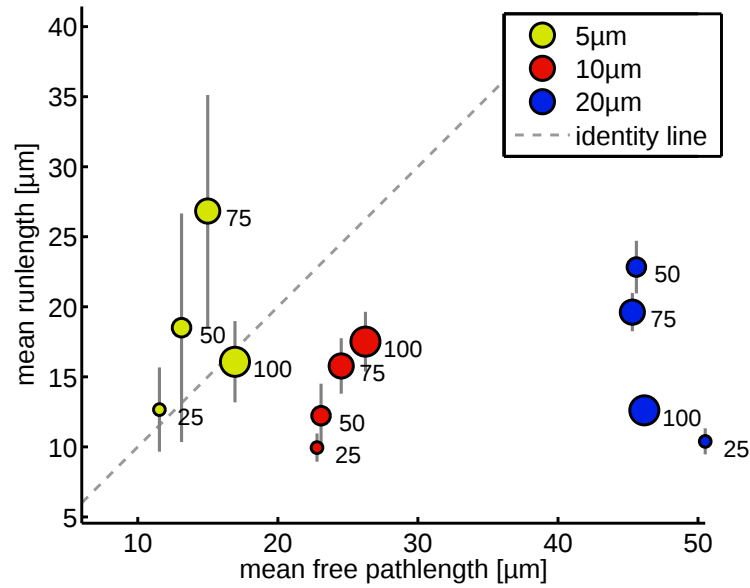
Figure 4.23.: Measured mean run lengths versus the predicted mean free path lengths of an equivalent dynamical billiards. Bubble sizes correspond to the size of obstacles, gray bars indicate standard error of the mean. The dotted line indicates the identity $\langle l_{\mathrm{run}} \rangle = \langle \tau \rangle$. Points below the line have shorter runs then predicted by the geometry alone, while points above it have longer runs on average. Reproduced from Raatz et al. (2015) with kind permission of The European Physical Journal (EPJ).

limited by frequent collisions with obstacles. For some obstacle sizes though, runs are even longer than the MFP, which shows that swimmers are indeed guided by the obstacle surfaces. As the obstacle size increases, runs do not get significantly longer, despite an increasing MFP. The intrinsic run time scale in swimming bacteria is the mean run time of about one second. It limits the average run lengths to about 15 µm to 20 µm under the conditions in these experiments. Only a weak dependence of run lengths on the obstacle sizes could be observed. In the 5 µm and 20 µm distance cases, the intermediate sizes of 50 µm and 75 µm increase the run length slightly. Most likely this is again an effect of guidance of swimmers by the obstacle walls, which might be more prominent at certain curvatures of the boundaries.

4.2.3. Discussion

From the manual examination of phase contrast and fluorescent trajectories it is clear that many tracks are guided by the nearby surfaces of obstacles, as well as the channel top and bottom. As we showed by comparing the situation to a dynamical billiards, this leads to an extended traversal of the environment.

The billiards situation, in which each contact to an obstacle leads to an elastic collision, is clearly not sufficient to explain the behavior of swimming *P. putida*. In-silico studies of active swimmers without hydrodynamic interaction with the obstacles, yielded very different dynamics (Zeitz et al., 2017). In this study, active Brownian particles swim in a 2D random maze of disk shaped obstacles. They frequently get stuck in corners – a behavior which we never saw in our microscopic observations. This evidence, together with our microscopic observations lets us conclude that hydrodynamic interactions dominate the guiding behavior in these narrow confinement situations.

One problem with bright field and phase contrast observations of cells swimming in structured channels is that a heuristic turn classification will never be able to distinguish completely and accurately between a change in direction due to active flagellar dynamics or one due to purely passive obstacle interaction. This problem might be alleviated by gathering larger data sets with fluorescently stained flagella. Here, active turns due to flagellar dynamics could be correctly distinguished.

In the above analysis we also did not consider the wrapped swimming mode, because at the time of this study the new swimming mode was not known to us. However, fluorescence observations would also help to distinguish swimming modes. This could improve our understanding of wrapped swimming in the context of surface interactions and confined spaces, as that environment would be much closer to *P. putida's* native habitat. It would be conceivable that a peritrichous swimmer that can only push, would be attracted to surfaces all the time, except during its short tumblings. A swimmer with push, pull and wrapped mode in contrast, would have more opportunities to detach from surfaces, since pulling actively drives cells away from them and wrapped mode is, as far as we know, indifferent towards them.

4.3. Chemotaxis

To investigate the chemotactic strategy of *P. putida*, we used a microfluidic device to generate linear gradients of a chemoattractant and recorded bacteria swimming in them using phase contrast microscopy. As an attractant we chose sodium benzoate, because it has been shown to elicit chemotaxis in *P. putida* and few is known about bacterial chemotaxis towards aromatic compounds.

The experiments were performed in a microfluidic device, composed of two reservoirs connected by an observation chamber (section 3.3). We uses gradients of varying strengths, as listed in table 4.4. In each gradient, we extracted several hundred cell trajectories from video recordings and measured the responses of the *P. putida* cell populations to the gradients. To this end we computed key motility parameters such as run time, run speed, and turning angle and analyzed them for possible chemotactic biases. We then discuss the chemotaxis strategy of our model organism and compare it with that of *E. coli*.

Table 4.4.: Parameters of the gradient experiments. c_{left}/mM and c_{right}/mM are the concentrations in the left and right reservoir of the gradient chamber, while ∇c/(mM/mm) is the resulting gradient strength.

c_{left}/mM	c_{right}/mM	∇c/(mM/mm)	no. of tracks	no. of runs
0	0	0	68	208
0.0	0.5	0.5	231	646
0.5	5.0	4.5	885	2673
0.0	5.0	5.0	170	454
5	5	0	128	250
0	50	50	809	1963

P. putida and other *Pseudomonads* are known to stop their runs by completely halting their motors (Theves, Taktikos, et al., 2013; Qian et al., 2013; Cai et al., 2016). Under the conditions used to induce chemotaxis towards benzoate *P. putida* performs stops with a rate below 0.25/s, see Influence of growth conditions. Since stops are present only in a fraction of the recorded trajectories, which are on average 1–2 seconds long, they were not included in our analyses of gradient response.

Under different conditions, however, stops do occur more frequently. In subsection 4.3.4, we show conditions that lead to an increase of the stop rate, and discuss how this might influence the modeling and description of *P. putida's* motility. Lastly, we discuss if stops impact the chemotactic behavior of our model organism.

4.3.1. General motility pattern

In this subsection we summarize the general motility pattern of cells swimming in different gradient conditions. We then introduce a classification scheme for run modes based on the available trajectory information.

mode	$\langle v \rangle$ / µm/s	σ_v/ µm/s	w
slow	19.9	7.2	0.64
fast	39.0	5.1	0.36

(a) no gradient

mode	$\langle v \rangle$ / µm/s	σ_v/ µm/s	w
slow	16.6	5.8	0.62
fast	38.3	7.0	0.38

(b) gradient strength 0.5 mM/mm
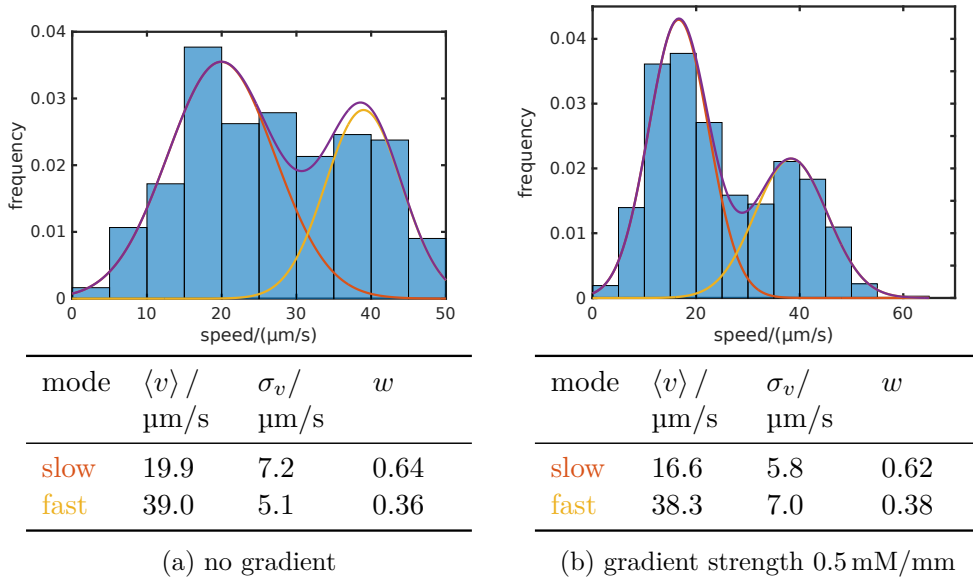
Figure 4.24.: Run speed distribution in different gradients. The solid curves are in-
ferred from a Gaussian mixture model (GMM) which is shown in purple.
The two components of the model are shown in orange and yellow.

As we showed in section 4.1, *P. putida* exhibits three distinct modes of swimming.
Without being able to visualize the flagella, we could not directly observe which swim-
ming mode (push, pull, or wrapped) the runs were in. However, the two distinct
speeds associated with extended and wrapped flagellar modes are clearly visible in
most datasets presented here. Two example distributions are shown in figure 4.24. In
these histograms of individual run speeds, two distinct peaks are present, one from
each flagellar mode. The broadness of the peaks is presumably due to a heterogeneous
distribution of swimming speeds within the bacterial population. The cells are in
different states of growth, sizes of their cell bodies and, correspondingly, lengths and
number of their flagella.

It is therefore not easily discernible if a given run is from the fast (extended flagella)
or slow (wrapped flagella) mode of swimming. A rigorous way of classifying run speeds
into a slow and a fast class is provided by a Gaussian Mixture Model (GMM). The
underlying assumption is that the data can be represented by a sum of two independent
normally distributed variables. It can be fitted to the data using a maximum likelihood
based algorithm, for details see section 3.8.2. The solid purple curves in figure 4.24
show the fit of the GMM and the tables below the figures the inferred parameters.
Most importantly, the prior probability that a run was in a designated mode is given
by the mode weight $p_{\text{fast}} = w_{\text{fast}}$ and $p_{\text{slow}} = w_{\text{slow}} = 1 - w_{\text{fast}}$. For the cells in
the 0.5 mM/mm gradient (figure 4.24b) the probabilities are 62 % and 38 %, for fast
and slow mode, respectively. This observation matches the three state description

obtained from the direct flagellar observations, where two out of three states are fast (push/pull), and one is slow (wrap). Additionally the figure shows that although the exact speeds and prior probabilities change with the gradient strength, both modes occur with and without the presence of a chemoattractant gradient. These results are in line with previous observations from Theves, Taktikos, et al. (2013) and Theves, Taktikos, et al. (2015) where the cause of the two speeds was not yet known and cells were cultured in slightly different conditions.

We therefore conclude, that the swimming behavior observed in the section Flagellar dynamics is also present in cells grown under slightly different conditions and without the stressors of the chemical staining protocol.

4.3.2. Chemotactic index

In order to quantify the chemotactic behavior of motile cells, the chemotactic index (CI) is frequently used to measure chemotactic efficiency. It is defined as the ratio of displacement traveled in the gradient direction d_x to the total path length l traversed:

$$\mathrm{CI} = \frac{d_x}{l} \ .$$

Here, we will use it to confirm that *P. putida* does indeed perform chemotaxis in our experiments and how its chemotactic efficiency relates to the gradient strengths it is exposed to.

With the microscopic wide field tracking technique we used, only rather short trajectories could be observed, usually between one and two runs long. As a consequence, the chemotactic index of individual trajectories fluctuates wildly. Therefore, we concatenated all trajectories from one experiment together by starting each new trajectory where the following left of. The resulting 'great trajectory' time traces are depicted in figure 4.25, which shows the population averaged chemotactic performance. Calculating the average CI from this great trajectory is equivalent to weighing each CI by its traversed path length: $\langle \mathrm{CI} \rangle_w = \langle \mathrm{CI}_i \cdot l_i \rangle / \sum_i l_i$, see subsection 3.8.3. The unweighted CI differs by up to one order of magnitude from the weighted one. For example, in the dataset shown in figure 4.25, the non weighted CI in parallel direction is 0.0079 compared to 0.018 for the weighted one. Because the magnitude of the CI is quite low, the values we computed have a considerable spread. This made the use of the weighed values necessary, even in strong gradients like the one shown.

The calculation was repeated for all the different gradients strengths and the resulting CIs are shown in figure 4.26. At high gradient strength ($|\nabla c| \gtrsim 1\,\mathrm{mM/mm}$) the cell populations clearly exhibit chemotactic behavior. The measured CIs correspond to drift velocities of $\approx 5\,\%$ to $10\,\%$ of the average cell velocity. At lower gradient strengths however, the measured CIs are more scattered and even negative. One reason for the negative drift observed might be residual advective flow in the microfluidic chamber. Slightly different cell concentrations in the two reservoir chambers of the microfluidic chip also can cause a non-chemotactic drift just by non-directed diffusion of the actively swimming cells. The magnitude of this effect is quite small. For example, the effective drift speed of the population at $0.5\,\mathrm{mM/mm}$ was $0.45\,\mathrm{\mu m/s}$ or

(a) parallel to gradient direction,
$\langle\mathrm{CI}\rangle_w = 0.058$

(b) orthogonal to gradient,
$\langle\mathrm{CI}\rangle_w = 0.018$
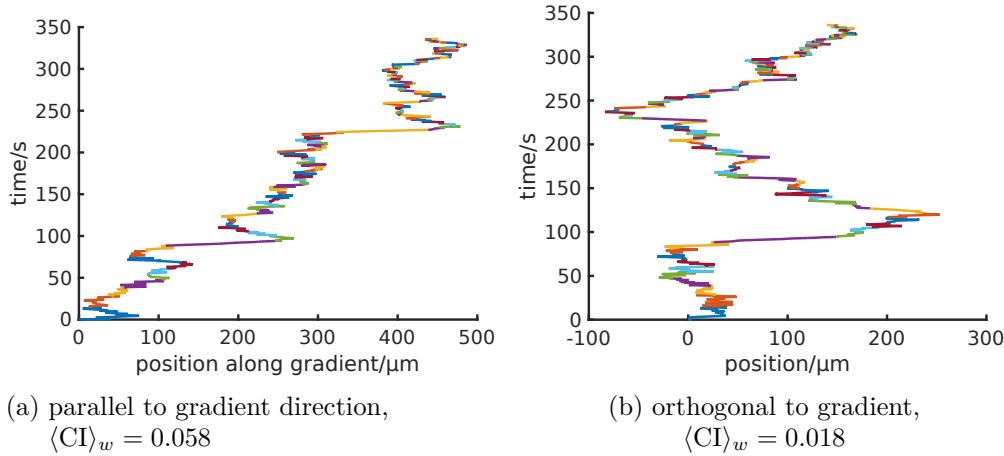
Figure 4.25.: Cumulative motion of bacteria in a gradient. Time traces of the concatenated "great trajectory" projected parallel and orthogonal to the gradient direction. The gradient points to the right, $\nabla c = 5.0\,\mathrm{mM/mm}$.

27 µm/min, less than 2 % of the swimming speed of cells. That is why this drift was not visible at the time of measurement as well as on the level of individual trajectories. Unfortunately, it was not possible for me to correct this in retrospect.

All measurements of this data set where recorded under identical conditions on the same day. Because of this, we conclude that all of the channels were subject to the same drift. The upwards trend of the measured drift is therefore independent of the offset caused by non ideal experimental conditions.

The trend indicates a systematic chemotactic effect that increases with rising gradient strengths. At low gradient strength the CIs do not conclusively show if the cell populations do indeed perform chemotaxis and how strong this effect might be compared to the higher concentrations. Especially at $\nabla c = 0$ the uncertainty is too large to give definitive conclusions. The large uncertainty is mostly due to the low number of tracks recorded in these chambers.

In the strong gradients, however, the measured CIs are similar to results for other bacteria such as *E. coli* which are on the order of 10 %.

4.3.3. Strategy

In the following section we describe what kind of chemotaxis strategies might occur in a swimming bacterium and show which of those strategies are actually applied by *P. putida*.

To achieve chemotaxis an organism might modulate any one or many of its motility characteristics. For bacteria several methods are usually considered. Firstly, a run time bias might be present: runs up the gradient are longer on average. This has been observed in many bacteria and is the main method of bacterial chemotaxis. Secondly a run speed bias might cause runs up the gradient to be faster on average – this is
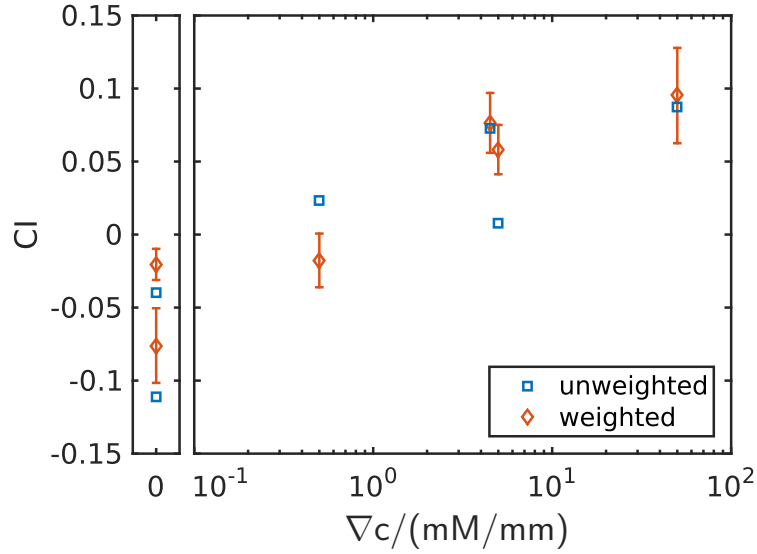
Figure 4.26.: Chemotactic index in gradients of different strengths. Gradient values are $0, 0.5, 4.5, 5.0$ and $50\,\mathrm{mM/mm}$ (see also table 4.4). Error bars represent standard error of the mean. Uncertainties for the unweighted CIs are outside the plot range.

termed chemokinesis and has been in observed in *S. meliotis* (Sourjik and Schmitt, 1996). Lastly a strategy might exist, which biases the turning angles from one run to the next, such that runs are more likely to point up the gradient. This effect has been proposed and been measured under certain conditions in *E. coli* (Saragosti et al., 2011). All three of these chemotaxis strategies are investigated below.

Run time bias

E. coli chemotaxes by increasing the length of runs that lead it up the gradient (H. C. Berg and Brown, 1972), but runs down the gradient are not increased in length. Since it always swims with a pushing flagellar bundle, it can only perform one kind of run and all runs have approximately the same speed. *P. putida* however can exhibit different types of runs under the conditions studied here.

As we showed in section 4.1, it can swim in pushing and pulling mode, with an extended flagellum, as well as with the flagellum wrapped around the cell body. The relative probability of swimming in one of the three run modes might be modulated by the concentration signal measured by its chemoreception machinery. This in turn means that an *E. coli* like strategy of run time modulation is not strictly necessary for *P. putida* in order to perform chemotaxis.

We measured the run times of *P. putida* and determined the run time distributions – shown in figure 4.27. It shows the complementary cumulative distribution function (CCDF) of runs times, conditioned on the run direction. All runs that have a com-

(a) 0.5 mM/mm

(b) 5.0 mM/mm
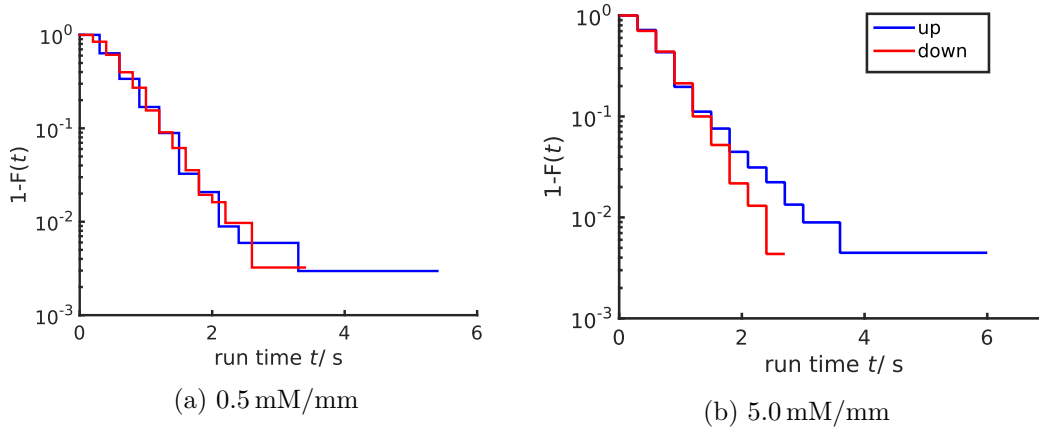
Figure 4.27.: Run time bias in benzoate gradients. CCDF of run times conditioned on the run direction relative to the gradient.

ponent pointing up the gradient are grouped together, as are those with a component pointing down the gradient. The CCDF is the probability P of observing a run time greater then t: $\text{CCDF}(t) = P(T > t) = 1 - \text{CDF}(t)$. It is the complement of the well known cumulative distribution function (CDF).

In strong gradients, such as in figure 4.27b, we found that very long runs, more than about two seconds, occur more frequently if going up the gradient than if going down. This means that *P. putida* employs the same strategy as *E. coli*, it lengthens runs that go in a favorable direction.

In shallower gradients there seems to be no appreciable difference in run lengths in either direction. If there is a chemotactic drift at lower gradient strengths, it is masked by the residual experimental drift. Above 0.5 mM/mm the chemotactic drift becomes measurable in the form of run time bias. This might indicate, that this is the gradient strength where experimental and chemotactic drift just cancel each other out. figure 4.26 also supports this conclusion as the CI at 0.5 mM/mm is almost equal to 0 within its uncertainty.

An overview of the run time distributions in all different gradients measured is given in figure 4.28a, where we show the average run time against the gradient strength. In shallow gradients, runs up the gradient tend to be shorter, which is probably again caused by residual flow effects. In steeper gradients, there is a clear increase in the overall length of runs, as well as an increasing difference between run directions. This coincides with the increase in chemotactic efficiency noted before and confirms that *P. putida* exhibits a run time bias, and lengthens its runs up the gradient.

A change in run times that is not triggered by the gradient itself, but by the background concentration indicates a non adapted chemotactic response. This is supported by our results from subsection 4.3.4, where we calculated the average run times for *P. putida* swimming in several different solutions of homogeneous benzoate concentrations. They start at 0.6 s in $c = 0$ mM and increase to 1 s in $c = 10$ mM. We therefore

73
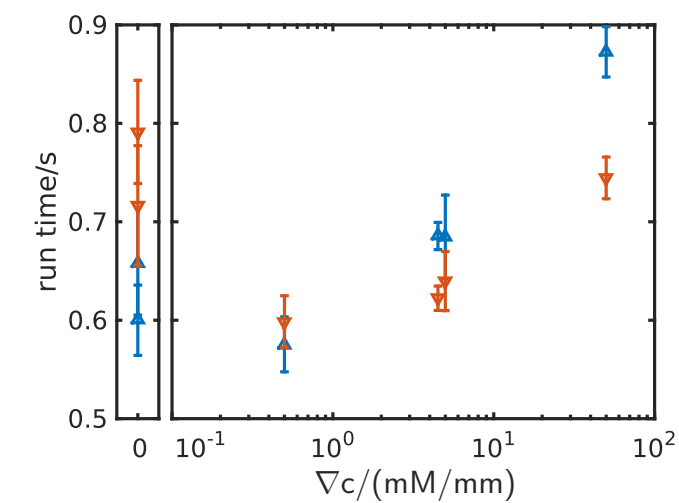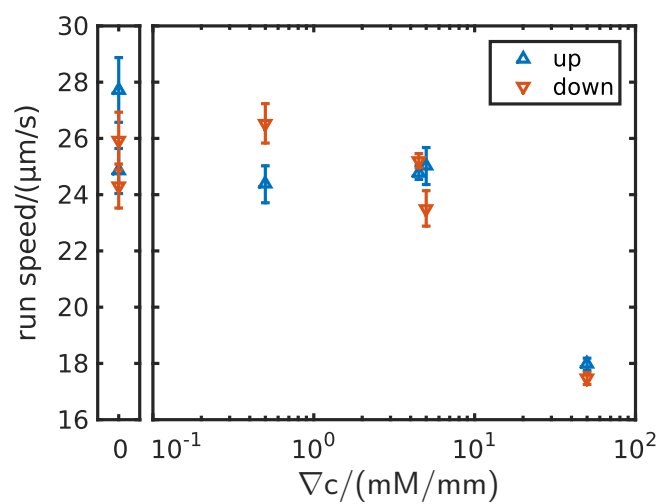
(a) run time

(b) run speed

Figure 4.28.: Average run time & speed in different benzoate gradients. Measurements are grouped separately by their direction relative to the gradient: △ for up, and ▽ for down the gradient. At high concentrations the run time is larger for runs going up the gradient then down the gradient. Error bars indicate standard error of the mean. At small concentrations however, the effect is less pronounced.

conclude that *P. putida* is indeed not completely adapted to benzoate.

Measured run times decrease around the $0.5\,\text{mM/mm}$ gradient. Because the measurements at $\nabla c = 0$ have a large uncertainty it is no completely clear if there truly is a minimum in the run time at low concentrations. Steady state measurements in Waljor (2016) show lower run times at $c = 0$, which indicates that our results shown in figure 4.28a are artificially increased by the residual flow. Nonetheless, as the concentration of benzoate increases further, *P. putida's* runs lengthen again, becoming even longer than without any chemoattractant.

Run speed bias

P. putida could also achieve positive chemotaxis by biasing runs up the gradient to be faster then runs downwards.

We checked for this effect by conditioning the measured run speeds on the direction relative to the gradient. The resulting mean run speeds for all gradient strengths are shown in figure 4.28b. Most significant is a decrease of the average run speed, regardless of direction. Presumably this is due to an inhibition of the motility machinery in high benzoate concentrations, which will be discussed later.

Superimposed on this general trend is an additional modulation of speeds depending on the run direction. At zero gradient, runs up the gradient are faster on average than runs downwards. For the low gradient strength ($0.5\,\text{mM/mm}$) runs upwards are slower, while at higher gradient strengths this effect is reversed and runs up the gradient are faster. The separation between the two directions decreases somewhat with the gradient strength, from about $7\,\%$ to $3\,\%$.

Any bias at $\nabla c = 0$ must be caused by drift effects like flow or passive diffusion, as discussed in the previous subsections. Because of this, as well as the large error bars for the no gradient situation, the difference in run speeds up and down the gradient may not be significant. At $\nabla c = 0.5\,\text{mM/mm}$ the difference is probably due to the residual flow in the microfluidic channel.

In conclusion, we cannot confirm a significant speed bias in *P. putida* swimming in benzoate gradients. The standard error of the mean shown in the previous figures probably underestimates the true measurement error, which is influenced by the microfluidic flow conditions. If a small bias is present, such an effect could be detected in similar tracking experiments with significantly lower residual flow. Alternatively, tracking of cells with significantly longer trajectories might also give further insights into the role of *P. putida* swimming speed in chemotactic situations.

Swimming mode bias

In order to examine the influence of the gradients on the fast and slow swimming modes we applied the Gaussian Mixture Model for the run speeds described previously (section 3.8.2) to runs going up the gradient separately from those going down. This way we could measure the speeds of the slow and fast modes, as well as their relative frequencies. Figure 4.29a shows the mean speed of modes and figure 4.29b the weight

(a) mean mode speeds

(b) mode weights
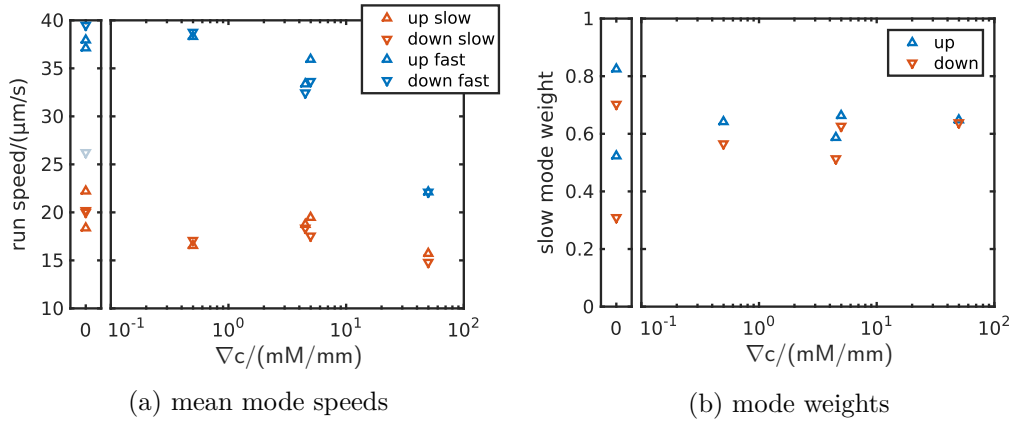
Figure 4.29.: Swimming modes in different benzoate gradients. For each gradient we applied the two component GMM to classify slow and fast runs. The runs were further grouped into up ($\triangle$) or down (∇) direction relative to the gradient. The grayed out point ($\triangledown$), at zero gradient, is considered an outlier due to the low number of samples at zero gradient.

of the slow mode in different gradients. The weight of the fast mode is the complement of the slow mode ($w_{\text{fast}} = 1 - w_{\text{slow}}$) because these are the only two possible outcomes and $p_{\text{fast}} + p_{\text{slow}} = 1$.

When comparing the mean speeds within each gradient condition and each mode, it is clear that the speeds differ only by a few percent. The dataset at $\nabla c = 0$ has a very low fast mode speed and should be considered an outlier (grayed out, $\triangledown$). In that measurement the fewest number of runs was observed and its statistical significance is smallest. The other points fall closely together for fast and slow modes. We believe the differences in speed between up and down directions to be within the measurement uncertainty. Because of this, we conclude that the swimming modes speeds are *not* modulated by the chemotaxis machinery under these conditions.

The mean speed of the slow mode is almost constant throughout all gradient conditions. It seems to be affected only weakly by strong gradients and high benzoate concentrations. The fast mode speed, on the other hand, decreases markedly in high benzoate concentrations – by up to 40 %. One possible cause of this effect is an impairment of the motility system by benzoate, such that the maximal attainable motor speed above $\approx 1\,\text{mM}$ is reduced. If both modes were affected proportionally by increasing benzoate concentrations, both speed would decrease with increasing concentration. However, as shown in figure 4.28a, the average run times also increase by up to 25 % at high benzoate concentration. This is an indication that both fast mode speed, as well as run time are modulated by chemosensory response. Otherwise only the speed would go down, but the run times would stay the same.

Another possible chemotaxis mechanism could be created by decreasing the number of slow runs going up the gradient or increasing the number of slow runs going down.

Figure 4.29b shows the weight of the slow mode for runs conditioned on the gradient direction. The weight of a mode in the mixture model is the proportion of runs that are attributed to that mode. Therefore w_{slow} corresponds to the percentage of slow runs and w_{fast} to the percentage of fast runs, if the model assumptions hold. Already at $\nabla c = 0\,\text{mM/mm}$ a significantly larger proportion of slow runs is going up the gradient than down. With increasing gradient strength the difference between up and down proportions diminishes slightly. Positive chemotaxis, however, could only be produced by the opposite bias, were slow runs down the gradient are more probable. In addition, the chemotactic index actually increases with gradient strength as shown in figure 4.26. All of this suggests, that the effective spread of up and down weights is solely due to the residual drift present in the microfluidic channels. It is thus unlikely that *P. putida* actively modulates the probabilities of its swimming modes in the presence of a chemoattractant.

Turning angle bias

Yet another possible chemotaxis mechanism could be devised by modulating the turning angles to increases the probability of runs which have a velocity component up the gradient. Based on the concentration history from the prior trajectory, the cell changes the probability for advantageous turning angles. For *P. putida* this means it would preferably have to turn into the gradient direction on its reversal, or, if the previous run was already pointing up the gradient, have a higher probability for a 0° 'turn' (i.e. a pull-to-wrap transition). Similarly, a stop would be better than a reversal in that situation. This situation is displayed in figure 4.30.
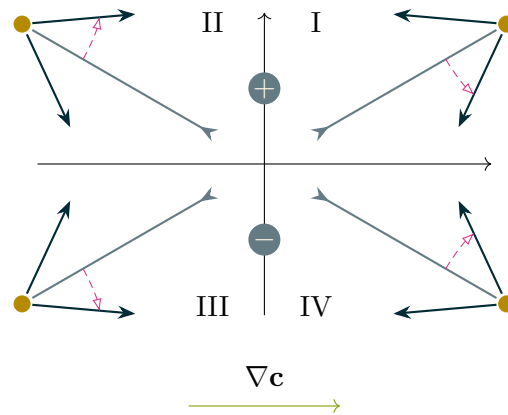
Figure 4.30.: Turning angle bias. In each of the four quadrants a prior (➤—) , and two possible subsequent runs (→) are shown. The turn after the prior run is marked by ●. For each of the two possible subsequent runs, the one leading up the gradient is marked by ---△. Roman numerals indicate the quadrant into which the prior run is pointing. The directions indicated by ⊕ and ⊖ are used to group the top and bottom quadrants together.

To investigate any possible angle modulation, we measured the signed turning angle of runs, conditioned on the prior direction. Runs going *left* and *right*, when looking up the gradient, are symmetric with respect to their advantageous turning angle. Here, we will refer two these directions orthogonal to the gradient as $+$ and $-$. If swimming into quadrant I, a turn to the right ($\triangleleft\text{-}\text{-}\triangle$) has a higher component up the gradient. The same is true if swimming into quadrant II: a turn to the right is advantageous. These two quadrants are therefore grouped in the $+$ direction, while quadrants III and IV, were a turn to the left is advantageous, are grouped in the $-$ direction.

The resulting histograms for each direction are shown in figure 4.31. Both distribu-
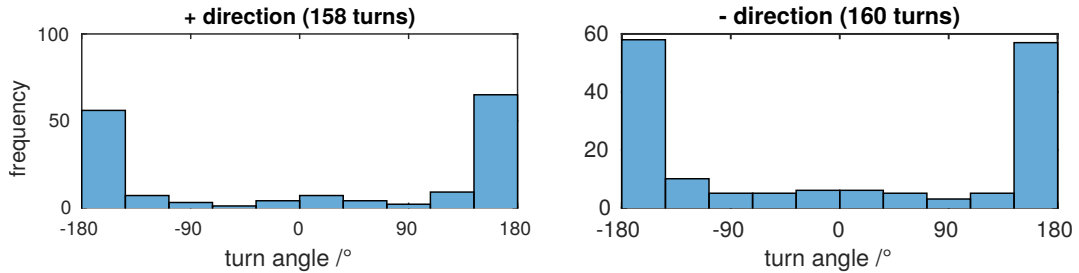
Figure 4.31.: Turning angle distribution, conditioned on the prior run direction. $+$ and $-$ directions group quadrant with symmetrical advantageous runs. Gradient strength is $5\,\text{mM/mm}$.

tions are symmetric with respect to the forward direction and we find no significant difference between the two cases. A positive turning angle modulation however, would require more *right* turns in the $+$ group, and more *left* turns in the $-$ group. Because of the symmetry in the distribution we can conclude that no angle bias is present in *P. putida* chemotaxis towards benzoate.

This is also the consensus for other bacterial swimmers, and agrees with our results obtained with the improved run and turn classification described in section 4.4.

4.3.4. Influence of growth conditions

In the previous sections, we only considered cells that were grown in a minimal medium with benzoate as the only carbon source, in order to induce the chemotaxis towards benzoate. In this section however, we will show that the motility pattern of *P. putida* strongly depends on the growth conditions that cells were subjected to. We will then discuss the adaptation of *P. putida* to the two chemoattractants benzoate and casamino acids.

In her bachelors thesis, which I co-supervised, Veronika Waljor measured the frequency of stops and reversals for cells grown in two different media, using the MATLAB analysis pipeline developed in this thesis (Waljor, 2016). Swimming was analyzed in rich medium (LB), as well as in a minimal medium (M9) under different chemoattractant concentrations.

In this series of experiments swimming cells would often stop in their runs These stops were marked manually in the recorded trajectories and used to compute several different motility parameters. Compared to *E. coli*, additional parameters have to be characterized, because we now have to consider more than two states of motion a cell can be in. This analysis, however, was performed before the three run modes push, pull, and wrapped, were known to us (section 4.1). Therefore, only one type of run and one type of turn were considered for this analysis. A side-by-side comparison of the traditional *E. coli* based two state model (H. C. Berg, 1975; Block et al., 1982) and the three state model necessary for this analysis is shown in figure 4.32.

(a) three state model
(*P. putida*)

(b) two state model
(*E. coli*)
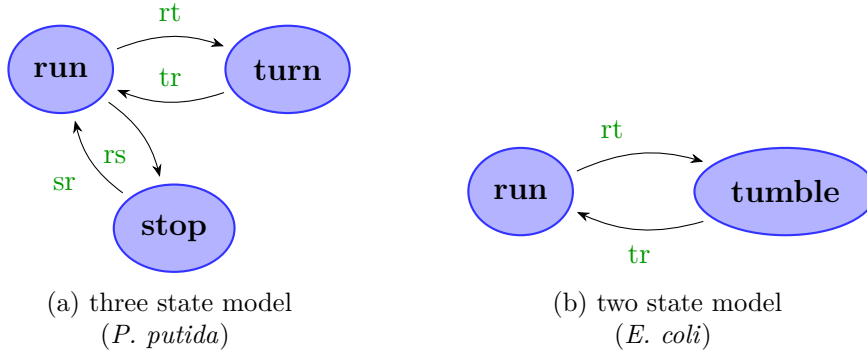
Figure 4.32.: State models for different swimming patterns

In the canonical *E. coli* model there is one run state and one tumble state, each with a life time and an associated transition rate. The tumble time is on the order of $0.1\,\mathrm{s}$, while the run time is on the order of $1\,\mathrm{s}$ (H. C. Berg, 1993). Furthermore, the tumble time does not change significantly in a chemotactic situation (Block et al., 1982). Because of this, tumbles are often assumed to be instantaneous, and the transition rate from tumble to run is ignored. This leaves one parameter: the transition rate from the run to the tumble state λ_{rt} usually called tumble rate λ_{rt}. The run time t_r is given by the rate's reciprocal $1/\lambda_{rt}$.

Since *P. putida* has three states of motion, there are a total of 6 rates and three life times to be considered. The time to change direction with a turn is even shorten than for *E. coli* and is assumed to be instantaneous. Transitions from turning to stopped state are forbidden, as cells can only stop in a run. The remaining 4 parameters we choose to express as the turn rate λ_{rt}, life time t_r, as well as the stop rate λ_{rs} and life time t_s.

The rates were calculated by counting transitions that occurred frame by frame and dividing by the recording frame rate:

$$\lambda_{ij} = n_{ij}/\Delta t \ . \tag{4.2}$$

The life times were computed by measuring runs and stops with clearly observed beginning and end events, and averaging these over the population.

The results of this analysis are shown in figure 4.33. Panels a and b show a significant

(a) transition rates, benzoate

(b) transition rates, casamino acids

(c) life times, benzoate

(d) life times, casamino acids
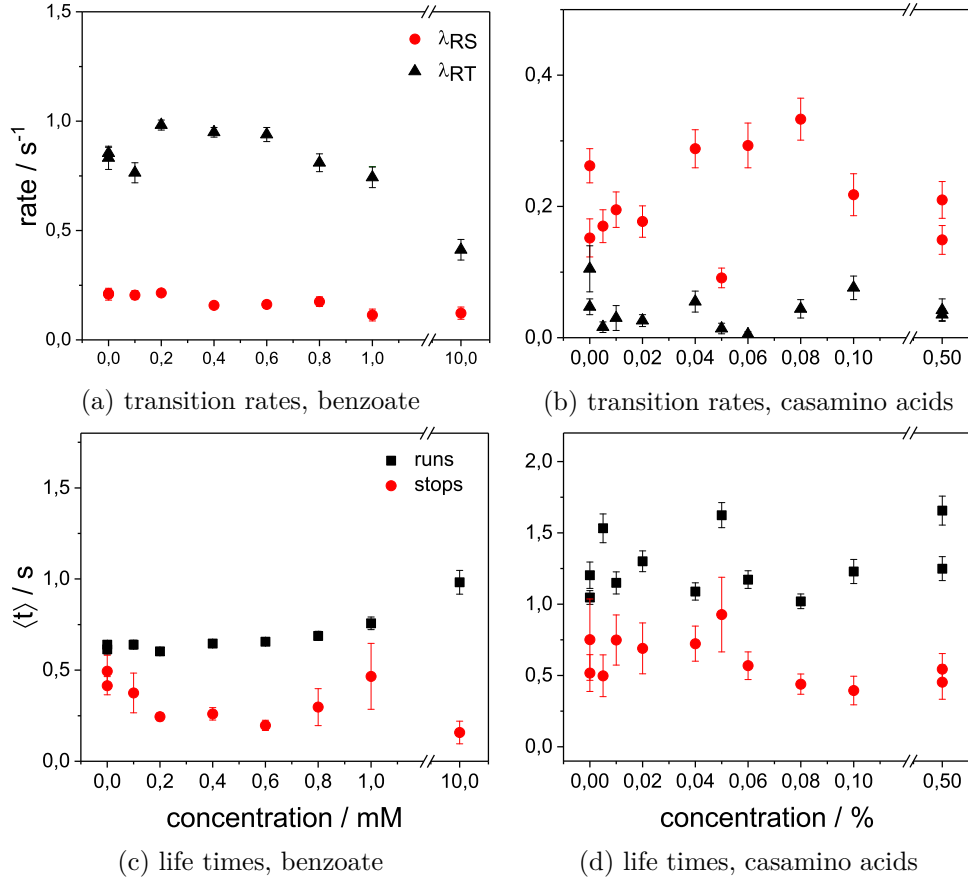
Figure 4.33.: Transition rates and life times in different media. (a) and (c): LB medium grown, benzoate added, (b) and (d) M9 medium grown, casamino acids added. Overall motility is strongly reduced in casamino acids, note the different ordinate scales in (b) and (d). Reproduced from Waljor (2016).

change from nutrient rich LB medium to nutrient poor M9 medium. Overall, the number of motile cells is significantly reduced: on average we detected 3.5 times fewer runs in casamino experiments compared to benzoate experiments, with an otherwise identical analysis pipeline. This is the reason the error bars and point spread for the casamino case are much larger than for benzoate. Within the error bounds, the stop rate is equal in both media, and mostly unaffected by the increasing chemoattractant concentration. The turn rate in contrast is decreased by an order of magnitude in rich medium and is even lower than the stop rate. Only slightly increased is the life time of stop states in the rich medium (panels c) and d – while the run time is increased by about one third. The fraction of time spend running is on average 85 % for both growth conditions.

One of the main results of this analysis was the measurement of the adaptation of *P. putida* cells in different attractants. In figure 4.33a and c it can be seen that

P. putida is not perfectly adapted for benzoate because the turn rate changes over the whole range of concentrations measured. For casamino acid chemotaxis the case is not as clear because of the larger spread of the results. However, both rates and life times appear to stay constant within the range of measurement fluctuation.

Based on the measurements from this section and the gradient measurements from subsection 4.3.3 we can conclude that *P. putida* is not perfectly adapted towards benzoate. This fact is clear, since two different methods based on gradients and homogeneous concentrations independently show a comparable increase of run times with increasing benzoate background concentration.

4.3.5. Discussion

In this section we investigated different possible strategies for *P. putida's* chemotaxis. The main finding is that it does *not* modulate its run modes or turning angles to achieve chemotaxis. Instead, it biases runs going up the gradient to be longer than runs down the gradient and thus follows the established model of bacterial chemotaxis (H. C. Berg, 2004). Older, more qualitative studies also show this lengthening of *P. putida's* runs after the addition of benzoate (Harwood, Fosnaugh, et al., 1989). In addition we could also show that *P. putida* is not perfectly adapted towards benzoate.

Its general motility strategy is however, more complex than that of other well studied bacteria. It has three different run modes (push, pull, and wrapped), and even occasionally stops in its tracks. A careful examination of these different modes – in this case only based on the run speeds – revealed no significant bias towards the attractive gradient. Neither the speeds of the modes themselves, nor their relative rate of occurrence changed significantly in the presence of attractive gradients.

Why then does *Pseudomonas putida* have these different run modes? Since we investigated only one kind of attractant, it is possible that *P. putida* behaves differently in the presence of other chemoattractants. Studies on *E. coli* chemotaxis with different chemoattractants have shown that the actual response varies for different compounds (H. C. Berg and Brown, 1972) and that there are nonlinear effects when multiple compounds are present (Wong-Ng et al., 2016). It is therefore possible that other attractants or repellents might elicit a chemotactic response in *P. putida* that modulates the three run modes in some way.

Otherwise it could also be possible that *P. putida* has evolved to swim with a wrapped, as well as an extended flagellum only in order to improve its motility in porous environments as discussed in subsection 4.1.3. In that case, no chemotactic modulation of the run modes can be expected.

Another interesting result is the selective reduction of fast (push/pull) mode swimming speed by the addition of benzoate. Since the slow (wrapped) mode speed remained largely unaffected, our hypothesis is that increasing benzoate concentrations just lower the maximal attainable rotation frequency of the motor, while a slower rotation speed remains unaffected. Studies on *Salmonella enterica* have shown that the presence of benzoate reduces the intracellular pH and total proton motive force, which leads to reduced swimming speeds (Minamino et al., 2003)

Compared to other chemoattractants the range of concentrations studied here is rather high. Whereas Harwood, Fosnaugh, et al. (1989) used 0.05 mM and 0.5 mM of benzoate for their *P. putida* chemotaxis experiments, *E. coli* is known to be able to sense amino acids down to nM concentrations. However, because the response of *P. putida* KT2440 was not previously quantified in our lab, we chose concentrations that were sure to elicit a chemotactic response. With the microfluidic technique used here it is also sometimes difficult to eliminate all unwanted flow and drift effects from the system. Therefore it was necessary to induce strong responses in order to be able to distinguish them from residual flow effects.

At the highest concentrations a slight reduction of mean swimming speeds occurs. The overall motility pattern is nonetheless unmodified, and cells are still drawn towards the attractant. If concentrations where still higher, we assume that the attraction towards the compound would become less or even reverse at some point. For further experiments with this chemoattractant, it would be advisable to reduce benzoate concentrations by one or even two orders of magnitude.

The role of the stops for chemotaxis and the general motility of *P. putida* and other *Pseudomonads* is not completely clear. In contrast to *R. sphaeroides'* stops, *P. putida's* are not principally involved in changing the direction between runs (Theves, 2013). Our preliminary findings also show that stops do *not* play a role in the chemotaxis towards benzoate (Waljor, 2016). They are nonetheless an important feature in *P. putida's* motility, as cells grown in rich medium spend as much as 10 % to 20 % of their time in stopped mode. Other studies on *Pseudomonas* chemotaxis have also not reported any influence of stops on chemotactic behavior, despite their prevalence in *P. putida*, *P. aeruginosa* and *P. fluorescens* (Qian et al., 2013; Cai et al., 2016). What advantage these stops confer to the bacteria and the role they play in the motility strategy of *Pseudomonads* remains to be investigated.

Section 4.3.4 highlights the importance of growth conditions for the motility of our model organism. When comparing our results with previous works on *P. putida* reported in Theves (2013), Bahrs (2013), Theves, Taktikos, et al. (2015), and Raatz et al. (2015), it should be noted that those studies used a very different growth protocol. In those studies, cells were grown in a rich peptone medium, diluted, and filled in to microchannels, where they were allowed to grow for circa 6 h. As Theves (2013) showed, the bacteria will first adhere to surfaces and grow there in a sessile biofilm state, before dispersing again in the bulk in a swimming state. Theves (2013) and Theves, Taktikos, et al. (2015) describe the bimodal speed of *P. putida* and report very similar values for the two speed modes (20 µm/s and 38 µm/s). Run times in their conditions are however significantly longer: 1.4 s in Theves (2013) and around 0.7 s in this study.

LB grow cells exhibit an overall decrease in the number of motile cells, as well as in time spend actually moving, i.e. in runs This behavior deviates somewhat from the previously reported motility pattern. A marked decrease in motile cells and increase in stopping times was also observed in cells prepared for the flagella stain, as well as in the homogeneous attractant experiments. The results reported in section 4.1 were all observed in *P. putida* grown in Tryptone broth. However, when grown in LB medium

and then subjected to the staining procedure, only about 10 % of individual cells were motile. Most of them had flagella, but showed no observable rotation. In agreement with the observations presented in this section, cells often would only start to swim after some time and then again stop. Most swimmers were running straight and no reversals could be observed during the limited fluorescence observation times.

In Davis et al. (2011, fig. 5) cells grown in LB medium and their swimming behavior was observed at different stages of the growth cycle. Here too, the trajectories are mostly straight with very few turns present.

Despite the differences between different growth protocols we can, in the end, conclude that the major characteristics of *P. putida's* motility seem to be robustly found in all growth conditions. This includes its turning angle distribution as well as its wrapped and extended flagella swimming modes.

4.4. Run-and-turn classification

The classification of bacterial swimming trajectories into runs and turns is a necessary step for most motility studies, but is not always easy. It has been approached with different techniques in the past. Here, we develop and use a novel algorithm to infer information about the chemotactic strategy of *E. coli* and *P. putida* without the need for a direct turn classification scheme. This algorithm can further be used to fully classify run and tumble sections of trajectories.

   We would like to thank Oliver Pohl, who devised and developed the new inference algorithm based on our data. The experiments, image analysis, tracking, and heuristic turn classification was performed by us, as described in section 3.8.1. The results and comparison of this joint effort were published in Pohl et al. (2017) and are presented below.

4.4.1. Method

Our novel approach is based on a stochastic two state model of the swimming motion. It assumes that the angle increments of the direction of motion have a known distribution, and that turn events are much faster than the duration of run. When in a run, cells will change their direction by a Brownian motion type process. A turn causes short bursts of angle increase, which are modeled with a shot noise process. An improvement over previous models is the necessity for only one free parameter: the time step of the procedure.
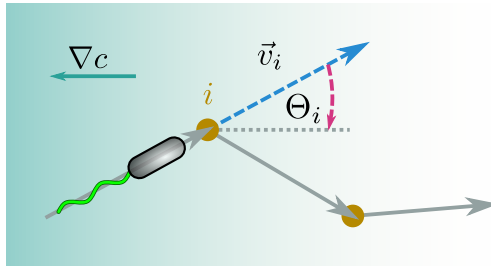
Figure 4.34.: Sketch of a cell swimming in a gradient.

   The method is based on a set of Langevin equations modeling the motion of a bacterium:

$$\dot{\mathbf{r}}(t) = v(t) \cdot \mathbf{e}(t) \ ,$$
$$\dot{\boldsymbol{\Theta}}(t) = q(t) + \xi(t) \ . \tag{4.3}$$

Here $\mathbf{r}$ and $\boldsymbol{\Theta}$ represent the position and the orientation angle of the bacterium, while $\mathbf{e} = (\cos\Theta, \sin\Theta)$ is the corresponding orientation vector. The swimming speed is denoted by $v(t)$, which decreases during a turn, but is otherwise ignored here. It focuses instead on the orientation angle. This angle is governed by two stochastic processes.

Firstly, white noise ξ characterized by $\langle \xi(t) \rangle = 0$ and $\langle \xi(s)\xi(t) \rangle = 2D_{\mathrm{rot}}\delta(t - s)$ and secondly a shot noise process $q(t)$. The shot noise is determined by

$$q(t) = \sum_{i=1}^{N^\lambda} \beta_i \delta(t - t_i) \ .$$

It is composed of a train of N^λ delta spikes at times t_i, where each spike has the amplitude β_i. Turns occur at a time varying rate $\lambda(t)$ and are Poisson distributed, as *E. coli* is known to have exponentially distributed waiting times between tumbles. Possible tumbling angles are symmetrically distributed around $\beta = 0$ and take values between $\beta = \pm\pi$. Their precise distribution depends on the species and the conditions studied.

Integration of equation 4.3 yields

$$\boldsymbol{\Theta}(t) = N(t) + B(t) \ , \tag{4.4}$$

where $B(t)$ is a Brownian motion with $P(dB) = \mathcal{N}(0, 2D_{\mathrm{rot}}\Delta t)$, and $N(t)$ the inhomogeneous Poisson process with rate $\lambda(t)$. In order to infer the parameters of these two sub-processes, we define the absolute conditional moment $m_{\Delta t}^n[\Theta]$ of order n for the stochastic process $\Theta(t)$ with a finite time step Δt,

$$m_{\Delta t}^n[\Theta] = \left\langle \frac{|\Theta(t + \Delta t) - \Theta(t)|_a^n}{\Delta t} \,\middle|\, \Theta(t) = \theta \right\rangle \ , \tag{4.5}$$

where $|\ldots|_a$ always gives the absolute value of the angle, such that it is smaller than π. It is important to note that Δt is finite and must be chosen such that it is larger than the mean tumbling time of the bacteria. These moments can then be calculated from experimental trajectories and are conditioned on the prior propagation direction $\Theta(t) = \theta$.

Because it is possible to derive analytical expressions for the conditional moments within the model assumptions, a set of non-linear equations for the moments on the left-hand side and the parameters of the sub-processes on the right-hand side can be obtained. These are the turn rate $\lambda(t)$, the moments of the turn angle distribution $\left\langle |\beta|^k \right\rangle$ and the rotational diffusion coefficient D_{rot}. Through a non-linear optimization procedure one can then obtain these unknown parameters and thus estimate the turn rate and the tumbling angle distribution of a population of swimming cells.

In effect, our method yields the information that is sought out by the application of a turn classification scheme – but without truly classifying runs and turns. However, this information can be used to obtain an a posteriori classification scheme with defined error probabilities. For more details on this method, as well as its extension to a true turn classifier, see Pohl (2016) and Pohl et al. (2017).

4.4.2. Analysis

A set of tracking experiments was performed with *E. coli* cells swimming in an aspartate gradient (0.5 mM/mm). The tracks were analyzed with the heuristic turn

classifier (section 3.8.1) used throughout this work and then with the novel inference algorithm (this section).

We also analyzed one subset (50 mM/mm) of the *P. putida* tracking data from the chemotaxis assay section section 4.3 with the heuristic, as well as the new algorithm to show its applicability to different motility pattern ans species. For the heuristic turn classifier, a number of parameters had to be adjusted in order to give results that agree with the literature consensus. The parameters are listed in table 4.5. A detailed explanation of the algorithm and the parameters is given in section 3.8.1.

Table 4.5.: Parameters for the turn classification algorithm

(a) *P. putida* datasets		(b) *E. coli* datasets	
parameter	value	parameter	value
α	3.5	α	1.0
ρ_v	0.2	ρ_v	0.45
γ	10.9	γ	3.5
ρ_ω	0.9	ρ_ω	0.85
$D_r/(\text{rad/s}^2)$	0.1	$D_r/(\text{rad/s}^2)$	0.1

E. coli

To test the efficacy of this method, we first calculated the tumbling angle distribution for *E. coli*, irrespective of the direction of the previous run. Based on the shape of the distribution of tumble angles observed in H. C. Berg and Brown (1972, Fig. 3), we use a γ distribution of tumbling angles β with

$$P\left(|\beta|\right) = \gamma(\sigma, k) = \frac{1}{\sigma^k\,\gamma_{\text{inc}}(k, \pi)}|\beta|^{k-1}\,e^{-|\beta|/\sigma}\ .$$

Here, $\gamma_{\text{inc}}(\sigma, k)$ is the lower incomplete γ-function. This choice of distribution is a heuristic one which only reflects the shape of the observed distribution. It is however needed in order to calculate the dependence of the conditioned moments on the tumble angles.

The model was then applied to a series of measurements of *E. coli* cells in a chemotaxis assay with the attractant aspartate. Trajectories were recorded at different time points after filling the gradient chamber (7 min, 12 min, 30 min, 45 min and 90 min). Figure 4.35 shows the tumble angle distributions obtained from these data sets with the heuristic and novel algorithm. The red dashed line is computed with the interference method by first smoothing the original data. Because the γ-distribution of *E. coli* tumbling angles was obtained from 3D trajectories, we need to multiply the heuristic 2D data by $\sin(\beta)$ to obtain a close agreement between the two methods (H. C. Berg, 2004). The corrected heuristic data is the dashed blue line.
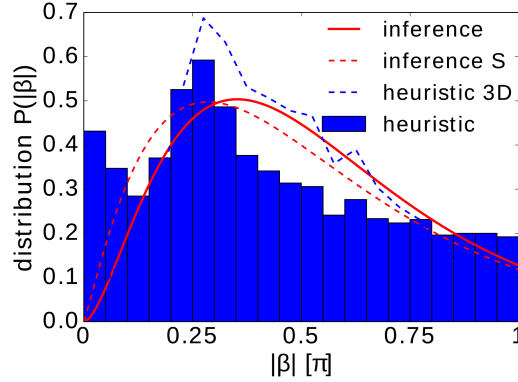
Figure 4.35.: Inferred tumble angle distribution of *E. coli*. The blue data are obtained from the heuristic tumble classifier in its original form (■) and multiplied by $\sin\theta$ (--). The red curves are inferred from the original (—) and smoothed data (--). Based on the data sets from 30 min to 90 min. Reproduced from Pohl et al. (2017)

The mean tumble angles and their standard deviations are $(76 \pm 49)°$ for the heuristic method and $(85 \pm 41)°$ for the inference method. This shows that both methods agree with each other within their error.

Next we measured the chemotactic modulation of *E. coli's* tumble statistics. To this end, the mean tumble angle $\langle|\beta|\rangle$ and the tumble rate were conditioned on the direction of the previous run (see section 2.4).

Our results, depicted in figure 4.36, show that the tumble rate in a linear gradient varies with the direction of the previous run. It decreases in the direction of the gradient ($\theta = \pi$), which means that runs down the gradient are longer than those upwards. This confirms the classical chemotaxis strategy of *E. coli* (H. C. Berg and Brown, 1972).

Furthermore, in first approximation, the concentration history of the bacterium depends linearly on the previous run's angle – see subsection 2.3.3, equation 2.6. This behavior is evident in all of the data sets and was well fitted with a cosine dependence, see figure 4.36, red line. This indicates, that the tumble angle modulation observed here is very well modeled by the underlying linear response theory (Celani and Vergassola, 2010; Celani and Vergassola, 2012).

The mean tumble rates are 0.28/s and 0.24/s for early and late times, respectively. They agree well with published values for the tumble rate of *E. coli* within the usual margins (Rosser, Fletcher, et al., 2013).

When conditioning the mean tumble angle on the previous run direction, we found that after 30 min no significant modulation of the tumble angle occurs. This reflects the generally accepted model that *E. coli* tumble angles are completely random in magnitude.

Our early data sets at 7 min and 12 min, however, show a different behavior. There, we find evidence for a relative decrease of tumble angles that occur after runs upward

(a) 30 to 90 minutes   (b) 7 and 12 minutes
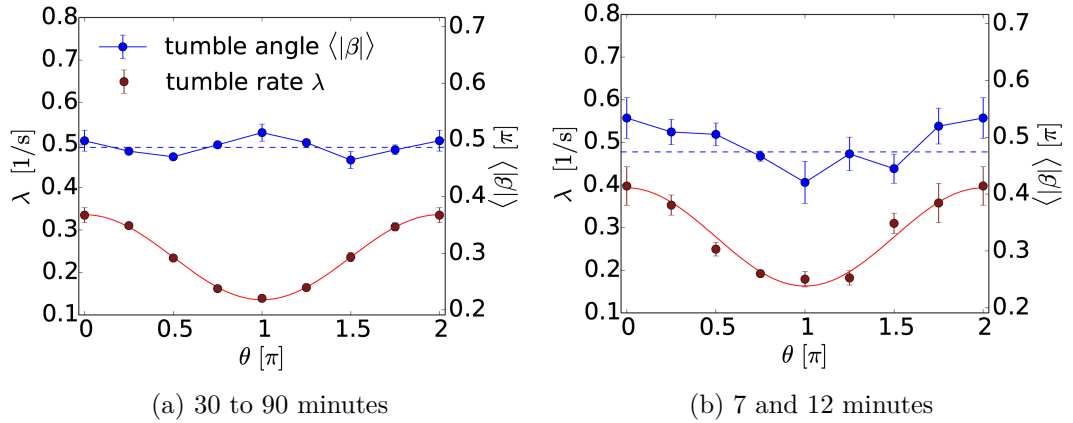
Figure 4.36.: Conditioned tumble statistics at different recording times. Mean tumble rate λ (●) and mean tumble angle β (●) for different prior run angles θ. The gradient points into the direction $\theta = \pi$. The tumble rate is fitted by a cosine function (—), and the dotted blue line indicates the tumble angle averaged of all directions (--). Reproduced from Pohl et al. (2017).

the gradient ($\theta \approx \pi$). Bacteria that were swimming in the right direction, have a reduced tumble angle compared to those that were swimming in the wrong direction. Biasing the tumbling angle in this way, leads to an increased chemotactic efficiency. We can therefore conclude that some of the cells in our experiments use this mechanism to increase their chemotactic efficiency. They probably appear first in the gradient chamber because of this high efficiency. Other studies have also gathered evidence, that *E. coli* may bias its tumble angles (Saragosti et al., 2011). A possible mechanism for this behavior could be the coordinated reversal of multiple motors (Terasawa et al., 2011) in conjunction with the fact that tumble angles tend to be larger, the more motors are involved in the tumble (Turner, W. S. Ryu, et al., 2000).

P. putida

We then applied the inference algorithm to the data set of *P. putida* swimming in a $5\,\mathrm{mM/mm}$ benzoate gradient and classified the turns in its swimming motion. Because this analysis was performed before the exact nature of the different run types of *P. putida* was known to us, we do not consider different run modes in the following section. The different run speeds observed in *P. putida* are also ignored, as this method only considers changes in direction.

In order to capture the peak at 180° we chose

$$P\left(|\beta|\right) = \frac{1}{\mathcal{N}} \left(e^{-(\pi-|\beta|)/\Delta\beta} + C \right)$$

as the turning angle distribution. Here, $\mathcal{N}$ is the normalization constant and $\Delta\beta$ a rate parameter which reflects the width of the distribution. The constant offset C
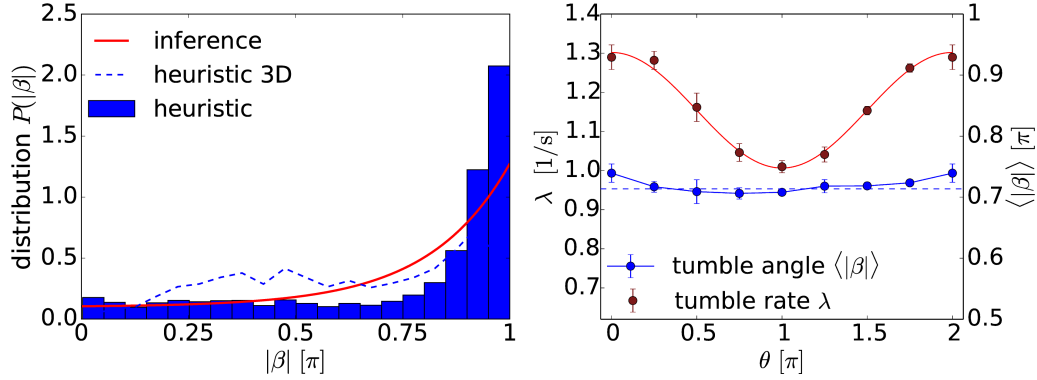
(a) Turning angle distribution. Data from the heuristic tumble classifier without (■), and with 3D correction (--). Red curve is inferred with the new classifier (—).

(b) Conditioned tumbling statistics. Curves are a cosine fit of the tumble rate (—), and the average tumble angle (--).

Figure 4.37.: Inferred turning statistics of *P. putida*. The gradient points into the direction $\theta = \pi$. Reproduced from Pohl et al. (2017)

reflect the small amount of classified turns at small angles. In figure 4.37a the turning angle distribution inferred from our data is shown. It agrees reasonably well with the heuristic method, similar to the *E. coli* case.

The turn rate conditioned on the previous run direction is shown in figure 4.37b. Again the rate varies with the cosine of the angle, but no significant variation of the turning angle is present. This reflects our result obtained in section 4.3: *P. putida* performs chemotaxis only by biasing its turning rate and not by any other means.

4.4.3. Discussion

Based on a stochastic model for the movement of swimming bacteria, we employed a novel algorithm to infer the turn rate, turn distribution parameters and rotational diffusion constant from tracking data. The method needs only a time scale Δt and a parameterized turn angle distribution $P(\beta)$. It produces results consistent with other methods and with literature values. Furthermore, it can successfully be generalized into a complete turn classification scheme (Pohl et al., 2017).

Using this method we recapture the well known turn angle distributions of *E. coli* and *P. putida*, as well as their chemotactic strategy. Compared to other methods of obtaining tumbling and chemotaxis statistics this method less free parameters and is more broadly applicable. This is exemplified by its application to two species with very different flagellation and motility patterns. It produces robust results comparable to more complex methods such as the Hidden Markov Model based scheme by Rosser, Fletcher, et al. (2013), where multiple experiments with motility mutants have to be performed.

5. Conclusion

5.1. Summary

The swimming of bacteria differs significantly between species with different numbers and locations of flagella (Taute et al., 2015). Studies of bacterial motility have mostly focused on peritrichous bacteria like *E. coli* and *Salmonella*, as well as monotrichous ones like *V. alginolyticus.*

In order to shed light on the relationship between flagellation and motility pattern we studied a lophotrichous swimmer with a polar bundle of flagella, which was known to deviated from the classical run-and-tumble pattern. Using high speed fluorescence imaging we observed the bacterium swimming with three different modes of flagellar arrangements. It shows a newly discovered mode of propagation, were it can wrap its flagella around the cell body. Furthermore, it can swim with a stable pushing and pulling bundle, which had not been observed in other bacteria before. We have revealed in detail the possible transitions between swimming states, as well as the associated dynamics of the flagellar bundle. Based on these observations, we could consolidate the previously observed motility pattern of *P. putida* in our model of three phase motility.

In pushing mode the flagella form a tight bundle, that trails behind the cell body and pushes the cell – just like in peritrichous and monotrichous bacteria. In pulling mode the bundle is leading in front of the cell body and pulls the cell. This behavior is reminiscent of the push-pull motility observed in monotrichous bacteria, but was usually not considered a possibility for multitrichous species. Furthermore, our model bacterium is able to swim with its flagella wrapped around the cell body – the first time this behavior has been observed for a bacterium wih multiple flagella. This mode deviates markedly form normal push or pull swimming where the flagella are extended away form the cell body. In wrapped mode, the motors rotate only half as fast as in the other to modes. At the same time the flagella assume a different physical conformation – or polymorphic state – which we attribute to the change in motor torque applied to the flagella. These polymorphic transitions likely are necessary for a complete transitions from and to the wrapped mode. Switching between modes occurred rapidly and synchronously with all flagella at the same time. This shows that the motors must be coupled more strongly than in peritrichous bacteria, where only a weak diffusive coupling is present (Terasawa et al., 2011).

As of the writing of this thesis, swimming with wrapped flagella had just been discovered in four species: *Shiwanella putrefaciens* (Kühn et al., 2017), *P. putida* (Hintsche et al., 2017), a *Burkholderia sp.* and *Aliivibrio fischeri* (Kinosita et al., 2017). We showed in subsection 4.1.3 that more species could exhibit this behavior than have

been directly observed in those three recent studies. With our three state swimming model, we can explain the swimming patterns of three other species previously reported in the literature. In particular, we find indirect but compelling evidence of wrapped swimming in *P. fluorescens* (Ping et al., 2013, fig. 1 and 3)), *P. citronellis* (Taylor and Koshland, 1974, fig. 1) and *M. magnetotacticum* (Murat et al., 2015, fig. 2) (also see the detailed discussion on page 54).

Because older observations of moving flagella *in situ* have relied on dark field microscopy (H. C. Berg, 1975), or less sophisticated staining techniques (Turner, W. S. Ryu, et al., 2000), flagella close to the cell body could not be resolved. The advent of highly specific staining has now enabled much more detailed examination of flagellar dynamics (Turner, Zhang, et al., 2010; Turner, Ping, et al., 2016).

All of this evidence points to a rather common wrapped mode in multiple species of bacteria, with one or more polar flagella. Apparently, even amphitrichously flagellated bacteria, where flagella are attached to both poles of a cell, use this swimming conformation (e.g. *M. magnetotacticum*). Historically the study of bacterial swimming was focused on peritrichous bacteria and an important mode of bacterial swimming was overlooked.

We could show that in *P. putida's* case the wrapped mode improves the diffusive spreading of a population on longer time scales. Others have shown that viscous and restrictive environments increase the prevalence of this mode of swimming (Kühn et al., 2017). However, other advantages conferred by this mode and the selection pressures that shaped it remain yet to be uncovered.

The environment of *P. putida* is structured on many length scales. By using microfluidic techniques, we created channels which were artificially structured on length scales similar to those encountered in the soil. We used microchannels in which cylindrical obstacles were arranged on a hexagonal lattice. Through variations of the obstacle sizes and distances we could probe the influence of environments with different porosity on the swimming behavior of our soil-dwelling model organism. We tracked the bacteria in the channels and observed different types of obstacle interactions. They could lead to either a collision with reorientation of the swimming path, or a transient hydrodynamic capture of the cells. By comparing run lengths with the theoretical prediction for a dynamical billiards situation, we concluded that hydrodynamic interactions and subsequent guiding of bacteria along the obstacles dominate reorientation effects due to the obstacles. We could further show that the hydrodynamics lead to a significant increase of run length for obstacles smaller than $15\,\mu\text{m}$.

One of the most important functions of cell motility is the ability to respond to environmental cues by moving in a directed manner. We therefore analyzed the behavior of our model organism in chemical gradients of varying strengths. Using a microfluidic device to generate linear gradients of the aromatic acid benzoate, we recorded and tracked cells swimming in these gradients. Their motion was analyzed with a custom software, written in Matlab, to extract key motility parameters and chemotaxis indicators. The analysis revealed, that *P. putida* performs chemotaxis by biasing runs up the gradient to be longer than down the gradient, which is the classical strategy employed by *E. coli*. We also concluded that its different swimming modes do not

play a role in the chemotaxis towards benzoate.

Based on our discovery of *P. putida's* swimming modes, we applied a Gaussian Mixture Model (GMM) to classify tracked runs into wrapped and extended modes, without direct observation of the swimming states. We found that the modes are not biased by its chemosensory pathway in benzoate gradients. By analyzing data in gradients and homogeneous attractant concentrations, we also showed that *P. putida* is not perfectly adapted to benzoate. Increasing benzoate concentrations influenced not only the run times but also the speed of runs. Interestingly, extended mode runs, were disproportionately affected by high concentrations.

Because traditional run-and-tumble classification is dependent on various parameters that must be tuned by hand, we, together with Oliver Pohl and Holger Stark, developed a new tumble classification algorithm for *E. coli*, which could be used equally well for *P. putida* (Pohl, 2016; Pohl et al., 2017). Based on our tracking experiments in microfluidic gradient chambers, we found that *E. coli* populations were heterogeneous with respect to their chemotactic ability to climb linear gradients. Cell that swam from the reservoir region into the gradient region had significantly reduced tumble rates shortly after the start of the experiment. We propose that this is a selection effect, because cells that respond faster to trace amounts of chemoattractant will arrive faster in the observation region. Additionally, we could show that those early swimmers exhibit a chemotactic angle bias, which means they suppress larger tumbling angles when swimming up the gradient in order to not deviate too much from the right direction.

In conclusion we successfully employed microscopic observation and cell tracking at different time scales to uncover the details of *P. putida's* motility scheme and revealed key features of its swimming behavior that were unexplained before. Using high speed fluorescence microscopy we uncovered three distinct swimming modes for the first time in a multi-flagellated bacterium. Through automated trajectory analysis, we investigated the effect of our model organism's swimming mode on its navigation in chemical gradients, and tested a novel parameter-less tumble classification scheme.

5.2. Outlook

Our study brings out a number of questions, concerning the details and advantages of this motility pattern in bacteria. These new questions, as well as remaining problems are discussed below.

In view of the recent discovery of the novel wrapping behavior in multiple, not closely related, bacterial species, we can assume that this wrapping of flagella around the cell body confers some advantages for locomotion. For example, the wrapping of flagella around the cell body has also been observed in the context of viscous media and trapped *Shewanella* cells (Kühn et al., 2017). Increasing the viscosity of the medium and observing the dynamics of flagellar wrapping in *P. putida* could therefore yield more insight into the torque dependence of the wrapping transition. In conjunction to this, numerical simulations of the flagellum mechanics could further help to understand

the polymorphic transitions and their triggers that lead to wrapping (Vogel and Stark, 2012; Vogel and Stark, 2013).

The observation of completely synchronized bundle reversals raises the question of how motor synchronization is achieved. Due to the polar arrangement and therefore close proximity of the motors in *P. putida* allosteric interaction of motor patches might lead to a strong motor coupling, similar to that in the chemotaxis receptor arrays (Duke and Bray, 1999; Bray, 2013). However, direct visualization of motor complexes – for example via immunogold labeling – is necessary to understand their precise locations and arrangement. More work of a more molecular biological character is needed to elucidate the synchronization mechanism.

It is also not clear how the control of the three swimming states is performed, when classically only CheY, which stands at the output of the chemotaxis signal cascade, regulates motor bias. Is the motor speed that causes transitions from extended to wrapped modes regulated separately, or does it just follow a stochastic sequence of events? This and the following questions will need the probing of single chemotaxis proteins by knock-out strains or other mutants. These kinds of experiments could also elucidate the function of the Che-system homologues that are present in *P. putida* but whose functions are only partially known as of yet (García-Fontana et al., 2013).

Another approach which has become feasible in the recent past, is the long term observation of swimming bacteria with wide field microscopy, combined with intermittent fluorescence observation of the bundle conformation (Turner, Ping, et al., 2016). In our case, this would allow for a precise description of the swimming state, as well as the ability to gather more and longer tracks with multiple transitions. This would allow a detailed analysis of the individual transition rates between different states. When combined with chemical cues such as gradients or even homogeneous attractant profiles, this kind of measurement would shed more light on the details of the control of motor speed and sense of rotation.

From a very general stand point one could ask in what sense a motility and chemotaxis strategy is optimal. We know, for example, that gradient climbing speed alone is not necessarily optimal (Celani and Vergassola, 2010; Masson et al., 2012), especially with multiple chemotactic requirements (Wong-Ng et al., 2016). *P. putida's* strategy may be advantageous in structured and complex, porous environments (Ranjard and Richaume, 2001).

P. putida, its three state motility, and the wrapped mode in general, will provide ample ground for further research.

A. Appendix

A.1. Methods

A.1.1. Construction of the FliC mutant

The following work to enabling the fluorescent staining of *P. putida* flagellar filaments was performed by Marco Kühn and Kai Thormann, who we kindly thank for constructing and providing the strain to us (Hintsche et al., 2017; Kühn et al., 2017).

To enable ligation of fluorescent maleimide-ligated dyes to assembled flagellar filaments of *P. putida*, we introduced a surface-exposed cysteine residue to the building block of the filament, the protein flagellin (FliC, PP_4378). Serine 267 (Ser267) was selected for an appropriate serine to cysteine substitution based on flagellin sequence alignments and modeling of the *P. putida* flagellin structure similarly as described for *S. putrefaciens* (Kühn et al., 2017). For the genetic substitution, flagellin-encoding *fliC* was first deleted and subsequently chromosomally replaced by the mutant variant by sequential homologous crossover essentially as previously described (Lassak et al., 2010; Kühn et al., 2017). The corresponding genetic fusions or gene variants were constructed by PCR using appropriate primers and cloned into suicide vector pNPTS138-R6K by Gibson assembly (Gibson, 2009) in *E. coli* DH5α\lambda pir (Miller and Mekalanos, 1988). The vector was transferred to *P. putida* by conjugation with *E. coli* WM3064 (W. Metcalf, University of Indiana, Urbana, Champaign) as donor, using the standard protocol developed for *Shewanella* (Lassak et al., 2010). All procedures were carried out on LB medium supplemented with $50\,\mu g/ml$, $300\,\mu M$ 2,6-diaminoheptanedioic acid, and/or $10\,\%(w/v)$ sucrose when appropriate. The swimming capacity of the resultant strain *P. putida* FliC$_{S267C}$ was tested by determining the spreading of the mutant on $0.3\,\%$ LB soft-agar plates directly compared to that of the wild type. Since no difference in motility on soft-agar plates occurred, we concluded that the Ser278Cys substitution does not negatively affect assembly and function of the flagellar filament.

A.1.2. Experimental

Table A.1.: Chemoattractant concentrations used for the adaptation measurements

attractant	concentration					
benzoate / (mM)						
log spacing	0	0.1	1	10		
linear spacing	0	0.1	0.2	0.4	0.6	0.8
casamino acids / (g/ml)						
log spacing	0	0.005	0.01	0.05	0.5	
linear spacing	0	0.02	0.04	0.06	0.08	

A.2. Results

A.2.1. Flagellar dynamics

Table A.2.: Summary of swimming state and transition statistics. For a graphical representation see figure 4.1, page 40 and figure 4.11a, page 47.

(a) frequency of states

state	frequency	fraction/%
push	645	81
pull	80	10
wrap	69	9
total	794	

(b) frequency of transitions

transition	frequency	fraction/%
pull-to-push	14	17
push-to-pull	31	39
pull-to-wrap	15	19
wrap-to-push	20	25
total	80	

Table A.3.: Videos of bacteria with stained flagella All videos are available on the enclosed CD. Some are also available online as part of the electronic supplementary information of Hintsche et al. (2017) (web link for the PDF version of this document).

movie no.	description	web link
1	Swimming as a pusher	[1]
2	Swimming as a puller	[2]
3	Transition from pushing to pulling	[3]
4	Swimming with the flagella wrapped around the cell body	[4]
5	Handedness of the flagella in wrapped mode	[5]
6	Swimming as a pusher with frequent stops	[6]
7	Swimming as a pusher with loose bundle interrupted by a stop	[7]
8	Transition from pulling to pushing	[8]
9	Transition from a pulling to a wrapped bundle	[9]
10	Transition from a pulling to a wrapped bundle of an immobilized cell	[10]
11	Transitions from a pulling to a wrapped bundle and from a wrapped to a pushing bundle	[11]
12	Transition from a wrapped to a pushing bundle of an immobilized cell	[12]
13	Transitions without change in the polymorphic state of the flagella	[13]
20	Transition from pull to wrap, tracked with ImageJ's TrackMate	
21	Wrapped swimmer coming into focus, helix handedness was determined from these events	
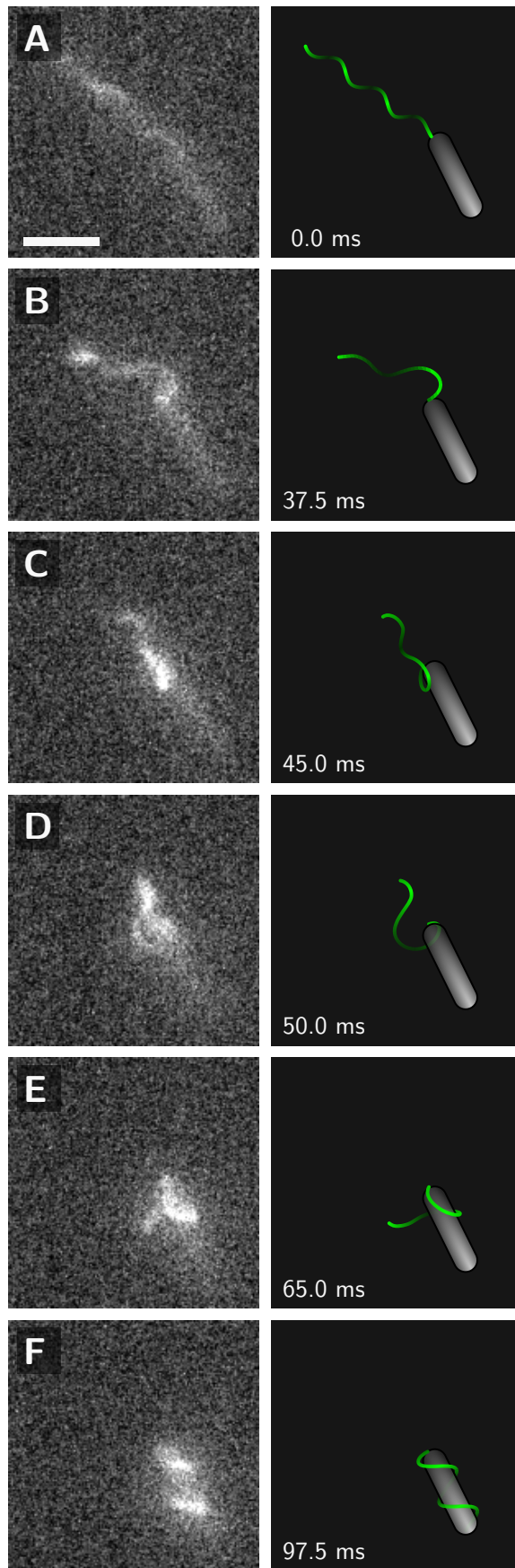
Figure A.1.: Pull to wrapped transition of a cell stuck to the cover slip. Snapshots from a fluorescence microscopy recording of a cell stuck to the cover slip. The flagellum rotates freely in CCW direction throughout. Scale bar is 3 µm. (See movie 10.)
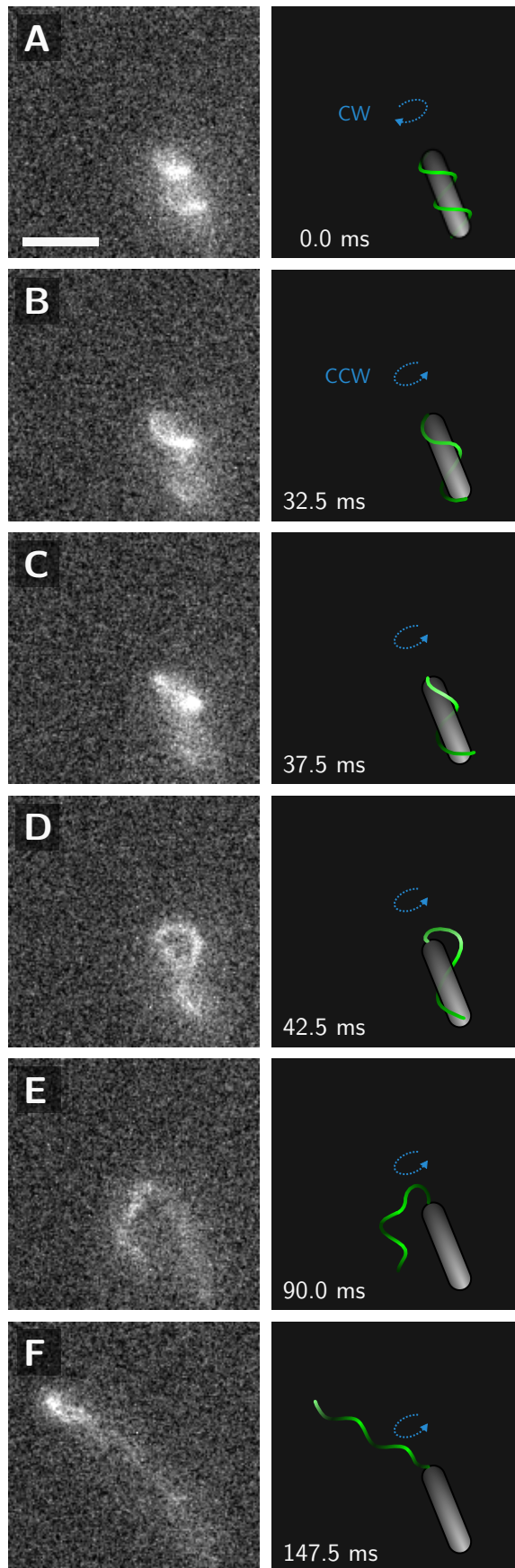
Figure A.2.: Wrapped to push transition of a cell stuck to the cover slip. Snapshots from a fluorescence microscopy recording of a cell stuck to the cover slip. The flagellum can rotate freely. The sense of rotation changes from CW to CCW just before panel **B** (indicated by the blue arrow). Scale bar is 3 µm. (See movie 12.)
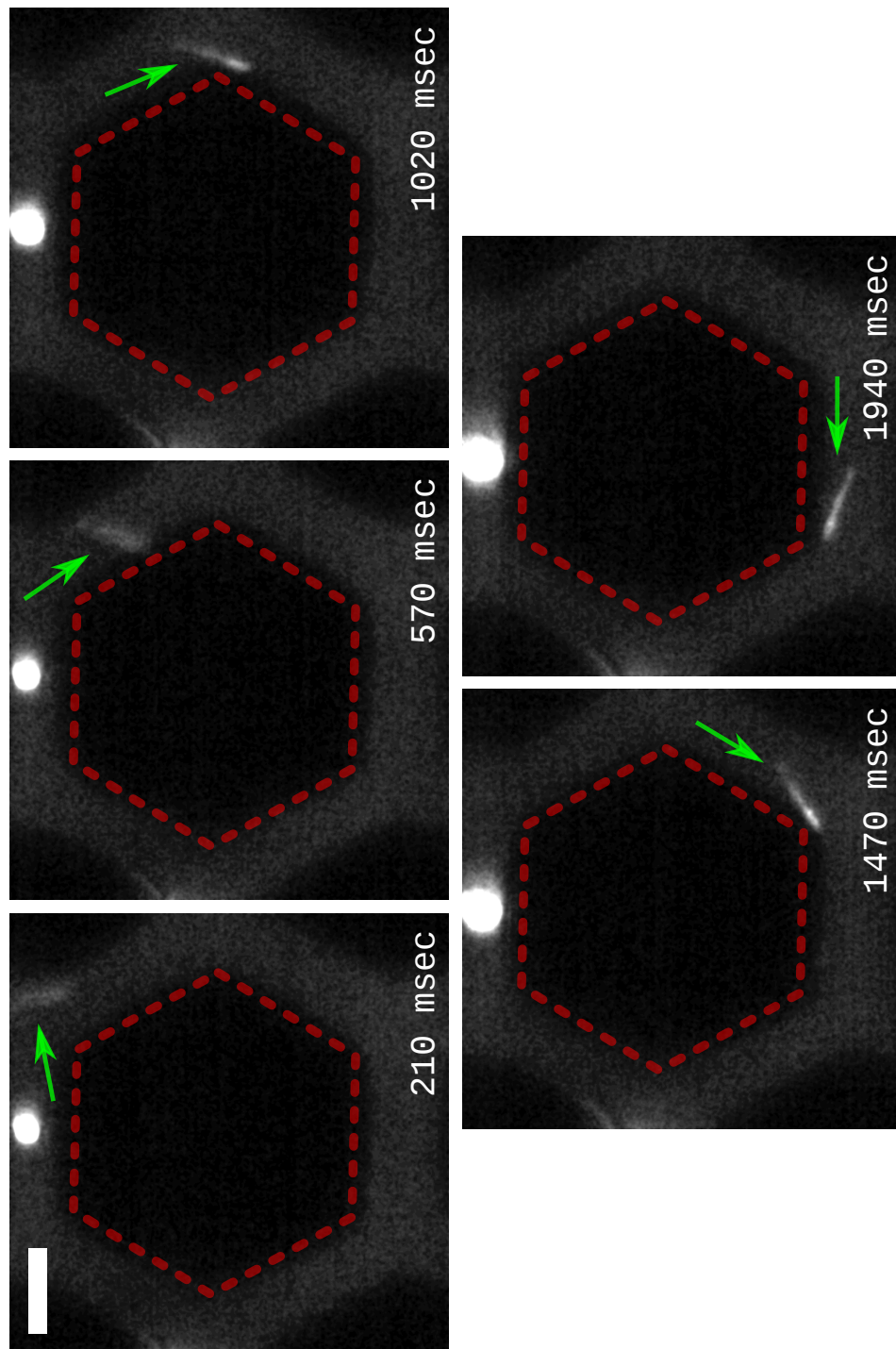
Figure A.3.: Montage of a cell with stained flagella swimming in a structured microchannel. Scale bar is $10\,\mu$m.

Bibliography

Adler, J. (1969). "Chemoreceptors in Bacteria". In: *Science* 166.3913, pp. 1588–1597.

Ahmed, T. and R. Stocker (2008). "Experimental Verification of the Behavioral Foundation of Bacterial Transport Parameters Using Microfluidics". In: *Biophysical Journal* 95.9, pp. 4481–4493.

Alon, U. et al. (1999). "Robustness in bacterial chemotaxis". In: *Nature.*

Armitage, J. P. and R. M. Macnab (1987). "Unidirectional, intermittent rotation of the flagellum of *Rhodobacter sphaeroides*". In: *J. Bacteriol.* 169.2, pp. 514–518.

Armitage, J. P., T. P. Pitta, et al. (1999). "Transformations in flagellar structure of *Rhodobacter sphaeroides* and possible relationship to changes in swimming speed". In: *J. Bacteriol.* 181.16, pp. 4825–4833.

Armitage, J. P. and R. Schmitt (1997). "Bacterial chemotaxis: *Rhodobacter sphaeroides* and *Sinorhizobium meliloti* - variations on a theme?" In: *Microbiology* 143.12, pp. 3671–3682.

Attmannspacher, U. et al. (2005). "Control of speed modulation (chemokinesis) in the unidirectional rotary motor of *Sinorhizobium meliloti*". In: *Molecular Microbiology* 56.3, pp. 708–718.

Bahrs, M. (2013). "Swimming microorganisms near circular obstacles and boundaries". Bachelor's thesis. Universität Potsdam.

Belda, E. et al. (2016). "The revisited genome of *Pseudomonas putida* KT2440 enlightens its value as a robust metabolic chassis". In: *Environmental Microbiology* 18.10, pp. 3403–3424.

Berg, H. C. (1975). "Chemotaxis in Bacteria". In: *Annual Review of Biophysics and Bioengineering* 4.1, pp. 119–136.

Berg, H. C. and R. A. Anderson (1973). "Bacteria swim by rotating their flagellar filaments". In: *Nature* 245, pp. 380–382.

Berg, H. C. and L. Turner (1990). "Chemotaxis of bacteria in glass capillary arrays. *Escherichia coli*, motility, microchannel plate, and light scattering". In: *Biophysical Journal* 58.4, pp. 919–930.

Berg, H. and E. Purcell (1977). "Physics of chemoreception". In: *Biophysical Journal* 20.2, pp. 193–219.

Berg, H. C. (1993). *Random Walks in Biology.* Princeton University Press.

– (2003). "The Rotary Motor of Bacterial Flagella". In: *Annual Review of Biochemistry* 72, pp. 19–54.

– (2004). *E. coli in Motion.* Springer-Verlag.

Berg, H. C. and D. A. Brown (1972). "Chemotaxis in *Escherichia coli* analysed by Three-dimensional Tracking". In: *Nature* 239.5374, pp. 500–504.

Berke, A. P. et al. (2008). "Hydrodynamic Attraction of Swimming Microorganisms by Surfaces". In: *Phys. Rev. Lett.* 101.3, p. 038102.

Berry, R. M. and H. C. Berg (1997). "Absence of a barrier to backwards rotation of the bacterial flagellar motor demonstrated with optical tweezers." In: *Proceedings of the National Academy of Sciences of the United States of America* 94 (26), pp. 14433–14437.

Bishop, C. M. (2006). *Pattern Recognition and Machine Learning.* Springer-Verlag New York Inc. 738 pp.

Blair, D. and E. Dufresne (2008). *The Matlab Particle Tracking Code Repository.* online.

Block, S. M. et al. (1982). "Impulse responses in bacterial chemotaxis". In: *Cell* 31.1, pp. 215–226.

Bray, D. (2013). "The Propagation of Allosteric States in Large Multiprotein Complexes". In: *Journal of Molecular Biology* 425.9, pp. 1410–1414.

Bray, D. et al. (1998). "Receptor clustering as a cellular mechanism to control sensitivity". In: *Nature* 393.6680, pp. 85–88.

Cai, Q. et al. (2016). "Singly Flagellated *Pseudomonas aeruginosa* Chemotaxes efficiently by Unbiased Motor Regulation". In: *mBio* 7.2, e00013–16.

Celani, A. and M. Vergassola (2010). "Bacterial strategies for chemotaxis response". In: *Proceedings of the National Academy of Sciences* 107.4, pp. 1391–1396.

– (2012). "Nonlinearity, Fluctuations, and Response in Sensory Systems". In: *Phys. Rev. Lett.* 108.25, p. 258102.

Chakrabarty, A. (1981). *Microorganisms having multiple compatible degradative energy-generating plasmids and preparation thereof.* US Patent 4,259,444.

Chattopadhyay, S. et al. (2006). "Swimming efficiency of bacterium *Escherichia coli*". In: *Proceedings of the National Academy of Sciences* 103.37, pp. 13712–13717.

Chen, X. and H. C. Berg (2000). "Torque-Speed Relationship of the Flagellar Rotary Motor of *Escherichia coli*". In: *Biophysical Journal* 78.2, pp. 1036–1041.

Clark, D. A. and L. C. Grant (2005). "The bacterial chemotactic response reflects a compromise between transient and steady-state behavior". In: *Proceedings of the National Academy of Sciences* 102.26, pp. 9150–9155.

Constantino, M. A., M. Jabbarzadeh, et al. (2016). "Helical and rod-shaped bacteria swim in helical trajectories with little additional propulsion from helical shape". In: *Science Advances* 2.11, e1601661–e1601661.

Constantino, M. A., S. Sharba, et al. (2017). *Effects of number and configuration of flagella on motility of Helicobacter species.* Conference talk abstract.

Costerton, J. W. et al. (1999). "Bacterial Biofilms: A Common Cause of Persistent Infections". In: *Science* 284.5418, pp. 1318–1322.

Crocker, J. C. and D. G. Grier (1996). "Methods of Digital Video Microscopy for Colloidal Studies". In: *Journal of Colloid and Interface Science* 179.1, pp. 298–310.

Darnton, N. C. and H. C. Berg (2007). "Force-extension measurements on bacterial flagella: triggering polymorphic transformations". In: *Biophysical journal* 92.6, pp. 2230–2236.

Darnton, N. C., L. Turner, et al. (2007). "On Torque and Tumbling in Swimming *Escherichia coli*". In: *J. Bacteriol.* 189.5, pp. 1756–1764.

Davis, M. L. et al. (2011). "2D motility tracking of *Pseudomonas putida* KT2440 in growth phases using video microscopy". In: *Journal of Bioscience and Bioengineering* 111.5, pp. 605–611.

Dempster, A. P. et al. (1977). "Maximum Likelihood from Incomplete Data via the EM Algorithm". In: *Journal of the Royal Statistical Society. Series B (Methodological)* 39.1, pp. 1–38.

DePamphilis, M. L. and J. Adler (1971). "Fine structure and isolation of the hook-basal body complex of flagella from *Escherichia coli* and *Bacillus subtilis*". In: *J. Bacteriol.* 105.1, pp. 384–95.

Ditty, J. L. et al. (1998). "Identification of a chemotaxis gene region from *Pseudomonas putida*". In: *FEMS Microbiology Letters* 159.2, pp. 267–273.

Duffy, K. J., P. T. Cummings, et al. (1995). "Random walk calculations for bacterial migration in porous media". In: *Biophysical Journal.*

Duffy, K. J. and R. M. Ford (1997). "Turn angle and run time distributions characterize swimming behavior for *Pseudomonas putida*". In: *J Bacteriol* 179.4, pp. 1428–1430.

Duke, T. A. J. and D. Bray (1999). "Heightened sensitivity of a lattice of membrane receptors". In: *Proceedings of the National Academy of Sciences* 96.18, pp. 10104–10108.

Ehlers, K. and G. Oster (2012). "On the Mysterious Propulsion of Synechococcus". In: *PLoS ONE* 7.5. Ed. by C. M. Aegerter, e36081.

Falke, J. J. et al. (1997). "THE TWO-COMPONENT SIGNALING PATHWAY OF BACTERIAL CHEMOTAXIS: A Molecular View of Signal Transduction by Receptors, Kinases, and Adaptation Enzymes". In: *Annual Review of Cell and Developmental Biology* 13.1, pp. 457–512.

Friedrich, B. M. and F. Jülicher (2007). "Chemotaxis of sperm cells". In: *Proceedings of the National Academy of Sciences* 104.33, pp. 13256–13261.

García-Fontana, C. et al. (2013). "High Specificity in CheR Methyltransferase Function". In: *Journal of Biological Chemistry* 288.26, pp. 18987–18999.

Gennes, P.-G. de (2004). "Chemotaxis: the role of internal delays". In: *European Biophysics Journal* 33.8, pp. 691–693.

Gibson, D. (2009). "Enzymatic assembly of DNA molecules up to several hundred kilobases". In: *Nat. Methods* 6.5, pp. 343–345.

Gonzalez, R. et al. (2009). *Digital Image Processing Using MATLAB*. 2nd. McGraw Hill Education.

Hamer, R. et al. (2010). "Deciphering chemotaxis pathways using cross species comparisons". In: *BMC Systems Biology* 4.1, p. 3.

Harwood, C. S., K. Fosnaugh, et al. (1989). "Flagellation of *Pseudomonas putida* and analysis of its motile behavior". In: *J Bacteriol* 171.7, pp. 4063–4066.

Harwood, C. S., R. E. Parales, et al. (1990). "Chemotaxis of *Pseudomonas putida* toward chlorinated benzoates". In: *Applied and Environmental Microbiology* 56.5, pp. 1501–1503.

Bibliography

Harwood, C. S., M. Rivelli, et al. (1984). "Aromatic acids are chemoattractants for *Pseudomonas putida*". In: *J Bacteriol* 160.2, pp. 622–628.

Hasegawa, E. et al. (1982). "Thermal transition in helical forms of *Salmonella* flagella". In: *Journal of Molecular Biology* 160.4, pp. 609–621.

Hasegawa, K. et al. (1998). "Quasi- and Nonequivalence in the Structure of Bacterial Flagellar Filament". In: *Biophysical Journal* 74.1, pp. 569–575.

Hintsche, M. et al. (2017). "A polar bundle of flagella can drive bacterial swimming by pushing, pulling, or coiling around the cell body". In: *Sci. Rep.*

Hirano, T. et al. (1994). "Roles of FliK and FlhB in determination of flagellar hook length in *Salmonella typhimurium*". In: *Journal of Bacteriology* 176.17, pp. 5439–5449.

Homma, M. et al. (1996). "Chemotactic responses to an attractant and a repellent by the polar and lateral flagellar systems of *Vibrio alginolyticus*". In: *Microbiology* 142.10, pp. 2777–2783.

Inmaculada Sampedro Rebecca E. Parales, T. K. and J. E. Hill (2015). "*Pseudomonas* chemotaxis". In: *FEMS Microbiology Reviews* 39.1, pp. 17–46.

Jarrell, K. F. and M. J. McBride (2008). "The surprisingly diverse ways that prokaryotes move". In: *Nature Reviews Microbiology* 6.6, pp. 466–476.

Josenhans, C. and S. Suerbaum (2002). "The role of motility as a virulence factor in bacteria". In: *International Journal of Medical Microbiology* 291.8, pp. 605–614.

Kamiya, R. and S. Asakura (1976). "Flagellar transformations at alkaline pH". In: *Journal of Molecular Biology* 108.2, pp. 513–518.

Kapur, J. et al. (1985). "A new method for gray-level picture thresholding using the entropy of the histogram". In: *Computer Vision, Graphics, and Image Processing* 29.3, pp. 273–285.

Kim, M. et al. (2003). "A macroscopic scale model of bacterial flagellar bundling". In: *Proceedings of the National Academy of Sciences* 100.26, pp. 15481–15485.

Kinosita, Y. et al. (2017). "Unforeseen swimming and gliding mode of an insect gut symbiont, *Burkholderia sp.* RPE64, with wrapping of the flagella around its cell body". In: *The ISME Journal.*

Krell, T. et al. (2010). "Diversity at its best: bacterial taxis". In: *Environmental Microbiology* 13.5, pp. 1115–1124.

Kühn, M. J. et al. (2017). "Bacteria exploit a polymorphic instability of the flagellar filament to escape from traps". In: *Proceedings of the National Academy of Sciences of the USA* 114.24, pp. 6340–6345.

Lacal, J. et al. (2010). "Sensing of environmental signals: classification of chemoreceptors according to the size of their ligand binding regions". In: *Environmental Microbiology* 12.11, pp. 2873–2884.

Lassak, J. et al. (2010). "ArcS, the Cognate Sensor Kinase in an Atypical Arc System of *Shewanella oneidensis* MR-1". In: *Appl. Environ. Microbiol.* 76.10, pp. 3263–3274.

Lauga, E., W. R. DiLuzio, et al. (2006). "Swimming in Circles: Motion of Bacteria near Solid Boundaries". In: *Biophysical Journal* 90.2, pp. 400–412.

Lauga, E. and T. R. Powers (2009). "The hydrodynamics of swimming microorganisms". In: *Reports on Progress in Physics* 72.9, p. 096601.

Leifson, E. (1960). *Atlas of bacterial flagellation.* New York & London, Academic Press.

Leis, A. P. et al. (2005). "Optically Transparent Porous Medium for Nondestructive Studies of Microbial Biofilm Architecture and Transport Dynamics". In: *Appl. Environ. Microbiol.* 71.8, pp. 4801–4808.

Lighthill, J. (1975). "Flagellar Hydrodynamics". In: *SIAM Rev.* 18.2, pp. 161–230.

Macnab, R. M. (1976). "Examination of bacterial flagellation by dark-field microscopy." In: *Journal of Clinical Microbiology* 4.3, pp. 258–265.

– (1977). "Bacterial flagella rotating in bundles: a study in helical geometry". In: *Proceedings of the National Academy of Sciences* 74.1, pp. 221–225.

Macnab, R. M. and M. K. Ornston (1977). "Normal-to-curly flagellar transitions and their role in bacterial tumbling. Stabilization of an alternative quaternary structure by mechanical force". In: *Journal of Molecular Biology* 112.1, pp. 1–30.

Magariyama, Y. et al. (1995). "Simultaneous measurement of bacterial flagellar rotation rate and swimming speed". In: *Biophysical Journal* 69.5, pp. 2154–2162.

Masson, J.-B. et al. (2012). "Noninvasive inference of the molecular chemotactic response using bacterial trajectories". In: *Proceedings of the National Academy of Sciences.*

McFall-Ngai, M. et al. (2013). "Animals in a bacterial world, a new imperative for the life sciences". In: *Proceedings of the National Academy of Sciences* 110.9, pp. 3229–3236.

Mears, P. J. et al. (2014). "*Escherichia coli* swimming is robust against variations in flagellar number". In: *eLife* 3.e01916, e01916.

Meister, M. et al. (1987). "The proton flux through the bacterial flagellar motor". In: *Cell* 49.5, pp. 643–650.

Miller, V. and J. Mekalanos (1988). "A novel suicide vector and its use in construction of insertion mutations: osmoregulation of outer membrane proteins and virulence determinants in *Vibrio cholerae* requires toxR". In: *J. Bacteriol.* 170.6, pp. 2575–2583.

Min, T. L. et al. (2009). "High-resolution, long-term characterization of bacterial motility using optical tweezers". In: *Nat Meth* 6.11, pp. 831–835.

Minamino, T. et al. (2003). "Effect of Intracellular pH on Rotational Speed of Bacterial Flagellar Motors". In: *Journal of Bacteriology* 185.4, pp. 1190–1194.

Murat, D. et al. (2015). "Opposite and Coordinated Rotation of Amphitrichous Flagella Governs Oriented Swimming and Reversals in a Magnetotactic Spirillum". In: *Journal of Bacteriology* 197.20. Ed. by J. S. Parkinson, pp. 3275–3282.

Murphy, D. B. (2002). *Fundamentals of Light Microscopy and Electronic Imaging.* John Wiley & Sons.

Neidhardt, F. C. and R. Curtiss, eds. (1996). *Escherichia coli and Salmonella: Cellular and Molecular Biology.* second. Washington: ASM Press.

Nelson, K. E. et al. (2002). "Complete genome sequence and comparative analysis of the metabolically versatile *Pseudomonas putida* KT2440". In: *Environmental Microbiology* 4.12, pp. 799–808.

Parkinson, J. S. (2003). "Bacterial Chemotaxis: a New Player in Response Regulator Dephosphorylation". In: *Journal of Bacteriology* 185.5, pp. 1492–1494.

Pilizota, T. et al. (2009). "A molecular brake, not a clutch, stops the *Rhodobacter sphaeroides* flagellar motor". In: *Proceedings of the National Academy of Sciences* 106.28, pp. 11582–11587.

Ping, L. et al. (2013). "Swimming behavior of the monotrichous bacterium *Pseudomonas fluorescens* SBW25". In: *FEMS Microbiology Ecology* 86.1, pp. 36–44.

Pohl, O. (2016). "Chemotaxis of self-phoretic active particles and bacteria". PhD thesis. Technische Universität Berlin.

Pohl, O. et al. (2017). "Inferring the Chemotactic Strategy of *P. putida* and *E. coli* Using Modified Kramers-Moyal Coefficients". In: *PLOS Computational Biology* 13.1, e1005329.

Purcell, E. M. (1977). "Life at low Reynolds number". In: *American Journal of Physics* 45.1, pp. 3–11.

Qian, C. et al. (2013). "Bacterial Tethering Analysis Reveals a "Run-Reverse-Turn" Mechanism for *Pseudomonas* Species Motility". In: *Applied and Environmental Microbiology* 79.15, pp. 4734–4743.

Raatz, M. et al. (2015). "Swimming patterns of a polarly flagellated bacterium in environments of increasing complexity". In: *The European Physical Journal Special Topics* 224.7, pp. 1185–1198.

Ranjard, L. and A. Richaume (2001). "Quantitative and qualitative microscale distribution of bacteria in soil". In: *Research in Microbiology* 152.8, pp. 707–716.

Ribeiro, A. C. F. et al. (2014). "Binary Diffusion Coefficients for Aqueous Solutions of l-Aspartic Acid and Its Respective Monosodium Salt". In: *Journal of Solution Chemistry* 43.1, pp. 83–92.

Rosser, G., R. E. Baker, et al. (2014). "Modelling and analysis of bacterial tracks suggest an active reorientation mechanism in *Rhodobacter sphaeroides*". In: *Journal of The Royal Society Interface* 11.97, pp. 20140320–20140320.

Rosser, G., A. G. Fletcher, et al. (2013). "Novel Methods for Analysing Bacterial Tracks Reveal Persistence in *Rhodobacter sphaeroides*". In: *PLoS Comput Biol* 9.10, e1003276.

Ryu, E. (1937). "A Simple Method of Staining Bacterial Flagella". In: *Kitasato Archives of Experimental Medicine* 14, pp. 218–19.

Samatey, F. A. et al. (2001). "Structure of the bacterial flagellar protofilament and implications for a switch for supercoiling". In: *Nature* 410.6826, pp. 331–337.

Santaló, L. A. (1976). *Integral Geometry and Geometric Probability*. Ed. by G.-C. Rota. Encyclopedia of Mathematics and Its Applications. Addison-Wesley Publishing Company.

Saragosti, J. et al. (2011). "Directional persistence of chemotactic bacteria in a traveling concentration wave". In: *Proceedings of the National Academy of Sciences* 108.39, pp. 16235–16240.

Sato, K. and M. Homma (2000). "Functional Reconstitution of the Na$^+$-driven Polar Flagellar Motor Component of *Vibrio alginolyticus*". In: *Journal of Biological Chemistry* 275.8, pp. 5718–5722.

Savitzky, A. and M. J. E. Golay (1964). "Smoothing and Differentiation of Data by Simplified Least Squares Procedures". In: *Analytical Chemistry* 36.8, pp. 1627–1639.

Schaechter, M., ed. (2009). *Encyclopedia of Microbiology.* 3d. Elsevier Science.

Scharf, B. (2002). "Real-Time Imaging of Fluorescent Flagellar Filaments of *Rhizobium lupini* H13-3: Flagellar Rotation and pH-Induced Polymorphic Transitions". In: *Journal of Bacteriology* 184.21, pp. 5979–5986.

Schindelin, J. et al. (2015). "The ImageJ ecosystem: An open platform for biomedical image analysis". In: *Molecular Reproduction and Development* 82.7-8, pp. 518–529.

Schneider, C. A. et al. (2012). "NIH Image to ImageJ: 25 years of image analysis". In: *Nature Methods* 9.7, pp. 671–675.

Segall, J. E. et al. (1986). "Temporal comparisons in bacterial chemotaxis". In: *Proceedings of the National Academy of Sciences* 83.23, pp. 8987–8991.

Shaevitz, J. W. et al. (2005). "*Spiroplasma* Swim by a Processive Change in Body Helicity". In: *Cell* 122.6, pp. 941–945.

Shah, D. S. H. et al. (2000). "The Flagellar Filament of *Rhodobacter sphaeroides*: pH-Induced Polymorphic Transitions and Analysis of the fliC Gene". In: *Journal of Bacteriology* 182.18, pp. 5218–5224.

Sourjik, V. and R. Schmitt (1996). "Different roles of CheY1 and CheY2 in the chemotaxis of *Rhizobium meliloti*". In: *Molecular microbiology* 22.3, pp. 427–436.

Sourjik, V. and N. S. Wingreen (2012). "Responding to chemical gradients: bacterial chemotaxis". In: *Current Opinion in Cell Biology* 24.2, pp. 262–268.

Stock, J. B. and M. D. Baker (2009). "Chemotaxis". In: *Encycloedia of Microbiology.* Ed. by M. Schaechter. 3d. Elsevier Science.

Taktikos, J. et al. (2013). "How the Motility Pattern of Bacteria Affects Their Dispersal and Chemotaxis". In: *PLoS ONE* 8.12, e81936.

Taute, K. et al. (2015). "High-throughput 3D tracking of bacteria on a standard phase contrast microscope". In: *Nature Communications* 6, p. 8776.

Taylor, B. L. and D. E. Koshland (1974). "Reversal of flagellar rotation in monotrichous and peritrichous bacteria: generation of changes in direction". In: *Journal of bacteriology* 119.2, pp. 640–642.

Terasawa, S. et al. (2011). "Coordinated Reversal of Flagellar Motors on a Single *Escherichia coli* Cell". In: *Biophysical Journal* 100.9, pp. 2193–2200.

Terashima, H. et al. (2008). "Chapter 2 Flagellar Motility in Bacteria: Structure and Function of Flagellar Motor". In: *International Review of Cell and Molecular Biology.* International Review of Cell and Molecular Biology 270. Ed. by K. W. Jeon, pp. 39–85.

Theves, M., J. Taktikos, et al. (2015). "Random walk patterns of a soil bacterium in open and confined environments". In: *Europhysics Letters* 109.2, p. 28007.

Theves, M. (2013). "Bacterial motility and growth in open and confined environments". PhD thesis. Universität Potsdam.

Theves, M., J. Taktikos, et al. (2013). "A Bacterial Swimmer with Two Alternating Speeds of Propagation". In: *Biophysical journal* 105.8, pp. 1915–1924.

Timmis, K. N. (2002). "*Pseudomonas putida*: a cosmopolitan opportunist par excellence". In: *Environmental Microbiology* 4.12, pp. 779–781.

Tinevez, J.-Y. et al. (2017). "TrackMate: An open and extensible platform for single-particle tracking". In: *Methods* 115, pp. 80–90.

Bibliography

Turner, L., L. Ping, et al. (2016). "Visualizing Flagella while Tracking Bacteria". In: *Biophysical Journal* 111.3, pp. 630–639.

Turner, L., W. S. Ryu, et al. (2000). "Real-Time Imaging of Fluorescent Flagellar Filaments". In: *J. Bacteriol.* 182.10. Ed. by 1. JB.182.10.2793-2801.2000, pp. 2793–2801.

Turner, L., R. Zhang, et al. (2010). "Visualization of Flagella during Bacterial Swarming". In: *Journal of Bacteriology* 192.13, pp. 3259–3267.

Valdés-Parada, F. J. et al. (2009). "Upscaling microbial chemotaxis in porous media". In: *Advances in Water Resources* 32.9, pp. 1413–1428.

Vogel, R. and H. Stark (2012). "Motor-driven bacterial flagella and buckling instabilities". In: *The European Physical Journal E* 35.2, p. 15.

Vogel, R. (2012). "The bacterial flagellum: Modeling the dynamics of the elastic filament and its transition between polymorphic helical forms". PhD thesis. Technische Universität Berlin.

Vogel, R. and H. Stark (2013). "Rotation-induced polymorphic transitions in bacterial flagella". In: *Physical review letters* 110.15, p. 158104.

Vos, M. et al. (2013). "Micro-scale determinants of bacterial diversity in soil". In: *FEMS Microbiology Reviews* 37.6, pp. 936–954.

Wadhams, G. H. and J. P. Armitage (2004). "Making sense of it all: bacterial chemotaxis". In: *Nat Rev Mol Cell Biol* 5.12, pp. 1024–1037.

Waljor, V. (2016). "Adaptation von *Pseudomonas putida* an die Lockstoffe Casaminosäuren und Benzoat". Bachelor's thesis. Universität Potsdam.

Wang, F. et al. (2017). "A structural model of flagellar filament switching across multiple bacterial species". In: *Nature Communications* 8.1.

Wang, M. and R. M. Ford (2009). "Transverse bacterial migration induced by chemotaxis in a packed column with structured physical heterogeneity". In: *Environ Sci Technol* 43.15, pp. 5921–5927.

Wong-Ng, J. et al. (2016). "The Role of Adaptation in Bacterial Speed Races". In: *PLOS Computational Biology* 12.6. Ed. by C. V. Rao, e1004974.

Xia, Y. and G. M. Whitesides (1998). "Soft Lithography". In: *Angewandte Chemie International Edition* 37.5, pp. 550–575.

Xie, L. et al. (2011). "Bacterial flagellum as a propeller and as a rudder for efficient chemotaxis". In: *Proc Natl Acad Sci U S A* 108.6, pp. 2246–2251.

Zeitz, M. et al. (2017). "Active Brownian particles moving in a random Lorentz gas". In: *The European Physical Journal E* 40.2, p. 23.